

## ABSTRACT

Title of Document: DEVELOPMENT AND TEST OF A  
PERMANENT MAGNET HELICON  
THRUSTER

Michael Frank DeMaio, Jr. M.S. 2010

Directed By: Assistant Professor Raymond Sedwick,  
Department of Aerospace Engineering

This thesis describes the development of a test facility equipped with Langmuir probe and Retarding Potential Analyzer diagnostics for helicon thruster research. A helicon thruster using permanent magnets was also designed and tested. The helicon has several advantages, but the main disadvantage is the use of electromagnets to generate the required magnetic field, requiring a high power draw. The choice of using permanent magnets is to reduce the size, cost and power required to generate high specific impulse thrust. A prototype has been designed, analyzed and tested using Argon with demonstrated specific impulse of 1400 seconds. Analysis of the variation of beam power and ion temperature in the exhaust plume with variation of input power and vacuum pressure are presented. Preliminary tests were conducted using water as a propellant. Measurement of the ion energy distribution function shows a number of peaks indicating the presence of dissociation products.

DEVELOPMENT AND TEST OF A PERMANENT MAGNET HELICON  
THRUSTER

By

Michael Frank DeMaio, Jr.

Thesis submitted to the Faculty of the Graduate School of the  
University of Maryland, College Park, in partial fulfillment  
of the requirements for the degree of  
Master of Science  
2010

Advisory Committee:  
Assistant Professor Raymond Sedwick, Chair  
Keystone Associate Professor Chris Cadou  
Associate Professor Kenneth Yu

© Copyright by  
Michael Frank DeMaio, Jr.  
2010

# Preface

After graduating from Manhattan College with a BS in civil engineering I wanted to follow my passion so I applied to the Aerospace Department at the University of Maryland. From an outside perspective that might seem somewhat irrational or extreme, but I always had a sense of fervor for space propulsion. Looking back on the past three years as a research graduate student, I embarked academically and personally on the greatest journey of my lifetime. I never would have guessed that I would be in the position that I am today, graduating with a master's degree in aerospace engineering and contributing to the field of space propulsion. Furthermore, I would like to thank my family, friends, the SPPL gang also known as the 'A-team' and foremost Dr. Ray Sedwick for making my passion a reality.

# Dedication

I would like to thank and honor Dr. Sedwick for giving me the opportunity to work as his research assistant for the past 3 years. He has provided me with the knowledge, the skills and the confidence that I needed in order to become a successful aerospace engineer. I was very blessed to work with such an established and intellectual man who was not only there for me as an advisor but also as a friend in times of hardship. He has challenged me intellectually and mentally which developed my sense of well being and character.

I would also like to thank my wonderful family, my grandfather and my fiancée Stephanie for supporting me over the past few years. I couldn't have done it without them; they were always there when I needed them, in good times and in bad.

I wish to thank Marissa Intelisano, an undergraduate who worked for Dr. Sedwick in assisting me with my research by designing and building the retarding field potential analyzer. I would like to thank Dustin Alinger, a graduate student at the University of Maryland, for assisting me in building and testing the Langmuir probe. I would also like to thank Jack Touart in the Electronic Development Group (EDG) for assisting me in the production of the helicon thruster.

Furthermore, I would like thank everyone in the Space Power and Propulsion group for being supportive and encouraging during my time here at the University of Maryland. God Bless.

# Acknowledgments

This research was funded in part by the UMD, Department of Aerospace Engineering and in part by the National Science Foundation, Award Number #0846320.

**“It builds character.”**

Thanks Ray!

It sure did.



Calvin and Hobbes by Will Watterson

# Table of Contents

Preface.....	ii
Dedication.....	iii
Acknowledgments.....	iv
Table of Contents.....	v
List of Figures.....	vii
List of Tables.....	ix
Chapter 1: Introduction.....	1
1.1 Motivation: Electric Propulsion Systems.....	1
1.2 The Helicon Plasma Source and Thruster.....	3
1.3 Previous Work.....	5
1.3.1 Background.....	5
1.3.2 Laboratory Plasmas.....	6
1.3.3 The Modern Helicon Source.....	7
1.3.4 Helicon Thruster.....	9
1.4 Objectives and Approach.....	10
Chapter 2: Helicon Modeling.....	12
2.1 Plasma Theory.....	12
2.1.1 The Helicon Wave.....	12
2.1.2 Modal Structures.....	14
2.1.3 Antenna Coupling.....	15
2.1.4 Polarization.....	15
2.2 Helicon Waves in Confined Plasmas.....	16
2.2.1 Eigenmodes.....	16
2.2.2 Landau Damping.....	18
2.2.3 Trivelpiece-Gould Modes.....	19
2.3 Current-Free Layers.....	22
2.3.1 Double Layer.....	22
2.3.2 Single Layer (Free-Standing Plasma Sheath).....	23
2.4 Loss Mechanisms and Efficiency.....	25
2.4.1 Bremsstrahlung Radiation.....	26
2.4.2 Ionization.....	27
2.4.3 Excitation.....	29
2.4.4 Ambipolar Diffusion.....	30
2.4.5 Efficiency.....	32
2.5 Summary of Chapter 2: Helicon Theory.....	33
Chapter 3: Design of Experiment.....	34
3.1 Helicon Source Dimensioning.....	34
3.2 Antenna Design.....	36
3.3 Magnet Design.....	38
3.4 Facility Setup.....	42

3.4.1 RF Power Supply and Matching Network .....	43
3.4.2 RF Feedthrough .....	45
3.4.3 Electromagnetic Radiation.....	46
3.5 Retarding Potential Analyzer.....	47
3.5.1 Probe Description.....	47
3.5.2 LabVIEW Interface.....	49
3.6 Langmuir Probe .....	50
3.6.1 Probe Description.....	50
3.6.2 LabVIEW Interface.....	54
3.7 Gas Feed Systems .....	55
Chapter 4: Testing.....	56
4.1 Retarding Potential Analyzer Data .....	56
4.1.1 Sample Measurements .....	56
4.2 Langmuir Probe Data.....	58
4.2.1 Sample Measurements .....	58
4.3 Radiated Power .....	59
4.4 Operation with Water Vapor.....	60
Chapter 5: Analysis of Results.....	62
5.1 Langmuir Probe .....	62
5.1.1 Standard Theory.....	62
5.1.1 Alternate Theory .....	65
5.2 Retarding Potential Analyzer.....	68
5.2.1 Theory .....	68
5.2.1 Results and Discussion .....	70
Chapter 6: Conclusions, Contributions and Future Work.....	75
6.1 Conclusions.....	75
6.1.1 Analytical Modeling .....	75
6.1.2 Facility Development.....	76
6.1.3 Helicon Source Development and Testing .....	76
6.2 Contributions.....	77
6.3 Future Work .....	78
6.3.1 Facility Upgrades .....	78
6.3.2 Thruster Upgrades.....	78
6.3.3 Experimental Procedures .....	79
Appendices.....	80
APPENDIX A: RPA I-V Curves for Argon .....	80
APPENDIX B: RPA Ion Distribution Functions for Argon.....	83
APPENDIX C: Error Analyses .....	91
C.1 Langmuir Probe and RPA Error Analysis: Area under a Shifted Maxwellian .....	91
C.2 RPA Error Analysis for Ion Temperature: Matching FWHM of IEDF curve .....	93
APPENDIX D: MATLAB Code for Retarding Potential Analyzer Analysis .....	94
APPENDIX E: MATLAB Code for Langmuir Probe Analysis .....	99
Bibliography .....	104

# List of Figures

- [1] Figure (2.1): Electric field patterns for the  $m = 0$  mode
- [2] Figure (2.2): Electric field patterns for the  $m = +1$  mode
- [3] Figure (2.3): Landau Damping Phenomenon depicting relative motion of electrons
- [4] Figure (2.4): Plasma Density versus Magnetic Field parameterizing TG and Helicon modes
- [5] Figure (2.5): Plasma Sheath
- [6] Figure (2.6): Ambipolar Diffusion
- [7] Figure (3.1): Single Turn Helix Antenna with bus connectors
- [8] Figure (3.2): Five Neodymium Magnets with Pyrex (outer) and Quartz (inner) tube
- [9] Figure (3.3): Stack of five Neodymium Permanent Magnets separated by G-10 spacers
- [10] Figure (3.4): Quartz Tube [Bottom] and Pyrex Tube with 1 ¼" hole [Top]
- [11] Figure (3.5): Cross sectional line plot of the magnetic flux density along the z-direction
- [12] Figure (3.6): Streamlines in the x-z plane
- [13] Figure (3.7): Schematic of the Helicon Thruster [exit plane at  $z = 0$ inch]
- [14] Figure (3.8): Helicon Thruster inside the SPPL Vacuum Chamber
- [15] Figure (3.9): AG-1213 RF Power Supply
- [16] Figure (3.10): AIM/ATN Matching Network
- [17] Figure (3.11): PT-II-CE Controller
- [18] Figure (3.12): RF feedthrough with a single HN connector
- [19] Figure (3.13): Plasma ignition at 100W using  $H_2O$ ,  $p = 2e-3$ mbar [RPA was positioned 3 inch from the exit plane]
- [20] Figure (3.14): Retarding Potential Analyzer (RPA)
- [21] Figure (3.15): Cross Section of the Retarding Potential Analyzer using COMSOL

- [22] Figure (3.16): Detail Schematic of the Retarding Potential Analyzer and its components
- [23] Figure (3.17): RF Compensated Langmuir Probe [with auxiliary electrode]
- [24] Figure (3.18): Schematic of the RF Compensated Circuit
- [25] Figure (3.19): Impedance vs. Frequency Curve for 100 $\mu$ H RF Conformal Inductor
- [26] Figure (3.20): Schematic of the Langmuir Probe Setup
- [27] Figure (3.21): CONCOA 560 Series 150mm Flow regulator
- [28] Figure (4.1): I-V curve (left) and derivative (right) at 50W and 8.5e-3mbar
- [29] Figure (4.2): I-V curve (left) and derivative (right) at 50W and 4e-3mbar
- [30] Figure (4.3): I-V curve (left) and derivative (right) at 50W and 2e-3mbar
- [31] Figure (4.4): I-V Curve, RF Compensated Case
- [32] Figure (4.5): Electron Energy Distribution Function (EEDF), RF Compensated Case
- [33] Figure (4.6): I-V Curve, Uncompensated Case
- [34] Figure (4.7): Electron Energy Distribution Function (EEDF), Uncompensated Case
- [35] Figure (4.8): Helicon Operation with Argon at 100W (upper left), 150W (upper right), 200W (lower left) and 250W (lower right)
- [36] Figure (4.9): Plasma ignition using H<sub>2</sub>O, P =150W, p =2e-3mbar
- [37] Figure (4.10): I-V Curve for H<sub>2</sub>O at P =150W
- [38] Figure (4.11): Ion Distribution Curve for H<sub>2</sub>O
- [39] Figure (5.1): Theoretical Curve for Langmuir Probe
- [40] Figure (5.2): (left) Average I-V curve for Argon, at 100W, (right) Semi-log plot of curve
- [41] Figure (5.3): Derivative of I-V plot at P =100W, p =2e-3mbar
- [42] Figure (5.4): I-V curve (left) and derivative (right) at 50W and 4e-3mbar
- [43] Figure (5.5): Variation of Beam Energy with Input Power at 2e-3, 4e-3 and 8.5e-3mbar
- [44] Figure (5.6): Variation of Ion Temperature with Power at 2e-3, 4e-3 and 8.5e-3mbar
- [45] Figure (5.7): Variation of Beam Energy with Pressure at 50, 100 and 150 Watts Power

# List of Tables

**Table 2.1:** Parameters for ionization cross section in Argon

**Table 2.2:** Parameters for excitation cross section in Argon

**Table 3.1:** Approximate tube diameters as a function of frequency

**Table 5.1:** Ion temperature and ion beam energy at 50, 100, 150W and pressures at  $8.5 \times 10^{-3}$ ,  $4 \times 10^{-3}$ , and  $2 \times 10^{-3}$  mbar using the Full Width Half Maximum Method

**Table 5.2:** Ion temperature and ion beam energy at 50, 100, 150W and pressures at  $8.5 \times 10^{-3}$ ,  $4 \times 10^{-3}$ , and  $2 \times 10^{-3}$  mbar using the Area Method

# Chapter 1: Introduction

## *1.1 Motivation: Electric Propulsion Systems*

The performance metrics for propulsion systems typically include thrust, power, mass, specific impulse and efficiency in some combination of relevant importance. For some systems, such as launch vehicles, thrust becomes a driving requirement since the system has to be able to accelerate at more than 1-g. When thrust is not the driver, such as for in-space propulsion systems, specific impulse will often take precedence since it has an exponential effect on propellant mass. To achieve ever-higher specific impulses, it is necessary to energize and accelerate the propellant to higher velocities, and the class of technologies that provide this energy through some electrical means are known as electric propulsion (EP) systems.

A variety of acceleration techniques have been employed in the development of EP systems, including electrothermal, electrostatic and electromagnetic mechanisms. The most basic approach, electrothermal, directly heats the propellant by some means and then allows the propellant to undergo a thermodynamic expansion through a nozzle. Methods of heating include resistive (resistojet), conductive (arcjet), inductive (radio frequency) and radiative (microwave) energy transfer. The limitation of these systems (apart from available power) is actually in the materials that comprise them, since they are in direct contact with a hot, dense propellant. This ultimately limits the operating temperatures and consequently the specific impulse. Maximum values in the 800-900 second range are theoretically possible; however values between 100-500 seconds are typical<sup>1</sup>.

To overcome the thermal limitations, it was conceived that a direct acceleration of ions by an electrostatic field could be implemented. This is the principal behind the ion thruster. A relatively low energy, non-thermal plasma is formed and from it ions are extracted and accelerated through high potentials to produce thrust. The excess electrons from the plasma are pumped out of the system and released thermionically where they can return to the ion beam to provide net-neutrality. The limitation to this system is certainly not specific impulse, since values as high as 5000 seconds are easily attainable<sup>2</sup>. Instead, this system is limited by thrust

density, with typical values on the order of one  $\text{N/m}^2$ . To achieve even this small value, it is necessary to use heavy noble gases such as Xenon, which is in limited supply and very expensive. The source of the low thrust density is the build-up of space charge between the accelerating plates, limiting the amount of current that can be extracted.

To address the problem of thrust density, classes of electromagnetic propulsion systems are under ongoing development. A notable technology in this category is the Hall Thruster, or Stationary Plasma Thruster. In this system, electrons in the ionization region are trapped by radial magnetic field lines, thus avoiding the build-up of space-charge. Hall thrusters are easily capable of specific impulses in the 1000-3000 second range, with thrust densities on the order of  $40 \text{ N/m}^2$ , and efficiencies on the order of 60%<sup>3</sup>. The main drawback of the Hall thruster is in fact not related to its performance characteristics, but rather its operational lifetime. The Hall thruster, like the ion engine, suffers from a problem of grid erosion, so it is not yet a feasible technology for missions with high  $\Delta V$  requirements over a long duration.

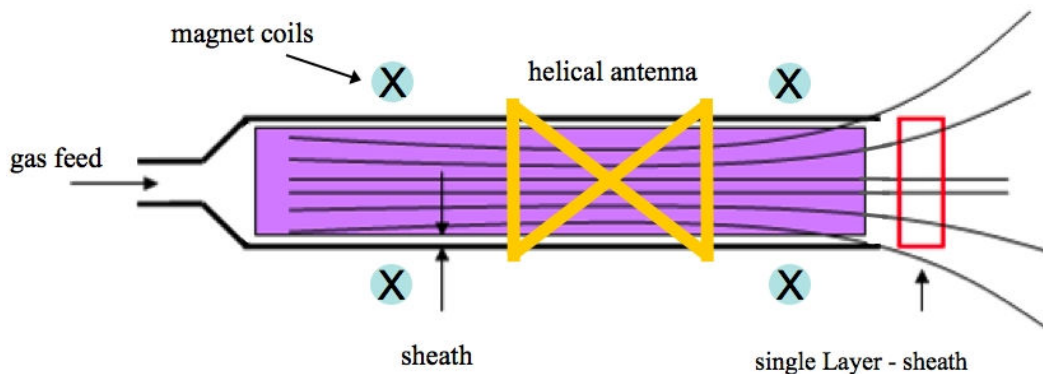
The big brother of the Hall Thruster, and in fact a close cousin of the arcjet is the Magnetoplasmadynamic (MPD) thruster. This system is capable of 6000 seconds of specific impulse and thrust densities of  $400 \text{ N/m}^2$ , although the theoretical limit is much higher<sup>4</sup>. The main drawback of this technology is that while it works very well at very high power levels (100 kW is a typically quoted value) its capabilities fall substantially as more reasonably attainable power levels are considered. Another drawback of this system, like its close relatives, is the problem of erosion. Long duration missions will require that the system can remain fully operational over tens of thousands of hours of continuous operation, and as of now this is a target that is still difficult to realize.

While many other technologies have been conceived and developed, one last system that will be mentioned is the Variable Specific Impulse Magnetoplasma Rocket (VASIMR)<sup>5</sup>. This system uses a magnetized plasma source to produce ions that are then heated directly to high energies through the process of ion cyclotron heating. The ions remain attached to magnetic field lines, protecting structural elements from potentially high heat loads. The magnetic field lines then diverge to convert the gyrational motion of the ions into directed thrust. The specific impulse of the system is variable as a result of being able to choose the amount of energy that is deposited

into the ions before they are expelled, which allows for high thrust to be achieved at the expense of specific impulse, or vice versa, as necessary under a fixed power availability. The VASIMR, like the MPD Thruster, is a system that is more appropriate to larger power systems, such as those that would drive interplanetary travel. It is of particular note because at its heart is the helicon plasma source, chosen because of its high ionization efficiency and its magnetization. Within the last decade it has been realized that this plasma source will exhibit the properties of a thruster all by itself, and its interesting properties make it the subject of the current research effort.

### ***1.2 The Helicon Plasma Source and Thruster***

The helicon plasma source in its thruster configuration is shown in the figure below. It consists of a tube of quartz or Pyrex into which gas is fed. Around the tube are typically placed a pair of Helmholtz coils to provide a uniform axial magnetic field that diverges at the end of the tube. Also around the outside of the tube is an antenna that can take many different forms. Some of these are discussed shortly. This antenna is connected to a radio frequency (RF) power supply that is typically producing power at the industrial usage 13.56 MHz frequency. The current flowing through the antenna induces a time varying magnetic field within the gas, which in turn results in a curling electric field. The electric field accelerates the free electrons in the gas until they reach a sufficiently high energy to cause ionization, and once a critical density of electrons are present an avalanche occurs and the plasma ignites.



At any surface contacted by the plasma a sheath forms as a result of the difference in mobility of the ions and electrons, and the wall becomes negatively charged relative to the plasma. This

drop in potential is gas dependent, and for Argon it is about 5 times the electron temperature when expressed in electron volts. Typically in plasmas the sheath is a primary source of energy loss, since ions are accelerated through this potential, only to hit the wall deposit this energy as heat. In addition, the energy that went into their ionization is also lost as they neutralize. The plasma is, however, very effective at confining most of the electron population in the plasma.

In the helicon, for a sufficiently high magnetic field, even the high energy electrons are confined, since their gyroradii around the magnetic field lines are typically very small in comparison to the scale of the device. While this is not true for the ions, their ability to reach the wall is still limited, since a rapid drain of ions would result in a large electric field build-up that would tend to hold them back. The ions and electrons are then forced to diffuse together across the magnetic field lines through the process of ambipolar diffusion. This substantially reduces the power lost to the walls and contributes to the efficiency of the plasma source. Pinching the field lines upstream (not shown) can provide similar confinement at the end with the gas feed.

At the exit of the thruster is a different story. Here, provided the pressure outside the thruster is low enough, the diverging magnetic fields will cause a free-standing sheath to form, referred to as a single layer. The details of this formation will be discussed later in this thesis. The presence of this sheath again causes ions to accelerate, reaching speeds typically in excess of 12,000 m/s. In addition, at steady-state, electrons leave the exit at the same rate (although not the same velocity) as the ions, resulting in a quasi-neutral thrust generating beam. This is an advantage of the helicon over other ionizing EP systems, which have to provide a completely separate power supply to maintain the neutrality of the beam.

The inductive coupling of the helicon source brings with it two other advantages. The first is that the propellant is not in direct contact with the antenna, so that it will not suffer from erosion. The use of a glass or quartz tube to contain the plasma makes it very robust against potentially reactive ions, allowing arbitrary gases to be used as propellants. One propellant that is of interest is simply to use water vapor because of its storability, abundance (both on Earth and elsewhere in the solar system), low cost and safe handling.

The other advantage of the coupling is its unique nature in the helicon. The simplified ionization mechanism discussed above is true for any inductively coupled plasma; however for a helicon, the interaction of the induced field with the static axial magnetic field causes the launch of helicon waves, as discussed shortly. Either through direct wave-electron acceleration, or through mode conversion to Trivelpiece-Gould waves, the efficiency with which energy is transferred into ionization is much larger for the helicon than for other RF plasmas. This results in roughly an order of magnitude decrease in the ionization energy cost, or an associated increase in density for the same power input.

The final point to be made about the helicon is that its main disadvantage is the need for a static axial magnetic field. It will be seen that higher fields promote larger plasma densities (i.e. more thrust), however the power required to generate these fields using electromagnets can more than offset the potential benefits of the helicon. A natural thought is to instead use permanent magnets; however the field structure of these magnets is not ideal. Research is being conducted at the University of Maryland Space Power and Propulsion Lab that may lead to a way of shaping these fields using the Meissner effect of superconductors to improve performance. The first step, however, is to develop a facility that will allow for a baseline permanent magnet helicon to be built and tested, paving the way for this follow-on research. This thesis describes the design and development of the facility, diagnostics and prototype thruster used in this initial effort.

## ***1.3 Previous Work***

### **1.3.1 Background**

Boswell and Chen<sup>6</sup> provide a historical perspective on helicon sources from the early 20<sup>th</sup> century to the mid-1980s. They mention that during the First World War, the first measurements were made of reflecting right-hand polarized waves. It was reported that long cables were stretched for kilometers away from enemy lines, in order to pick up weak currents produced by telephones. This spy communication tactic led to the discovery of audio frequency whistling tones later known as “whistler waves” that were heard over short durations. At the war front, this phenomenon was christened “the grenades fly” which Barkhausen<sup>7</sup> first mentioned in his scientific journal in 1919. Later he revisited this phenomenon, but was unable to fully

understand the whistling behavior; nevertheless, he speculated it was due to multiple reflections in the Heaviside layer that reflects propagating RF waves.

This unexplained phenomenon sparked the interest of Appleton<sup>8</sup> and Hartree<sup>9</sup>, who developed the first theory on the propagation of electromagnetic waves in magnetized plasma. They formulated a simple dispersion relation, which incorporated electron plasma frequency, electron cyclotron frequency and an angle referencing the respective wave to the magnetic field. This simple dispersion relation provided a first fundamental understanding of the behavior of whistler waves that occurred through the Earth's ionosphere.

In the mid 20<sup>th</sup> century, Storey<sup>10</sup> modified the Appleton-Hartree dispersion relation, providing a more detailed explanation of the whistling atmospheric effect. Storey's suggestive theory for the atmospheric whistling effect was caused by two phenomena: 1) The lightning that provides a point source for the wave and 2) an anisotropic dispersive plasma which supplies the harmonics of the wave as it propagates along the Earth's magnetic field lines. Boswell and Chen<sup>6</sup> provide an example of a whistler wave where the rising and falling of tones are directly frequency dependent on the group velocity. These noise frequency waves are oriented at a particular altitude within the ionosphere, and are guided and weakly propagated along the Earth's magnetic field.

The mid 20<sup>th</sup> century marked the beginning of contemporary helicon sources. The name "helicon" was suggested by Aigrain in 1960<sup>11</sup> to describe an electromagnetic wave that propagated between the electron and ion cyclotron frequency. It was called a helicon wave solely due to the helical rotation as it propagated through a medium. At this point, interests in plasmas had become more abundant due to the possibilities of using diagnostics to measure the behavior of these electromagnetic waves. It was not until the mid 1960's when Klosenberg, McNamara, and Thonemann (KMT) independently presented theories on helicons in cylindrical media.

### **1.3.2 Laboratory Plasmas**

The first observation of helicon modes in laboratory plasma<sup>12</sup> was in 1960 carried out by the Zero Energy Toroidal Assembly (ZETA), where the guided waves propagated along the magnetic field lines. A few years later, Thonemann and Blevin<sup>13</sup> decided to excite electrons

through an azimuthal magnetic field. The current produced by the static magnetic and induced magnetic fields (due to Lenz's law) acted as a plasma confining mechanism. However, it was Lehane and Thonemann<sup>14</sup> who conducted the first helicon-wave experiment in a radio frequency (RF) maintained plasma. It consisted of 10-cm diameter, 100-cm long glass tube. The static magnetic field was less than 500 Gauss, with a pressure that ranged from 10-70 mTorr using Xenon gas. A 3kW RF generator operating at 15 MHz was used to generate plasma. The range in pressure allowed for the propagation of the  $m = 0$  and  $m = 1$  helicon modes. Furthermore, the electron density and temperature were measured. The experimental results were matched successfully with the theory that was devised by KMT a few years earlier.

Throughout the 1960's further experiments were carried out by Blevin and Thonemann<sup>13</sup> to determine whether using high frequencies could excite a helical wave. The experimental apparatus consisted of a 5-cm diameter, 55-cm long glass tube with two magnetic fields coils capable of producing a 2kG field. The frequency ranged from 6-28MHz. The antenna that coupled with the plasma fields was 16-cm long on either side of the glass tube and launched an  $m = +1$  mode helicon wave. Boswell and Chen<sup>6</sup> explain that there was strong evidence to suggest that the choice of static magnetic field governs the highest plasma density that can be achieved and that this maximum density occurs at a particular pressure that was also magnetic field dependent. These maxima were thought to have been forms of resonant behavior that occurred within the system. The dispersion relation was used to calculate the maxima and it provided strong evidence that a helicon wave existed in the system.

In the 1970's many experiments were carried out focusing on lower hybrid heating, fast wave heating, current generation and a variety of low frequency Alfvén wave schemes in helicon plasmas<sup>6</sup>.

### **1.3.3 The Modern Helicon Source**

By the 1980's, a basic design for a helicon source had been developed and was called Waves on Magnetized Beams and Turbulence (WOMBAT). It consisted of a 20-cm diameter helicon source attached to a 100-cm diffusion chamber. The research was done at the Australian National University (ANU) and its purpose was to simulate wave and electron beam interactions within the auroral plasma<sup>6</sup>. Using mainly spectroscopy and ultra high frequency (UHF)

interferometry diagnostics, the differential radial intensity profiles of Argon were measured. It was found that increasing the intensity of the magnetic field showed a variation in the ionization rate across the plasma.

By the mid 1980's a researcher, Daniel Henry, brought with him to ANU a set of 4-inch complimentary metal-oxide semiconductor (CMOS) test wafers (silicon based) to test etching characteristics in the small-density machine (BASIL) and in WOMBAT<sup>6</sup>. After much testing particularly in BASIL, Henry and Boswell observed that rapid etching exists for short durations (order of milliseconds) after the RF plasma pulsed when the plasma density had decayed by a few orders of magnitude. Boswell and Chen<sup>6</sup> concluded that recombination played a role in the etching of the Si ions. The experiment demonstrated that increasing the pulsing frequency and decreasing the pressure can improve etching rates. The results of these experiments motivated present day helicon source experiments.

One particular experiment that was performed by Sato et al<sup>15</sup> investigated right-hand polarized waves using three different types of helicon antennas to relate the magnetic field to the density variation in the plasma. The experimental setup consisted of a 40-cm long glass tube with an inner radius of 9.3-cm. The applied magnetic field and pressure was 110 Gauss and  $5 \times 10^{-2}$  Pa respectively. The radio frequency was fixed at 13.56 MHz. The power ranged between 100W and 2kW. Three helicon antennas with particular wavelengths were used to investigate wave propagation and efficiency. These antennas consisted of a phased helical, a half turn helical and a double half-turn antenna. Sato et al<sup>15</sup> observed a peak in the plasma density that increased with increasing pressure and magnetic field; however, the electron temperature had an opposite relationship. Sato explained the density peak phenomenon by locally matching the antenna's wavelength to the dispersion relation, which is a function of magnetic field strength and density. On the contrary, Degeling<sup>16</sup> suggested that a peak in density arises due to electron trapping, which might occur if the phase velocity of the wave is close to the thermal velocity of the electrons. Overall, the trends for the half turn and phased helical antennas were similar. The density increased as the magnitude of the magnetic field and RF power increased. The double half turn antenna did not observe this trend, which might be attributed to symmetry.

### 1.3.4 Helicon Thruster

Many helicon experiments have been conducted that have observed expanding plasmas in the exit plume. Recent work was performed using a wide variety of noble gases, geometries, pressures, powers, and magnetic fields. The Chi-Kung experiment<sup>17</sup> was the first to observe what is referred to as a current free double layer in the late 20<sup>th</sup> century. The experiment consisted of a 15-cm diameter, 32-cm long cylindrical glass tube with a conventional double saddle antenna. The conventional gas that was used in the ionization process was Argon. Operating at 13.56MHz, a few hundred watts, and low pressure, a current free double layer was formed downstream, which was identified through measurements of the ion energy distribution function. These measurements were taken with a retarding field potential analyzer (RPA), a device to measure ion energy at various axial and radial points downstream of the source.

The current-free double layer is a structure that forms between two plasmas that differ in their density and temperature, and as a result a potential gradient is established between them in steady state. It was observed that a double peak in the energy spectrum of the ions existed, suggesting that two plasmas were formed: 1) a stationary plasma and 2) an ion beam. The second peak exhibited a higher energy and the difference between the peaks is a result of the potential drop of the double layer. Charles and Boswell<sup>17</sup> observed that downstream in the diffusion chamber the density decreases. This is due to an increase in ion velocity as they are accelerated across the double layer. The actual ionization mechanism that governs the double layer formation is the subject of much debate, however results<sup>[18,19]</sup> show that the ion beam formed by the double layer will detach from the magnetic field lines and produce thrust. It is typically assumed that a magnetic field needs to exist for a double layer to form, although its formation has been observed in the absence of a magnetic field in electronegative gases<sup>20</sup>.

West<sup>21</sup> also demonstrated for a given physical geometry, pressure and power a double layer potential can be generated, hence provide appreciable thrust. It was tested in a large vacuum chamber to investigate the feasibility of using the helicon thruster in a space application. The setup is similar to what others have done, consisting of a 15-cm diameter; 29-cm long tube. A fixed pressure, flow rate, magnetic field and low power (using the conventional 13.56MHz frequency) generated a current free double layer. He emphasized that the antenna coupling was more efficient for a smaller gap between the antenna and the tube. This would help prevent

capacitive coupling that might arise. A retarding field potential analyzer was used to capture the behavior of the ion distribution as the beam entered the downstream region. He demonstrated that the source can be applicable to a space application since the potential profile did not change when the retarding potential analyzer was moved far downstream from the exit plane. Furthermore, the pressure at which a current free double layer can exist is within a narrow range, typically between 0.1-1mTorr.

Below pressures of about 0.1 mTorr the double layer is not observed<sup>20</sup>. Instead the formation is identified by Chen<sup>39</sup> as a single layer, or essentially a free-stream sheath supported by the divergence of the magnetic field. This mechanism is more appropriate to the operation of a thruster in space, since the pressure of an ambient plasma would be much lower than this for missions of interest (low drag orbits).

Due to the power requirements to form the required static magnetic field, it was investigated by Chen<sup>22</sup> that the use of permanent magnets could offer an advantage in both power and compact size. This sparked the interest of building a compact thruster using permanent magnets. Chen designed two tubes of different diameters, one being 9-cm and the other being 5-cm to determine their behavior using permanent magnets. It was observed that the 9-cm diameter tube demonstrated a larger plasma resistance, indicative of better antenna coupling. It was suggested that this increase in coupling is due to direct volumetric energy transfer by the Trivelpiece-Gould (TG) damping phenomenon. TG waves are the dominant mode to deposit appreciable energy downstream of the antenna and in lower.

## ***1.4 Objectives and Approach***

The main objective of this thesis is to develop a helicon thruster test facility with preliminary diagnostics to provide for the evaluation of advanced thruster design concepts. To support this objective, a baseline thruster concept that uses permanent magnets instead of electromagnets will be designed and implemented, along with two standard diagnostic tools for studying plasmas. The objective will be accomplished through a combination of analytical, computational and experimental techniques.

The approach is outlined below:

- 1) Develop a 0-Dimensional analytical model of helicon thruster performance that can be used to design a small thruster and predict its operational characteristics.
- 2) Use magnetic field modeling software to aid in the design of a permanent ring magnet configuration that can be used in lieu of electromagnets in the helicon source design
- 3) Build a prototype thruster, based on the analytical model that is capable of operating with either an inert gas such as Argon, or a vapor phase liquid such as water.
- 4) Assist in the design and construction of a Retarding Potential Analyzer and a Radio Frequency Compensated Langmuir probe for the purpose of performing diagnostics on the thruster.
- 5) Compare the predicted and measured performance of the thruster to a) evaluate the performance model, b) characterize the diagnostics and c) provide an operational baseline with which to compare future thruster design improvements.

# Chapter 2: Helicon Modeling

## 2.1 Plasma Theory

### 2.1.1 The Helicon Wave

Helicon waves<sup>23</sup> are right-hand circularly polarized electromagnetic waves that propagate in radially confined magnetized plasma. Chen<sup>23</sup> describes that Whistler waves differ from helicons in two forms: 1) They are low frequency electromagnetic waves and 2) governed by system bounded modes.

It is pertinent to have a fundamental understanding of helicon waves and the behavior they exhibit in gaseous media before examining the helicon as a thruster. While typically the plasma is not uniform across the discharge, it is instructive to assume that it is for the sake of developing a set of governing equations. The dispersion relation<sup>23</sup> is derived by starting with the following governing equations (in SI units):

$$\nabla \times \mathbf{E} = -\partial \mathbf{B} / \partial t \quad (2.1)$$

$$\nabla \times \mathbf{B} = \mu_0 \mathbf{j} \quad (2.2)$$

$$\mathbf{E} = \mathbf{j} \times \mathbf{B} / en_0 \quad (2.3)$$

Equations 2.1-2.3 imply that

$$\nabla \cdot \mathbf{B} = 0 \quad (2.4)$$

$$\nabla \cdot \mathbf{j} = 0 \quad (2.5)$$

$$\mathbf{j}_\perp = -en_0 \mathbf{E} \times \mathbf{B}_0 / B_0^2 \quad (2.6)$$

The  $n_0$  and  $\mathbf{B}_0 = B_0 \hat{z}$  variables represent the uniform equilibrium density and magnetic field respectively. The  $n$ ,  $\mathbf{B}$ ,  $\mathbf{E}$  and  $\mathbf{j}$  are the perturbed density, magnetic and electric fields and current respectively. The displacement current has been neglected in equation (2.2) and in equation (2.6) the plasma current is assumed to be carried by  $\mathbf{E} \times \mathbf{B}$  drift motions of the electrons. Perturbations of the form  $\exp i(m\theta + kz - \omega t)$  are assumed, where  $k$  is the axial wave

number. This represents wave patterns that rotate in the clockwise  $m > 0$  or anticlockwise  $m < 0$  direction, however, according to the literature a dominance of right-handed (clockwise) polarization appears to exist. This leads to two important relationships, again assuming uniform plasma<sup>23</sup>

$$\nabla \times \mathbf{B} = \alpha \mathbf{B} \quad (2.7)$$

$$\alpha(\alpha \mathbf{B}) + \nabla^2 \mathbf{B} = 0 \quad (2.8)$$

where  $\alpha$  is the dispersion relation and is given by

$$\alpha \equiv \frac{\omega \mu_o e n_o}{k B_o} = \frac{\omega \omega_p^2}{k \omega_c^2} \quad (2.9)$$

According to Chen and Boswell<sup>6</sup>  $k$  is to be recognized as the wave number for low frequency Whistler waves moving along  $B_o$  in free space. In bounded systems this wave number is not a free quantity since radial modes govern wave propagation through the medium. Solving for equations (2.7) and (2.8) gives<sup>23</sup> the radial, azimuthal and axial magnetic fields respectively, provided that the cylinder is uniform for a given fixed radius.

$$B_r = -\frac{k}{\omega} E_\theta = A[(\alpha + k)J_{m-1}(Tr) + (\alpha - k)J_{m+1}(Tr)]\cos(m\theta + kz - \omega t) \quad (2.10)$$

$$B_\theta = \frac{k}{\omega} E_r = -A[(\alpha + k)J_{m-1}(Tr) + (\alpha - k)J_{m+1}(Tr)]\sin(m\theta + kz - \omega t) \quad (2.11)$$

$$B_z = 2ATJ_m(Tr)\sin(m\theta + kz - \omega t) \quad (2.12)$$

The  $J_m$  terms represent Bessel functions, which are used to find separable solutions to particular equations. The  $T$  is known as the transverse wave number<sup>23</sup>, given by

$$T = \alpha^2 - k^2 \quad (2.13)$$

The alpha term represents the azimuthal and radial modes for a given radius. Establishing the radial, azimuthal, and longitudinal equations for the B field, it is trivial to find the respective electric fields. According to the dispersion relation equation (2.9), it is evident that if the frequency and wave number are fixed, then the magnetic field would scale linearly with the plasma density, provided sufficient RF power is available.

In practice<sup>6</sup> the radial profile is non-uniform and typically assumed to be parabolic. This implies that the density is more concentrated at a central peak. For purposes of this study, the plasma is assumed to be uniform.

### 2.1.2 Modal Structures

Ellingboe and Boswell<sup>24</sup> surveyed the modal structures of Helicon plasmas and discovered three different modes of operation. These are E, H and W modes. The E-mode is usually referred to as the capacitive mode; the H-mode is called the inductive mode; and finally the W-mode is the helicon mode. The E-mode typically exists at low powers when the plasma density is low and the skin depth (related to Debye length in plasma) is the same or larger scale as the confining cylinder. In the E-mode the antenna is capacitively coupled since the applied E-field can penetrate the plasma and the induced E-field is not yet comparable in strength.

An increase in power will decrease the skin depth. As the skin depth decreases the external E-field is blocked, whereas the B-field can still reach into the core of the plasma enabling a higher mode; the H-mode. Kinder et al<sup>31</sup> stated that while the electric field does not penetrate far into the plasma, it does produce resonant heating near the surface. In the presence of the static axial B-field, the wave coupling eventually dominates and a transition to the W mode occurs. The H and W modes are usually the dominant modes since they are associated with the higher density plasma operation.

The transitions between modes are not always obvious due to other subtle factors that are consequential of plasma behavior, for example TG modes. It has been shown that these transitions do exist in uniform magnetically confined plasmas that are right-hand circularly polarized. Furthermore, it is the first order Bessel functions that governs the behavior of azimuthal electric fields. Kinder et al<sup>31</sup> suggested that a reasonable scaling factor that determines whether or not a W-mode would exist is based on the aspect ratio of wavelength to

length of the plasma medium. Furthermore, both modes were found to exist simultaneously; however, the H-mode seemed to dominate in plasma sources. Depending on whether or not electrostatic coupling (TG mode) is induced will still affect the behavior and power deposition of the source.

### **2.1.3 Antenna Coupling**

This leads into a discussion of antenna coupling effects and how they play a role in transition modes of helicon sources. A variety of antennas have been used in helicon sources. Boswell<sup>25</sup> among others, have used double saddle antennas, while others have used helical and Nagoya Type II and III antennas. Other antennas have been designed to induce higher nodal modes and have been tested by Kim et al <sup>[26,27]</sup>. Furthermore, Blackwell and Chen<sup>28</sup> have conducted experiments regarding pure helical and Nagoya Type III antennas to infer their behaviors in a medium. They concluded that the main difference between these two specific antennas (mentioned above) is the orientation of the magnetic field. It was shown by Blackwell and Chen<sup>28</sup> that a helical  $m = +1$  mode antenna produces a higher density of plasma than the Nagoya Type III antenna. The plasma generated is also more concentrated at the center than for the Nagoya Type III antenna. As discussed later, the eigenmodes of the helicon wave match that of the helical antenna geometry. Therefore, the helical antenna is more efficient at coupling to these modes than other geometries. Due to conclusive evidence that helical antennas are more efficient, the antenna that was used in this research resembles that of a helix.

### **2.1.4 Polarization**

Earlier, it was mentioned that helicon waves can either be right-hand or left-hand polarized depending on the sign of the wave number. It has been observed that there is a dominance of right-hand polarized waves, referred to as  $m = +1$  modes, however it is not generally understood why this dominance exists over left-hand polarized waves ( $m = -1$ ).

According to Chen<sup>23</sup>, in an  $m = +1$  configuration the space charge changes sign across the diameter of the antenna and produces an electric field. The transverse electric field couples with the helicon mode. As the electric field is propagating, it will synchronize relative to the antenna's wavelength. Suzuki<sup>29</sup> claimed that promoting a wave with the opposite helicity, for

example an  $m = +1$  mode with  $k < 0$  would not permit wave excitation. This is due to phase cancelations within the propagating electric field.

Liebermann<sup>30</sup> provides the fundamental axial wavelength in a uniform axial magnetic field for a right-handed polarized wave as

$$\lambda_z = \frac{3.83}{R} \frac{B_o}{q\mu_o n_e \nu_{rf}} \quad (2.14)$$

The above variables represent the radius,  $R$  of the plasma volume, the magnetic field along the  $z$ -direction,  $B_o$ , the elementary charge,  $q$ , the electron density,  $n_e$  permeability,  $\mu_o$  and the frequency,  $\nu_{rf}$ . This relation only holds for electron densities that are low, on the order of  $10^{12} \text{ cm}^{-3}$ . Kinder et al<sup>31</sup> note that the rate at which the wavelength increased would scale proportionally to the magnetic field with a decrease in frequency and power. The wavelength relative to the length of the medium will usually dictate the radial and axial order of waves, while the antenna governs the modal shapes of electromagnetic waves in the plasma.

## 2.2 Helicon Waves in Confined Plasmas

### 2.2.1 Eigenmodes

The wave pattern<sup>23</sup> for a helicon mode is given by equations (2.10-2.12), reproduced below

$$B_r = -\frac{k}{\omega} E_\theta = A[(\alpha + k)J_{m-1}(Tr) + (\alpha - k)J_{m+1}(Tr)]\cos(m\theta + kz - \omega t) \quad (2.15)$$

$$B_\theta = \frac{k}{\omega} E_r = -A[(\alpha + k)J_{m-1}(Tr) + (\alpha - k)J_{m+1}(Tr)]\sin(m\theta + kz - \omega t) \quad (2.16)$$

$$B_z = 2ATJ_m(Tr)\sin(m\theta + kz - \omega t) \quad (2.17)$$

Using equations (2.15-2.17) let's examine the  $m=0$  and  $m=\pm 1$  modes respectively. As mentioned in the section on polarization, local fields are either right-hand or left-hand circularly polarized.

By applying the proper boundary conditions, equations (2.15-2.17) can be written

$$\begin{aligned}
 \text{a) } E_r &= A\omega(\alpha/k)J_1(Tr)\sin(\psi) & \text{d) } B_r &= -AkJ_1(Tr)\cos(\psi) & (2.18,\text{a-f}) \\
 \text{b) } E_\theta &= A\omega J_1(Tr)\cos(\psi) & \text{e) } B_\theta &= A\alpha J_1(Tr)\sin(\psi) \\
 \text{c) } E_z &= 0 & \text{f) } B_z &= ATJ_0(Tr)\sin(\psi)
 \end{aligned}$$

In Figure (2.1) the field is purely electromagnetic when  $\psi = 0$  (center), and when  $\psi = \pi/2$  (right) the field is purely radial and electrostatic. The transition is a hybrid of electromagnet and electrostatic waves, which are seen between  $0 < \psi < \pi/2$ . In the  $m = 0$  mode, the electric field typically dominates over the azimuthal electromagnetic component. Since the  $m = 0$  mode is not a dominant mode in helicons it will not be mentioned further.

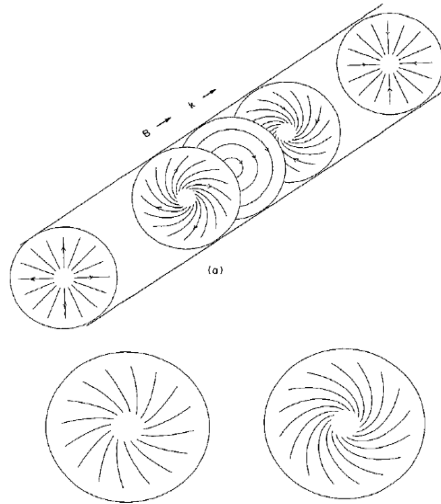


**Figure 2.1** Electric field patterns for the  $m = 0$  mode<sup>23</sup>

The dominant mode is the  $m = +1$  mode. The distinct differences between the two modes are the field patterns. The  $m = +1$  mode field pattern does not change with position, unlike the  $m = 0$  mode. Figure (2.2) depicts the  $m = +1$  mode.

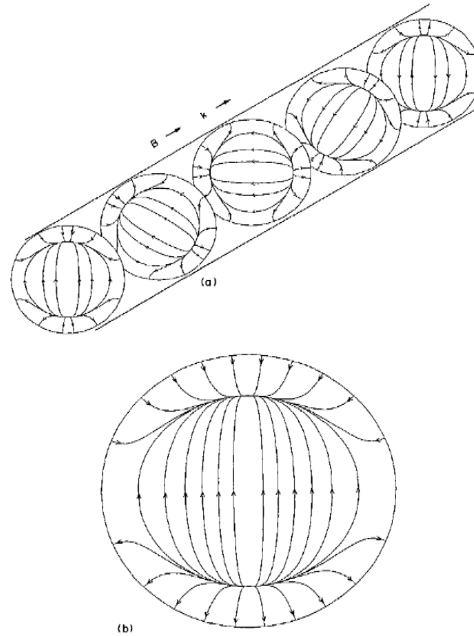


**Figure 2.2** *Electric field patterns for the  $m = +1$  mode*<sup>23</sup>

The electric field pattern is given by equations (2.18,a-c), however it is clear that changing the sign and manipulating the above equations can provide the respective radial and azimuthal components of the magnetic field as well. The electric and magnetic fields are mutually perpendicular to one another as the wave propagates along the  $+z$ -axis. The dampening of helicon waves arises because the magnetic field causes collisions via electron motion. An  $m = +1$  antenna can be designed accordingly to have a strong electric field component near the center. One mechanism thought to cause helicon damping is mentioned in the next section.

### 2.2.2 Landau Damping

Early work<sup>14</sup> showed that the helicon damping length agreed well with theory, however, it was later found<sup>32</sup> that the required collision rates were three orders of magnitude greater than classical theory. In the early 1990's, Chen<sup>34</sup> proposed that if electrons had the proper phase velocity it would promote more efficient ionization by allowing them to match the energy peak of the ionization cross section. This led to the application of a phenomenon known as Landau damping, which explored non-collisional mechanisms based on assumed radial profile densities of the plasma.

To better understand Landau damping, an analogy will be drawn to a surfer on a moving wave such as shown in Figure (2.3). If the surfer were moving more slowly than the wave then the surfer would be gaining energy from the wave, causing it to damp out. On the other hand, if the surfer were moving faster than the wave, then the surfer would be losing energy. This would result in a wave gain.

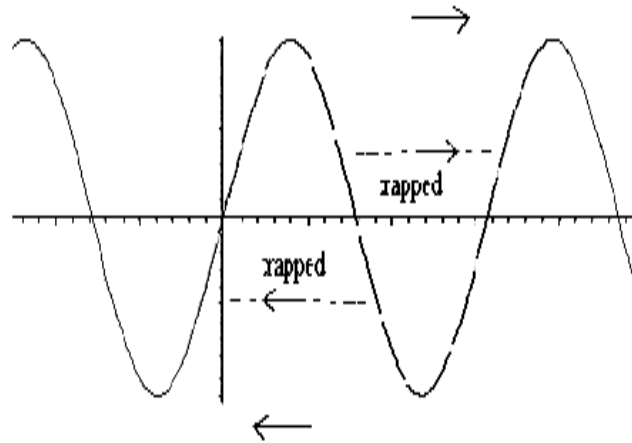


**Figure 2.3** Landau Damping Phenomenon depicting relative motion of electrons<sup>33</sup>

It was conjectured that the ionization in a helicon plasma is a two-step process, the first being the direct acceleration of free electrons by Landau damping, which is a non-collisional process. The second step is collisional, whereby the accelerated free electrons collide with bound electrons and form ions. The reason that the Landau damping hypothesis could potentially lead to more efficient ionization is that it would tend to drive the electron energies towards a shifted Maxwellian that is matched to the ionization energy, thus reducing the number of electrons that are not energetic enough for ionization. These lower energy electrons would tend to excite the bound electrons of the plasma, leading to significant radiation losses and making the effective ionization energy an order of magnitude higher. This is what is typically found in other RF plasmas.

### 2.2.3 Trivelpiece-Gould Modes

It was later suggested by Chen and Blackwell<sup>34</sup> in the early 21<sup>st</sup> century that Landau damping might not be the primary mechanism for ionization in a helicon discharge after all. Their

experiments using an RF compensated energy analyzer demonstrated that electrons that were apparently accelerated by Landau damping were too sparse to account for the high degree of ionization.

There are actually two types of waves of interest in helicon sources: 1) Helicon waves and 2) Trivelpiece-Gould (TG) waves. A helicon wave is an electromagnetic wave that is long and weakly damped across a magnetic field and a TG wave is a quasi electrostatic wave that is strongly damped across a magnetic field. The two waves are actually two modes of the same dispersion relation, appearing once the electron mass is included. Helicon waves are coupled to the TG waves through surface absorption and TG waves are coupled volumetrically to the plasma. TG waves do not naturally arise within a plasma medium. According to Shamrai and Taranov<sup>[35,36]</sup> TG waves deposit their energy inward as they propagate in a plasma. Figure (2.4) depicts the region where helicon and TG modes exist.

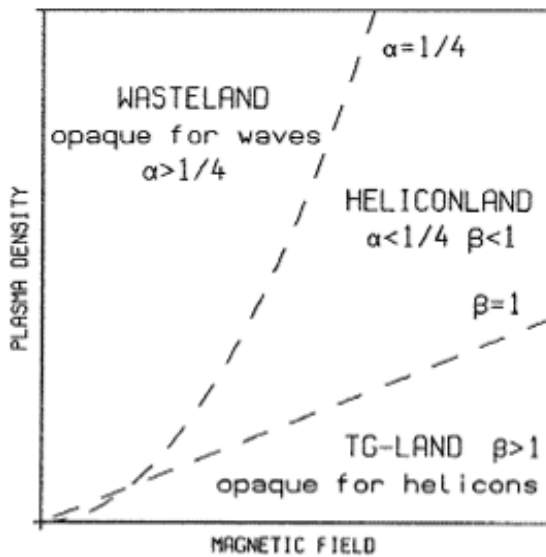


**Figure 2.4** Plasma Density versus Magnetic Field parametrizing TG and Helicon modes<sup>35</sup>

In this figure,  $\beta$  and  $\alpha$  are parameters that are extracted from the dispersion relation given in Shamrai<sup>35</sup>. The amount of power deposited is given by the lowest plasma density which is found by the anti-resonance condition<sup>35</sup>.

$$n = \frac{c}{4\pi e} \frac{B_o k}{\omega r_o} \left( p_{mi} - \frac{kr_o}{m} \right) \quad (2.19)$$

where  $B_o$  is the magnetic field,  $k$  is the parallel wave number,  $e$  is the charge,  $r_o$  is the radius of the antenna,  $c$  is the speed of light,  $\omega$  is the generator frequency, and  $p_{mi}$  is  $i^{th}$  root of the equation  $J_m'(p) + (m/kr_o)J_m(p) = 0$ . The power deposited by TG waves is substantially greater than helicon waves since TG waves are highly damped. The efficiency with which power is absorbed by the plasma is proportional to the effective frequency of the system. The effective frequency is defined by  $\nu_{eff} = \nu / \chi$ , where  $\nu$  is the frequency of electron collisions, and  $\chi$  is a factor that is governed by the geometry of the system.

As mentioned above, an antenna excites two types of waves in a plasma source: 1) Helicon and 2) Trivelpiece-Gould waves (TG). The antenna directly excites the helicon wave, which is strongly coupled azimuthally to the antenna. A TG wave arises when two criteria are met. The first criterion is given by,

$$B_* = \frac{m_e c}{e} \frac{\omega^2}{\nu} \frac{1}{k_{||} r_o} \quad (2.20)$$

where  $B_*$  is the critical magnetic field,  $r_o$  is the radius of the antenna,  $\nu$  is the collisional frequency,  $k_{||}$  is the longitudinal wave number,  $c$  is the speed of light,  $\omega$  is the generator frequency and  $m_e$  is the electron mass. The second criterion is given by

$$d_* = R \frac{\beta}{2|m|} \quad (2.21)$$

where,  $d_*$  is the critical distance between the antenna and the conducting layer,  $R$  is the plasma cavity radius,  $m$  is the mode number, and  $\beta$  is a non-dimensional parameter<sup>35</sup>. The external magnetic field (permanent magnets) and the distance between the antenna and the plasma cavity ( $d$ ) dictate helicon conversion. TG waves are known to be strongly damped and of short

wavelength across magnetic fields, while helicon waves are long and weakly damped. When  $B > B_*$  and  $d > d_*$ , TG waves penetrate into the bulk of the plasma near the plasma edge.

A helicon wave converts to a TG wave when the electron plasma frequency is at its maximum, which is near the surface. At low magnetic fields the power absorption is volumetric and is able to reach the core of the plasma. At high magnetic fields it tends to penetrate the plasma along the surface. Helicon resonances and anti-resonances are destroyed by collisions, which explain the high absorption efficiency in helicon sources.

## 2.3 Current-Free Layers

### 2.3.1 Double Layer

Recent research has shown that a current-free double layer can exist near the downstream of the exit plane where ions are accelerated at supersonic velocities to generate thrust. As mentioned in Chapter 1, the Chi Kung Experiment found the first evidence of the current free double layer. To understand the physical mechanism behind the current free double layer (DL), consider two populations of species that are divided into separate regions where one region is warmer than the other. The electrons in both regions are moving much more quickly than the ions, and those in region one will have a tendency to move more rapidly into region two as a result of their higher energy. In steady-state, the flux of electrons across the interface must be equal, so a potential must be established to equalize the particle flux. This potential then accelerates ions from the higher potential to the lower potential side.

From research by Boswell<sup>37</sup>, the ion distribution function (IDF) was analyzed to determine the ion beam energy and the local plasma potential on each side of the layer which provides a measure of the potential drop across the double layer. The velocity of the beam is given by

$$v_{beam} = \sqrt{\frac{2e(V_{beam} - V_{chamber})}{M}} \quad (2.22)$$

where  $V_{beam}$  is the upstream ion energy,  $V_{chamber}$  is the local plasma potential downstream,  $M$  is the ion mass (depends on the gas), and  $e$  is the electron charge.

Lieberman et al<sup>38</sup> develop a theory for the formation of the double layer. The double layer is described in terms of four species of particles: 1) thermal ions, 2) thermal electrons, 3) mono-energetic ions flowing downstream and 4) mono-energetic electrons flowing upstream. The charge densities are described by Boltzmann relationships. The ratio of ion-to-electron flux is extracted from the charge density relations. It is given by,

$$\frac{\Gamma_e}{\Gamma_i} = \frac{n_{c1}}{n_{b2}} \frac{u_b}{v_i} \frac{e^{-\zeta_1^2}}{\text{erfc}(\zeta_1)} \sqrt{\frac{2M}{\pi m}} \quad (2.23)$$

where,  $n_{c1}$  is the density of mono-energetic electrons downstream,  $n_{b2}$  is the density of mono-energetic ions upstream,  $\zeta_1 = \sqrt{\Phi_e / \tau_e}$ ,  $\tau_e = T_e / V_s$ ,  $\Phi_e = mv_e^2 / 2eV_s$ ,  $T_e$  is the electron temperature,  $V_s$  is the plasma potential,  $v_e$  is the electron velocity,  $M$  is the ion mass, and  $m$  is the electron mass. Furthermore, the double layer strength is governed by pressure, plasma potential and electron temperature. There exists a narrow range of pressures, typically between 0.1-1mTorr<sup>20</sup> for which the double layer exists. Below 0.1mTorr a single layer is instead formed which will be mentioned in the next section.

### 2.3.2 Single Layer (Free-Standing Plasma Sheath)

According to Chen<sup>39</sup> the mechanism for particle acceleration at low external pressure is more consistent with a free-standing sheath, supported by the expanding magnetic field at the exit plane of the helicon source. Through flux conservation, the magnetic field expansion is given by

$$\frac{B}{B_o} = \frac{n}{n_o} = \left( \frac{r}{r_o} \right)^2 \quad (2.24)$$

where,  $B$  is the magnetic field,  $n$  is the density, and  $r$  is the radius of the plasma at each axial location. The reference quantities are defined inside the plasma source. Furthermore, the electrons are assumed Maxwellian, and the electron density is therefore given by the Boltzmann relation as

$$n_e = n_o e^{-\eta} \quad (2.25)$$

where  $\eta = -eV / KT_e$ . Using equation (2.24) it can be determined that the expansion region of the plasma is formed at a position where the flux tube is 28% larger than the discharge radius, at which point the density drops to the value typically seen at the sheath edge ( $n_e = n_0 e^{-1/2}$ ). According to Chen and Arnush<sup>40</sup> the minimum potential that is developed is the floating potential, given by

$$\eta_f = \frac{-eV}{KT_e} = \frac{1}{2} \left[ 1 + \ln \left( \frac{m_i}{2\pi m_e} \right) \right] \quad (2.26)$$

For the case of Argon, this ratio equates to about  $\eta_f = 5.2$ . This factor determines the average energy that will be gained by ions accelerating out of the plasma, and the value is seen to change for different gases. The single layer reaches a steady-state when the flux of ions and electrons is the same. The directed energy of the ion stream is drawn from the electron population and comes from the power to maintain the steady state of the plasma. This phenomenon occurs within the typical sheath thickness, which is about twice the Debye length. The Debye length is typically on the order of micrometers, for plasma sources, and is given by

$$\lambda_d = \left( \frac{\kappa \epsilon_o K_b T}{q^2 N_o} \right)^{1/2} \quad (2.27)$$

Where,  $\kappa$  is the electric permittivity,  $\epsilon_o$  is the electric constant,  $K_b$  is the Boltzmann constant,  $N_o$  is the density in where the potential is equal to zero and  $T$  is the temperature.

Figure (2.5) depicts the sheath. The pre-sheath is the region where ions are accelerated to the Bohm velocity, which is labeled as  $v_b$  in Figure (2.5). At this point the electron density is 40% smaller than the total density within the plasma.

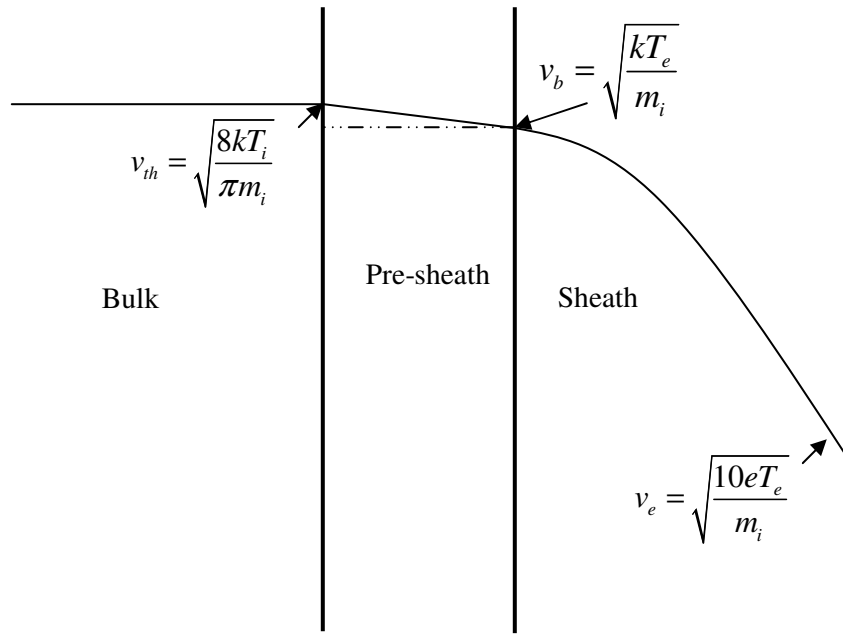


**Figure 2.5** *Plasma Sheath*

The sheath is formed at all solid boundaries of the plasma as well as in the diverging B-field of the exit. The sheath structure at the walls accelerates ions into the walls (ignoring B-field effects for now), which is considered a loss, but confines the majority of the electrons. However, the sheath at the exit plane is responsible for the acceleration of the ions to produce the beam responsible for thrust. The speed of the ions exiting the system is determined by the electron temperature of the plasma, and the higher this value the more efficient the use of the propellant.

## **2.4 Loss Mechanisms and Efficiency**

Loss mechanisms play a vital role in the efficiency and performance of helicon thrusters. The four pertinent losses are Bremsstrahlung radiation, ionization, excitation and ambipolar diffusion. Bremsstrahlung radiation consists of electromagnetic radiation that is generated by the acceleration of free charges when deflected by another charged particle. Ionization, while necessary to produce the plasma, is still a loss mechanism since that energy is not realized in the kinetic energy of the exhaust. Excitation is an unavoidable loss mechanism since collisions that are not energetic enough to ionize an atom will excite bound electrons that radiate as they relax to their ground state. Lastly, ambipolar diffusion directly influences the rate of ion and electron

diffusion across the magnetic field lines to reach the walls. It is evident that these mechanisms are not favorable; however through optimization these losses can be minimized. According to Chen and Arnush<sup>40</sup> the effective ionization energy in a helicon source is 30eV (twice the ionization potential), accounting for these various loss modes. It is worth noting that this is far less than for other RF plasmas, which can have effective ionization energies of 200 eV.

The loss calculations are based on the following set of simplifying assumptions:

- 1) The system is in steady state (good assumption)
- 2) The electrons are monoenergetic (poor assumption)
- 3) The density of the plasma was uniform (poor but mostly harmless assumption)

#### 2.4.1 Bremsstrahlung Radiation

Boyd and Sanderson<sup>14</sup> provide a simple model to determine the total Bremsstrahlung power radiated per unit volume of plasma by assuming an electron moving in the electric field of a stationary ion. The model provides the radiated power by an electron to be

$$P_e = \frac{e^2}{6\pi\epsilon_0 c^3} \left( \frac{Ze^2}{4\pi\epsilon_0 m r^2} \right)^2 \quad (2.28)$$

Assuming a uniform spatial distribution of electrons about the ion then equation (2.28) can be integrated to obtain

$$P = \frac{8\pi Z^2 e^6 n_e}{3(4\pi\epsilon_0)^3 m^2 c^3} \int_{r_{\min}}^{\infty} \frac{dr}{r^2} = \frac{8\pi Z^2 e^6 n_e}{3(4\pi\epsilon_0)^3 m^2 c^3 r_{\min}} \quad (2.29)$$

The minimum radial distance is given by the deBroglie wavelength. This is assumed in order to approximate the distance at which an electron can no longer be considered ‘classical’. The deBroglie wavelength for a thermal electron<sup>14</sup> is given by

$$\lambda_{deB} = \frac{\hbar}{\sqrt{mK_b T_e}} \quad (2.30)$$

where  $\hbar$  is a form of Planck's constant,  $m$  is the electron mass,  $K_b$  is Boltzmann's constant, and  $T_e$  is the electron temperature. Substituting equation (2.30) into equation (2.31) gives

$$P \approx \frac{8\pi Z^2 e^6 n_e}{3(4\pi\epsilon_0)^3 mc^3 \hbar} \sqrt{\frac{K_b T_e}{m}} \quad (2.31)$$

Therefore the total Bremsstrahlung power radiated per unit volume of plasma is found to be

$$P_{ff} = \left( \frac{8\pi Z^2 e^6 n_e}{3(4\pi\epsilon_0)^3 mc^3 \hbar} \sqrt{\frac{K_b T_e}{m}} \right) n_i = 5.34e^{-37} Z^2 n_e n_i \sqrt{T_e} (keV) \quad (2.32)$$

Assuming representative values for the helicon source ( $n_e \approx n_i \approx 10^{12} cm^{-3}$ ,  $T_e = 8eV$ ,  $Z = 1$ ) the effective power radiated was calculated to be on the order of milliWatts and can be ignored.

### 2.4.2 Ionization

Lennon et al<sup>41</sup> and Märk<sup>42</sup> proposed a semi empirical equation for ionization cross-section given by

$$Q_{ionization} = \frac{f(\epsilon)}{\epsilon \epsilon_i} \left( A \ln \frac{\epsilon}{\epsilon_i} + \sum_{j=1}^N B_j \left[ 1 - \frac{\epsilon_j}{\epsilon} \right] \right) \quad (2.33)$$

where  $A$  and  $B$  are coefficients and  $f(\epsilon)$  is a correction function or constant. The constants are given in Table 2.1 for the  $B_j$  terms.

**Table 2.1:** Parameters for ionization cross-section in Argon<sup>41</sup>

Constant	Ar <sup>+</sup>
A	2.532
B <sub>1</sub>	-2.672
B <sub>2</sub>	2.543
B <sub>3</sub>	-0.769
B <sub>4</sub>	0.008
B <sub>5</sub>	0.006
f(ε)	0.4045ε <sup>0.1844</sup>

Using Table 2.1 and assuming  $\varepsilon_i = 15.75eV$  to be the first ionization energy level of Argon, the ionization cross-section is

$$Q_{ionization} = \frac{.707}{20(15.75)} \left( 2.53e^{-17} \ln\left(\frac{20}{15.75}\right) - 2.67e^{-17} \left[ 1 - \frac{15.75}{20} \right] + \dots \right) = 9.90e^{-21} m^2$$

The ionization rate is given by

$$R_{ion} = Q_{ionization} v_e n_{neutral} n_{electrons} V \quad (2.34)$$

where  $v_e$  is the electron velocity,  $n_{neutral}$  is the density of the neutrals in the plasma,  $n_{electrons}$  is the density of the electrons, and  $V$  is the volume of the plasma. The electron velocity, assuming  $T_e = 15.75eV$  is given by

$$v_e = \sqrt{\frac{2(1.609e^{-19})(15.75eV)}{9.1e^{-31}kg}} = 2.36e^6 m/s$$

In steady-state, the total ionization rate is equal to the rate at which ions leave the plasma. This is found by multiplying the flux rate by the bounding area of the plasma and is given by

$$R_{ion} = \Gamma_i A \quad (2.35)$$

where,  $A$  is the total boundary surface of the plasma, and  $\Gamma_i$  is the flux rate. The flux rate is given by equation (2.36)

$$\Gamma_i = n_p e^{-1/2} \sqrt{\frac{K_b T_e}{m_i}} \quad (2.36)$$

where  $n_p$  is the plasma density,  $K_b$  is the Boltzmann constant,  $m_i$  is the ion mass, and  $T_e$  is the electron temperature. The neutral density is determined by manipulating equation (2.37),

$$n_{neutral} = \frac{R_{ion}}{Q_{ionization} v_e n_{electrons} V} \quad (2.37)$$

Lastly the ionization power is given by

$$P_{ion} = R_{ion} E_i \quad (2.38)$$

where  $E_i$  is the ionization energy as defined above. Because the ionization cross-section rapidly increases with electron energy above the ionization potential equation (2.38), the ionization efficiency would potentially increase substantially as the electron energy increases. At some point this cross-section levels out and no further gains in efficiency can be realized.

To estimate how much power goes into ionization, assume representative values for the helicon source [ $n_e \sim 10^{18} \text{ m}^{-3}$ ,  $T_e = 8\text{eV}$ ,  $r = 1 \text{ cm}$ ]. This gives an ionization rate of about  $R_{ion} \sim 10^9 \text{ s}^{-1}$ . The power required for ionization is about 30W assuming an ionization energy of 15.75eV. This is an overestimate of the ionization power because it assumes that the ion flux is driven by the Bohm sheath criterion to all surfaces, however the flux across the field lines will be inhibited by ambipolar diffusion. This will be used to find the power loss to the wall.

### 2.4.3 Excitation

Brusa<sup>43</sup> suggests a semi empirical expression for an excitation cross-section given by

$$Q_{excite} = \frac{1}{F(G + \epsilon)} \ln \left[ \frac{\epsilon}{\epsilon_{exc}} \right] \quad (2.39)$$

where  $F$  and  $G$  are constants,  $\epsilon_{exc}$  is the excitation threshold, and  $\epsilon$  is the incident threshold energy. Table 2.2: Parameters for excitation cross section in Argon provides the  $F$ ,  $G$  and  $\epsilon_{exc}$  parameters which are used in equation (2.39)

**Table 2.2:** Parameters for excitation cross-section in Argon<sup>43</sup>

<b>F</b>	2.52E+21	keV <sup>-1</sup> m <sup>2</sup>
<b>G</b>	2.36E-02	keV
<b><math>\epsilon_{exc}</math></b>	11.5	eV

The excitation power can be found by

$$P_{excite} = E_i Q_{excite} v_e n_e n_{ion} V \quad (2.40)$$

where  $n_{ion}$  is the ion density, and the other variables are defined in the previous section. It is important to note that the ion and electron density were assumed equal due to quasi-neutrality. Furthermore, the neutral density has also been assumed much smaller than the electron density.

The goal is to minimize excitation losses relative to ionization losses. For example, an electron energy of 90eV (largely unachievable) would reduce the excitation loss by almost 50%. This is significant when determining the overall efficiency of the helicon thruster. Again assuming representative values, the excitation power is about 50% of the power due to ionization, or about 15 Watts.

#### **2.4.4 Ambipolar Diffusion**

Ambipolar diffusion occurs when mobile electrons separate from ions and a charge imbalance is generated producing an electric field. This field acts to retard the electrons, which tend to drag the ions along with the electrons to maintain a charge balance. Figure (2.6) depicts this phenomenon. As the electrons and ions move across the density gradient, the electrons will have a more difficult time crossing the static magnetic field than the ions. The ions will continue to diffuse until the ambipolar electric field starts to slow them down and the electrons and ions diffuse together across the field lines. This diffusion mechanism also contributes to the total losses within the plasma volume since it governs the rate at which particles reach the walls.

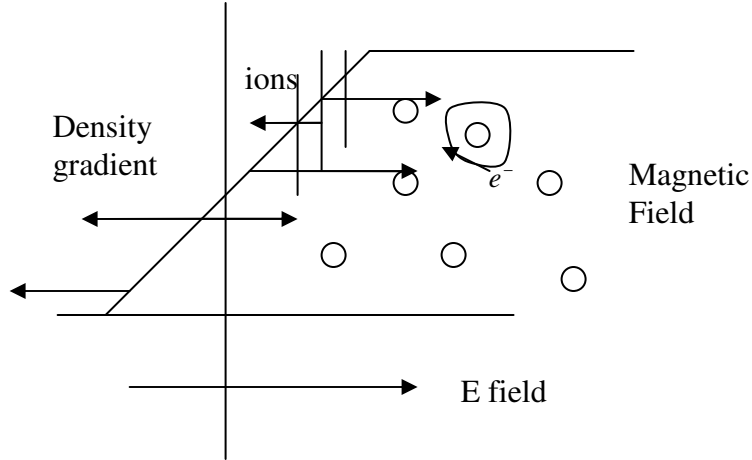


**Figure 2.6** *Ambipolar Diffusion*

According to Schneider<sup>44</sup> the power loss to the walls per electron-ion pair is given by

$$P_{wall} = \frac{neE_iV}{\tau_r} \quad (2.41)$$

where,  $n$  is the plasma density,  $e$  is the charge,  $E_i$  is the ionization energy,  $V$  is the volume ( $V = \pi r^2 L$ ). This form assumes a representative diffusion time constant ( $\tau_r$ )<sup>44</sup>, which is given by equation (2.42). In cylindrical geometry,

$$\tau_r = \frac{R^2}{D_c(5.76)} \quad (2.42)$$

where  $R$  is the tube radius, and  $D_c$  is the diffusion constant, which is given by

$$D_c = \frac{\eta n_o (kT_e + kT_i)}{B^2} \quad (2.43)$$

Using equations (2.41-2.43), the power loss can be written as

$$P_{wall} = C \left( \frac{n_e}{B} \right)^2 \quad (2.44)$$

where  $C = \frac{2e^{-11}E_i m_e V}{T_{ev}^{1/2} R^2}$ ,  $R$  is the tube radius,  $m_e$  is the electron mass,  $V$  is the plasma volume,

$T_{ev}$  is the electron temperature, and  $E_i$  is the threshold energy. It is important to note that the power lost to the wall is proportional to the ratio of plasma density to magnetic field. As will be shown in Chapter 3, for a fixed tube radius and ionization energy, the ratio of  $n/B$  is roughly constant. Therefore even though more power is delivered to the plasma, the power lost to the wall remains approximately constant. Therefore the efficiency of the thruster (at least with regard to wall losses) should increase at higher power levels.

Assuming the nominal values used previously, with the addition of a 200 Gauss magnetic field, will give about 0.3 Watts of power loss to the walls. However, at a more desirable density of  $10^{13} \text{ cm}^{-3}$ , this power would increase to 35 Watts, unless the magnetic field was increased accordingly.

### 2.4.5 Efficiency

The efficiency is given by equation (2.45)

$$\eta = \frac{\text{useful}}{\text{total}} = \frac{\text{useful}}{\text{useful} + \text{lost}} = \frac{1}{1 + \frac{\text{lost}}{\text{useful}}} \quad (2.45)$$

where  $P_{\text{useful}}$  is the useful power, defined here as the beam power. Under this definition

$$P_{\text{useful}} = \left[ \frac{1}{2} m_i v^2 \right] \dot{m} \frac{1}{m_i} = \frac{1}{2} \dot{m} v^2 = \frac{1}{2} (\dot{m} v) v = \frac{1}{2} T v_e \quad (2.46)$$

where  $T$  is the thrust and is given by

$$T = n_o e^{(-1/2)} m_i A \left( \frac{e T_e}{m_i} \right)^{1/2} \left( \frac{10 e T_e}{m_i} \right)^{1/2} \quad (2.47)$$

and  $m_i$  is the ion mass,  $T_e$  is the electron temperature,  $A$  is the cross sectional area of the quartz tube and  $n_o$  is the bulk density. The exit velocity (which appears in the thrust as well) is

$$v_e = \sqrt{\frac{10eT_e}{m_i}} \quad (2.48)$$

and the total power loss,  $P_{lost}$  is given by equation (2.49)

$$P_{lost} = P_{ion} + P_{ex} + P_{wall} \quad (2.49)$$

where  $P_{ion}$  is the ionization power,  $P_{excite}$  is the excitation power and  $P_{wall}$  is the power lost by heating of the wall. Assuming representative values, the thrust is about 10mN. Using equation (2.46) the useful power is about  $P_{useful} \sim 70W$ . The specific impulse, which is given by  $I_{sp} = v_e / g$  was calculated to be about 1400 seconds.

Typically, the heat and radiation losses are negligible. The efficiency based on the wasted and useful energy evaluated above equates to about 60% assuming an electron temperature of 16eV.

## ***2.5 Summary of Chapter 2: Helicon Theory***

A helicon ion thruster was analyzed using nominal operating parameters achievable with Neodymium magnets. The goal was to evaluate whether such a system could provide comparable or more attractive performance characteristics than other EP technologies. Based on previous research, helicons are known for their efficient ionization, although the mechanism itself is still debated. For the low background pressures expected in space, a free-standing sheath is seen to form in the diverging magnetic field region. Referred to as a Single Layer, this provides an ion acceleration mechanism that simultaneously allows a neutralizing flow of electrons. The predicted specific impulse for the nominal design is 1400 seconds, with a thrust of 10 mN. Evaluation of the various loss mechanisms shows that ionization and excitation dominate with heat loading to the wall from ion and electron impact coming in third and Bremsstrahlung being completely negligible. The predicted efficiency of the system is 60%, which neglects losses from the power supply. This is comparable to existing EP technologies.

# Chapter 3: Design of Experiment

## 3.1 Helicon Source Dimensioning

The design parameters below are modeled after a paper by Chen<sup>23</sup>. Using the dispersion relation from equation (2.9)

$$\alpha = \frac{\omega \mu_o e n_o}{k B_o} \quad (3.1)$$

The phase velocity,  $\omega/k$  can be solved using equation (3.2)

$$\frac{\omega}{k} = \frac{T B_o}{\mu_o e n_o} \quad (3.2)$$

where the transverse wave number is given by the approximate boundary condition for the  $m = 0, m = 1$  modes to be

$$T = 3.83/a \quad (3.3)$$

The first two steps in the design process are 1) selecting the diameter of the tube and 2) determining the proper phase velocity  $\omega/k$  to promote efficient ionization. Once these parameters are determined, the remaining variables can be easily solved assuming first order harmonics. Since there is much debate over the mechanism for efficient ionization, the Landau damping hypothesis will be assumed since it provides a convenient relationship to establish the desired phase velocity of the helicon waves. In this case, one would choose a phase velocity to be near the desired velocity of the ionizing electrons<sup>23</sup>.

By assuming  $E_f$  to be the electron energy (in eV) for which the wave is to be matched to the phase velocity, the phase velocity is then given by equation (3.4)<sup>23</sup>

$$\frac{\omega}{k} = \left( \frac{2eE_f}{m} \right)^{1/2} = 5.93 \times 10^5 E_f^{1/2} \text{ ms}^{-1} \quad (3.4)$$

Using equations (3.3) and (3.4) in equation (2.9)

$$\frac{B_o}{n_o} = \left( \frac{2eE_f}{m} \right)^{1/2} \frac{\mu_o e}{3.83} a_{cm} = 31.2(10^{-13}) E_f^{1/2} a_{cm}$$

But, by defining  $n_{13} = \frac{n_o}{10^{13}}$  yields  $\frac{B_G}{n_{13}} = 31.2 E_f^{1/2} a_{cm}$ , where  $B_G$  is the magnetic field in Gauss,  $n_{13}$  is the scaled density in  $\text{cm}^3$ , and  $a_{cm}$  is the tube radius in cm. The ionization cross-section peaks at 50eV for an Argon discharge, resulting in

$$\frac{B_G}{n_{13}} = 31.2 E_f^{1/2} a_{cm} = 31.2(50eV)^{1/2} a_{cm} = 200 a_{cm} \quad (3.5)$$

So the phase velocity becomes  $\frac{\omega}{k} = 5.93 \times 10^5 E_f^{1/2} = 5.93 \times 10^5 (50eV)^{1/2} = 4.19 \times 10^6 \text{ ms}^{-1}$ . From equation (3.6) it is evident that  $B/n$  depends only on tube radius. According to Chen<sup>23</sup> this is the maximum density achievable, however the actual density depends on the available radio frequency power to overcome the losses.

The choice of frequency or wavelength is more flexible. The frequency is usually taken to be the industrial frequency of 13.56 MHz.

**Table 3.1:** *Approximate tube diameters as a function of frequency*<sup>23</sup>

<i>Approx diameter</i> (cm)	<i>Frequency</i> (MHz)
1.5	40.68
2	27.12
4	13.56
10	6.78
20	3.39

Table 3.1: Approximate tube diameters as a function of frequency, shows the harmonics and sub-harmonics of the frequency that would govern each choice of tube diameter. The plasma may choose its own diameter (smaller than the tube) if the frequency is not matched. Once the frequency is chosen then other parameters can be calculated. The wavelength is given by

$$\lambda = 5.93 \times 10^5 E_f^{1/2} / f \text{ m} \quad (3.6)$$

where  $f$  is the frequency in MHz. Equation (3.6) provides the necessary wavelength in order to design an antenna. In this case, a single turn helical antenna was constructed. Assuming a 50eV ionization potential for Argon and a frequency of 13.56MHz the antenna's wavelength was about 30cm. Equation (3.6) and Table 3.1: Approximate tube diameters as a function of provide only an estimate to determine how frequency varies with appropriate tube diameter. In future work, it would be interesting to observe how frequency affects the performance of a thruster.

### 3.2 Antenna Design

The antenna is another component of the thruster that is crucial for electromagnetic waves to propagate in the confined magnetized plasma. The antenna used was a single turn helix, due to its superior coupling characteristics. A helical antenna is more efficient in propagating a wave downstream since it is matched to the naturally dominant  $m=1$  mode. Figure (3.1) shows an image of the antenna.



**Figure 3.1** *Single Turn Helix Antenna with bus connectors*

The leads of the antenna were connected to a feedthrough (not shown) to deliver the power to support the plasma. The antenna's internal resistance must be calculated to determine whether or not it will draw significant power compared to the plasma. By “unfolding” the antenna [assuming it was a straight bar] it was easier to calculate the impedance. The impedance consists of a real and imaginary part. The real part is called the resistance and the imaginary part is

called the reactance and is related to the capacitance and the inductance. It is important to note that the reactance varies with frequency, unlike the resistance. The equation for impedance<sup>45</sup> is

$$Z = R + jX \quad (3.7)$$

Using equation (3.7) and assuming the antenna is ‘unfolded’ gives

$$Z = R + \underbrace{\frac{1}{\frac{1}{R_2} + \frac{1}{R_2}} + 2R + \frac{1}{\frac{1}{R_2} + \frac{1}{R_2}}}_{\text{Resistance}} + R + \underbrace{j\omega L}_{\text{Reactance}} = 4R + R_2 + j\omega L \quad (3.8)$$

where  $R$  denotes the resistance of the legs with bus connectors on the ends, and  $R_2$  is the resistance of half of each end ring. Applying the equation that governs the resistance of a conductor

$$R = \frac{\rho L}{A} \quad (3.9)$$

where,  $\rho$  is the resistivity,  $L$  is the length, and  $A$  is the area of the wire, the impedance becomes

$$Z = \underbrace{\frac{\rho}{A}[4l + l_2]}_{\text{Resistance}} + \underbrace{j\omega L}_{\text{Reactance}} \quad (3.10)$$

In addition, the skin depth of the helical antenna is approximately given equation is<sup>46</sup>

$$\delta \approx 503 \sqrt{\frac{\rho}{\mu_r f}} \quad (3.11)$$

where  $\mu_r$  is the relative permeability,  $f$  is the frequency and  $\rho$  is the resistivity. The relative permeability of copper is 1 and the RF frequency was fixed at 13.56MHz, so the skin depth is about 18 $\mu$ m.

Equation (3.10) is further simplified by neglecting the reactance terms. The reactance will be considered when discussing the matching network. The impedance becomes

$$Z = \frac{\rho}{wh} [4l + l_2] \quad (3.12)$$

Substituting in known values for the  $\rho, l, w, h$  where  $l$  is the length,  $w$  is the width and  $h$  is the height of the antenna, the resistive part of the impedance is found to be  $\sim 0.2 \text{ m}\Omega$ . Therefore, the internal resistance of the antenna is negligible and will not be considered in future calculations.

In addition, a digital LC meter was used to determine the inductance of the antenna. The inductance of the antenna was  $0.53 \mu\text{H}$  with  $\pm 1\%$  accuracy. The characteristic impedance of the antenna is therefore about  $Z \sim 45\Omega$ .

### ***3.3 Magnet Design***

The design consisted of using permanent magnets instead of electromagnets to generate similar field strengths. Neodymium magnets were used based on their strength and availability. The COMSOL<sup>48</sup> Multiphysics modeling program was used to model and analyze several magnetic configurations. The magnet sizes used in the design were compatible with the chosen tub diameter; however other engineering design considerations were examined which are mentioned in the next section. Each Neodymium magnet had an inner diameter of 38.1mm, an outer diameter of 76.2mm and a thickness of 6.35mm. Five magnets were used and configured in an array separated by 12.7mm Galorite (G-10) rods. Figure (3.2), shows a model of the five magnet array in COMSOL. The magnets surrounded a 35mm O.D. Pyrex tube. A quartz tube measuring 20mm (inner diameter) and 23mm (outer diameter) sat concentrically within the Pyrex. The Pyrex and quartz tubes were both 40cm long. The Pyrex tube was necked down on one end to a 6.35mm opening for the Argon gas feed line (shown in Figure 3.4).

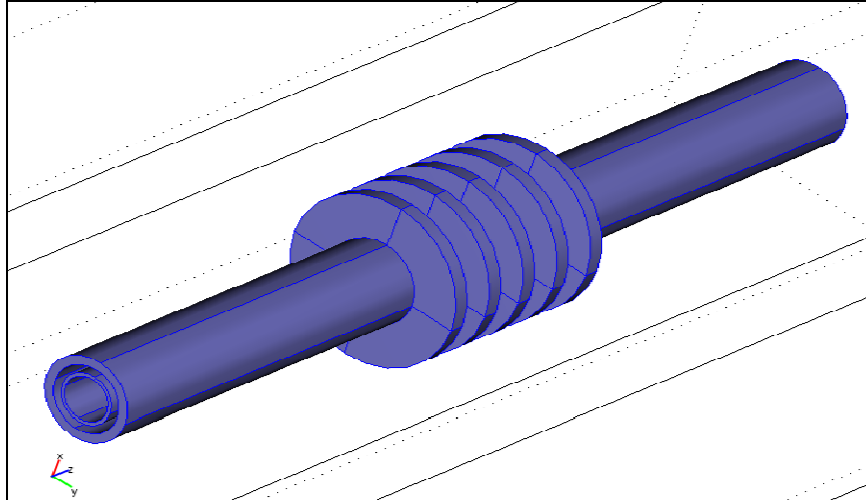


**Figure 3.2** *Five Neodymium Magnets encompassing with Pyrex (outer) and Quartz (inner) tube*

Figures (3.3) and (3.4) are the actual components used in the COMSOL model above. The G-10 spacers were designed accordingly to analysis; the tubes were designed to enable proper wave propagation and field generation.

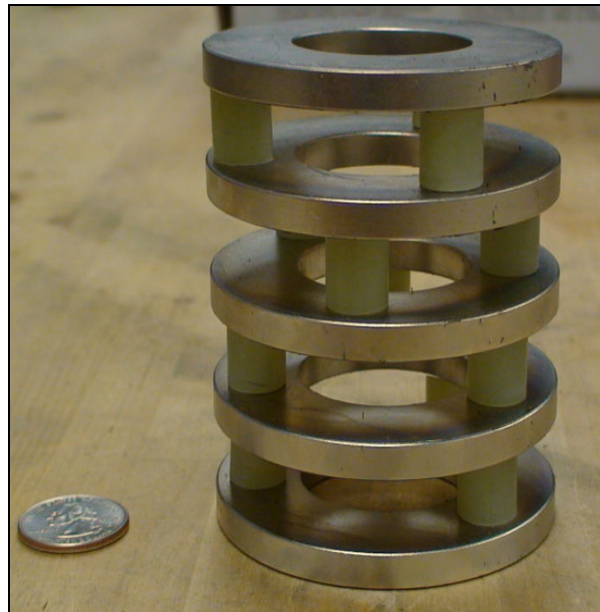


**Figure 3.3** *Stack of five Neodymium Permanent Magnets separated by G-10 spacers*



**Figure 3.4** Quartz Tube [Bottom] and Pyrex Tube with 1 1/4" hole [Top]

The difference between the field lines of permanent ring magnets and electromagnets is that the lines of a ring magnet will thread through the hole of the magnet in addition to around the outside. This causes a null field region on either side of the hole that can severely hinder plasma sustainment since ions would be lost to the walls. Once ions are lost, they must be regenerated and the efficiency decreases substantially. Therefore, it was decided that it would be advantageous to place the antenna downstream of the magnets to promote better ionization efficiency. Figure (3.5) shows the axial flux density along the length of the tube.

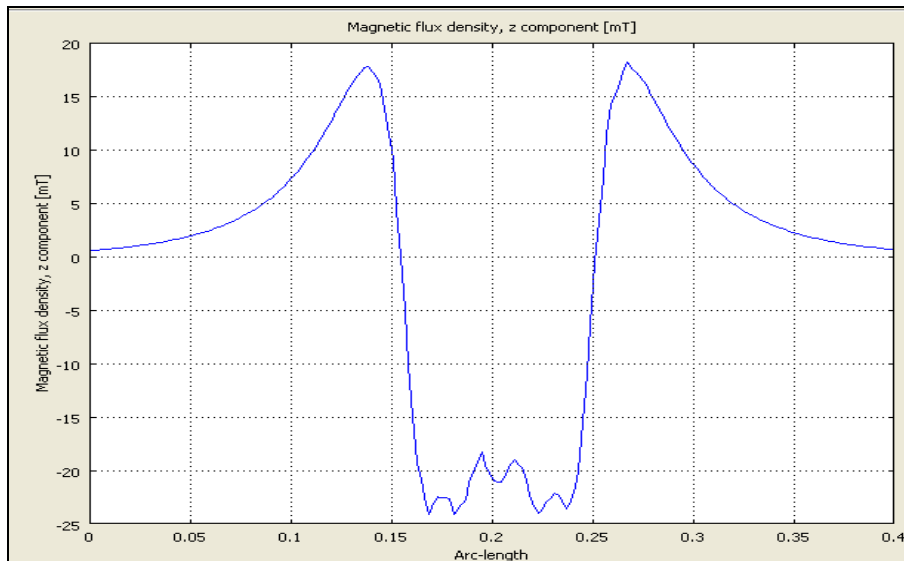


**Figure 3.5** Cross sectional line plot of the magnetic flux density along the z-direction

The null point can be perceived as a point where the flux goes to zero. This occurs 20 mm downstream from the magnetic array. The flux density inside the magnetic configuration is relatively uniform; there is only about a 10% variation between the magnets. This is because the magnet design was actually driven by the desire to make the field in this region uniform, before it was realized what detrimental effect the null regions would have on performance. Outside the configuration the magnetic flux drops off rapidly over a short range. From Figure (3.6), it is apparent that the streamlines are fairly axial at short distances from the antenna, but as the antenna is moved farther downstream it is less likely that the linear theory of helicon wave propagation would apply.

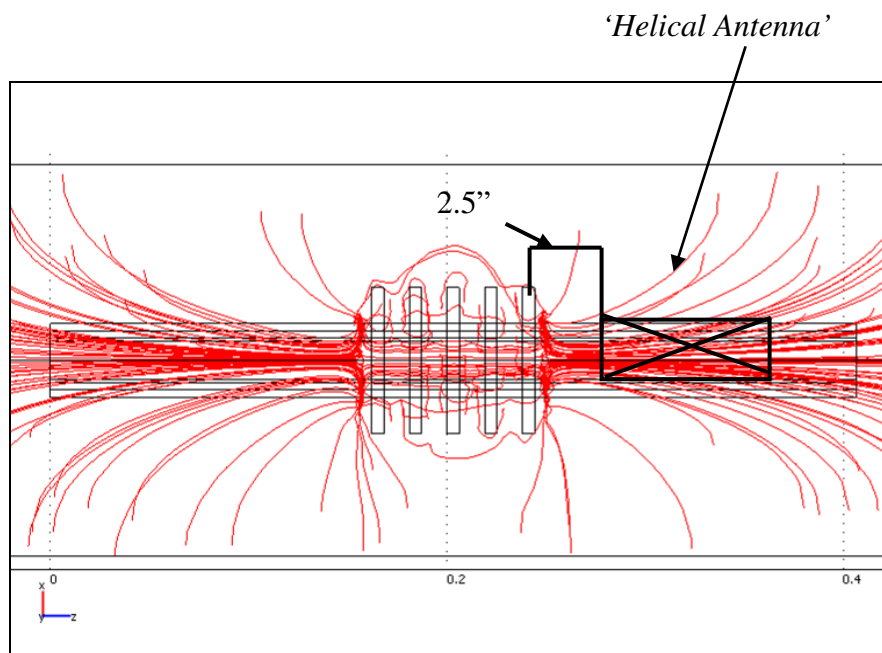


**Figure 3.6** *Streamlines in the x-z plane*

A 5180 Gauss meter with a 4in axial probe was used to experimentally check the magnetic strength of the configuration at various points for comparison to the COMSOL model. The probe completely submerged gave a reading of 30mT, which is about 20% less than the peak to peak reading given in Figure (3.5). The magnetic strength decreased approximately by 50% per inch as the probe was moved farther away. This agreed qualitatively well with the cross-sectional plot in Figure (3.5).

### 3.4 Facility Setup

The full experimental setup is shown schematically in Figure (3.7) below.

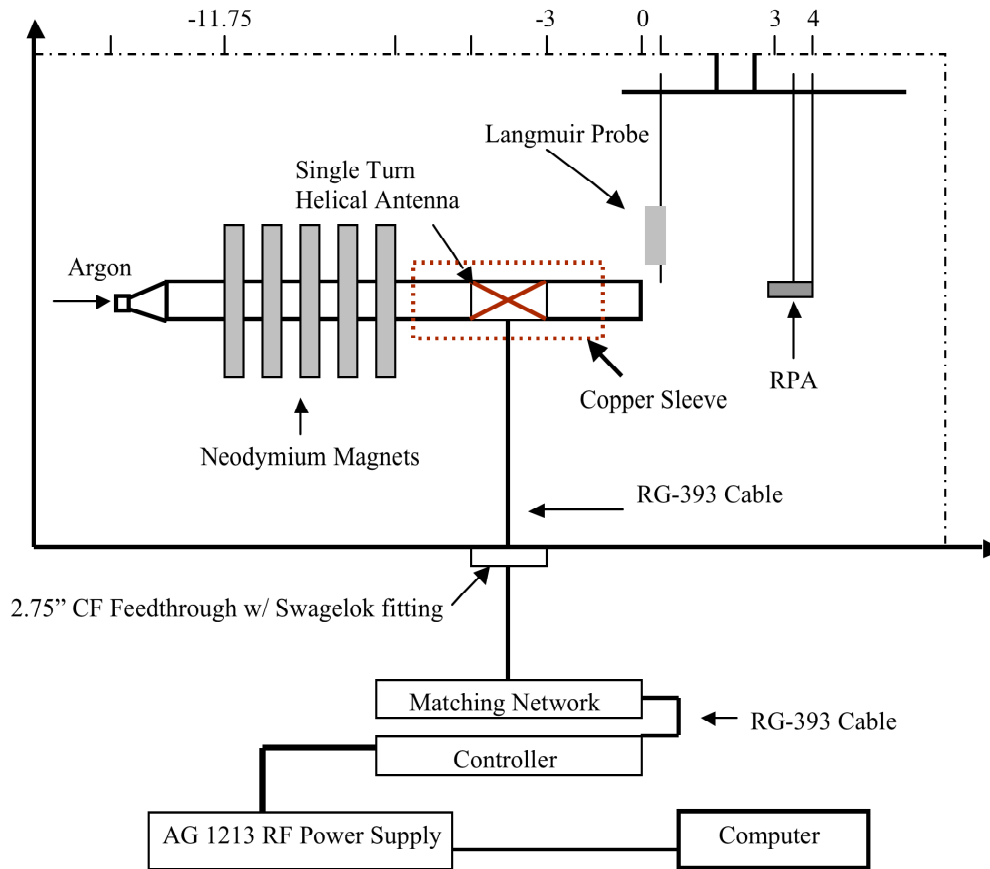


**Figure 3.7** Schematic of the Helicon Thruster [exit plane at  $z=0$ inch]

The helicon thruster was supported using an Aluminum stand (not shown in the schematic) inside the vacuum chamber, which is 60-cm in diameter and 1m in length. A Roughing pump and a Turbotronix NT 20 Controller were used to set the base pressure to  $1e-5$ mbar. A needle valve and flow regulator were used to control the rate of Argon flowing into the quartz tube. A 10mm polyvinyl tube connected to the end of the quartz tube and was fastened by a zip tie. In addition, a 13.5-cm long copper sleeve was placed downstream from the magnets (the dashed line in the schematic), which surrounded the Pyrex tube. A Resistive Thermal Device (RTD) device was attached to the sleeve in an attempt to measure the radiated power from the plasma.

The RPA and Langmuir probe were suspended from a 19mm diameter tube that was made adjustable to allow for the RPA and Langmuir Probe to be positioned accordingly.

A picture of the full setup inside the chamber is shown below in Figure (3.8).

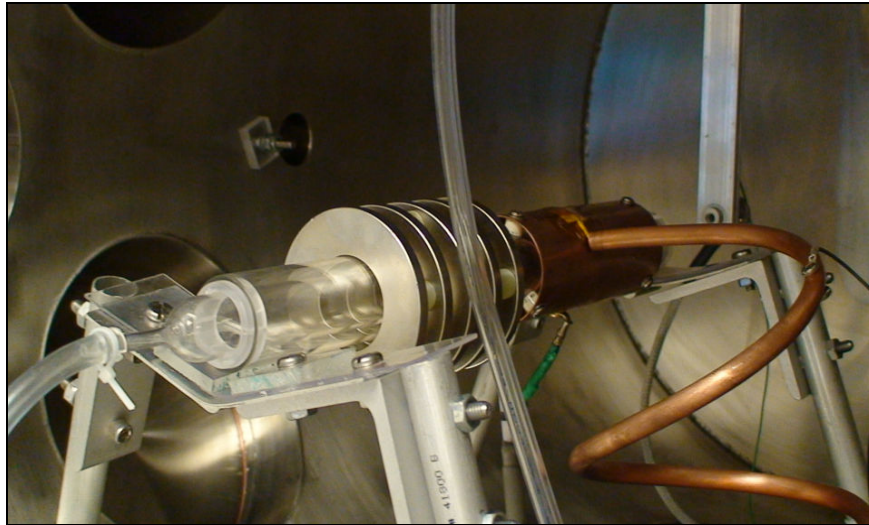


**Figure 3.8** *Helicon Thruster inside the SPPL Vacuum Chamber*

### **3.4.1 RF Power Supply and Matching Network**

An AG 1213W RF Power Source was used to deliver power to the helicon thruster as seen in Figure (3.9). An AIM/ATN Matching Network and the PT-II-CE controller were used for impedance matching. The magnitude and phase knobs were used to tune the response of the motors inside the matching network. The magnitude controlled the load capacitor and the phase controlled the tune capacitor. The tune and load capacitors could be either auto-tuned or manually tuned. This experiment used the auto-tune setting for simplicity. The matching network tries to find a ‘perfect match’ for which the reactance of the LC circuit cancel and the system becomes purely resistive. Therefore, the RF power supply will operate most efficiently when a 50ohm resistive load is connected to its output. The matching network tries to match this resistive load to properly load the transmission line.

Since the resistance of the plasma is on the order of 50-100milliohms, the load and tune capacitors need to find the proper reactance for plasma ignition. The capacitances that needed to be considered to find the proper reactance were from the RF feedthrough and the HN connector that was attached to the rear of the Matching Network [MN]. The cable between the MN and the

RF power supply was not considered part of the circuit, since its length was selected to transform whatever impedance was found at one end to the identical impedance at the other wave would 'stand' on the transmission line.

A graphical user interface (GUI) system was used to control the power input of the RF power supply. The system recorded the forward, reverse, load and requested power. The smaller the reflected power the better the match, so more power would be delivered to the thruster.



**Figure 3.9** AG-1213 RF POWER SUPPLY

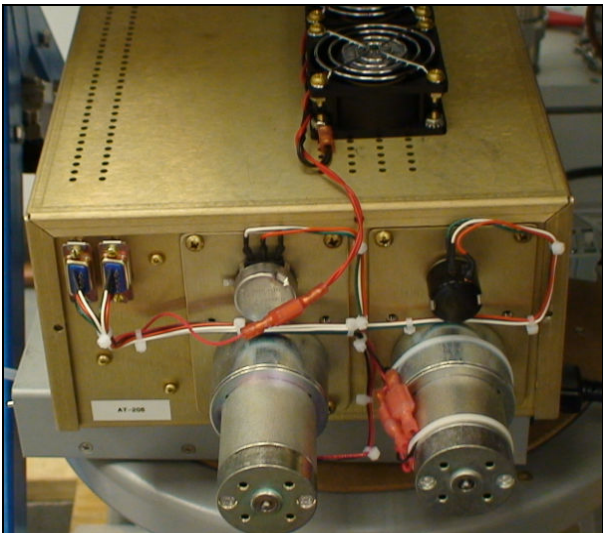


**Figure 3.10** AIM/ATN Matching Network

The controller typically was set in auto-tune, however, depending on the match, sometimes it would need to be controlled manually, to minimize reflected power. As mentioned, the load and tune capacitors can be preset by the phase detectors. This experiment did not set any pre-existing condition, although the detectors on the back of the MN were manually adjusted to optimize error reduction. Figure (3.11) shows the controller used for the MN.



**Figure 3.11** PT-II-CE Controller

### 3.4.2 RF Feedthrough

Due to much trial and error, it was determined that the best solution for connecting the matching network to the antenna, with the most efficiency, was running the cable directly into the chamber without any double-end connectors. Initially a BNC double-end connector was attached to a RG-213 cable, but due to heating, the system failed. Secondly, a similar concept was used, but instead of using coaxial cable, a single stranded copper wire was connected to the antenna. Plasma was being generated along the wire, which indicated that the system wasn't grounded properly. Attempts were made to ground the system, but failed to work correctly. Other systems were built and failed which will not be mentioned. Conceptually the idea of directly connecting the cable through the vacuum chamber was initiated through experience from previous attempts.

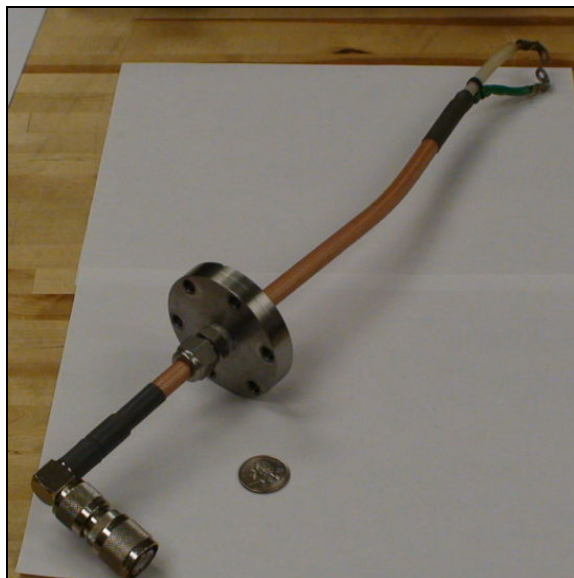


**Figure 3.12** *RF feedthrough with a single HN connector*

The Matching Network was connected to the single turn helical antenna via an RF feedthrough. The HN connector attached to the MN (see bottom left hand corner of Figure 3.12). Since the currents induced by the generator and the MN were on the order of 10 amps, RG 393 cable was used. The system was connected to the SPPL vacuum chamber using a 2.75" CF flange and a Swagelok compression fitting. The 3/8" Swagelok clamped down on the cable to provide a vacuum seal. In addition, vacuum grease was applied on the cable, since the mesh on the cable

was large enough for air to permeate. The end of the cable was attached to the antenna by 6.35mm ring connectors that were connected via brass screws for better electrical conductivity. Initially the end of the cable was soldered onto the antenna, but due to heating from the current, the solder melted. Figure (3.12) shows the final design RF feedthrough used in this experiment.

### 3.4.3 Electromagnetic Radiation

According to the Institute of Electrical and Electronics (IEEE) standards for RF radiation<sup>47</sup> for controlled environments the allowable radiated power density between 1-10MHz is 5mW/cm<sup>2</sup>.

The power radiated is given by

$$P_{rad} = \frac{1}{2} I^2 R_{rad} \quad (3.13)$$

Where  $I$  is the current, and  $R_{rad}$  is the radiation resistance, which is given by equation (3.14) for small dipoles

$$R = \frac{8\pi^5}{3} \sqrt{\frac{\mu_0}{\epsilon_0}} \left( \frac{r}{\lambda} \right)^4 \quad (3.14)$$

where  $r$  is the radius of the antenna, and  $\lambda$  is the wavelength of the radiation. The antenna radius is about 3cm, so at 13.56MHz, the radiation resistance is about 1μOhm. If 100Watts was being delivered to the plasma, then assuming a plasma resistance of 50mOhm, the radiated power would be only 2mWatts. Most of the chamber is stainless steel and would not allow any radiation of this frequency to penetrate, however there is one glass viewport, which would be about 30cm from the antenna. The power density at this viewport is then the total radiated power divided by the area of a sphere of radius 30cm. This results in a radiated power density of less than 2 mW/cm<sup>2</sup>, which is within acceptable limits.

It is important to be aware of electromagnetic radiation since it can cause tissue damage to humans. Therefore testing the helical antenna outside the SPPL vacuum chamber would be safe since the exposure is minimal. Furthermore, it is important to shield and maximize distance between the equipment to minimize RF interference.

### ***3.5 Retarding Potential Analyzer***

#### **3.5.1 Probe Description**

The Retarding Potential Analyzer (RPA) is a diagnostic instrument that measures the Ion Energy Distribution within the plasma. The RPA was built as an honors undergraduate thesis project by Marissa Intelisano. Figure (3.13) shows the RPA immersed in the SPPL vacuum chamber, and Figure (3.14) shows it compared to a quarter to get a sense for its size.



**Figure 3.13** *Plasma ignition at 100W using H<sub>2</sub>O, p = 2e-3mbar  
The RPA was positioned 3 inches away from the exit plane (upper right)*

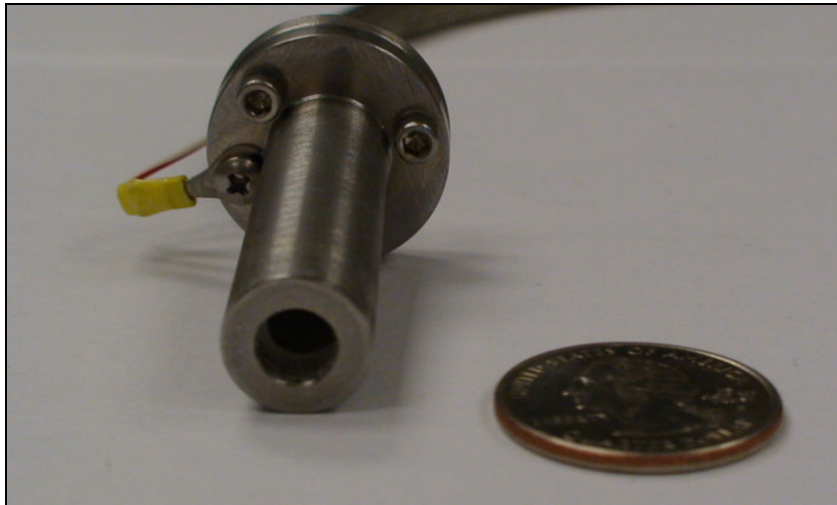


**Figure 3.14** *Retarding Potential Analyzer (RPA)*

The RPA was suspended by 3mm thick aluminum slabs and ceramic spacer inserts to prevent shorting between the RPA and ground. Wires were connected and shielded accordingly to provide voltage to the system and read the collected current with low noise characteristics. A cross-section of the RPA is shown below, where it can be seen to house 3 grids. The 1<sup>st</sup> grid is allowed to float in the plasma shield instabilities that might arise in the plasma due to wave phenomena. The 2<sup>nd</sup> grid is negatively biased to repel electrons and is fixed at -28V. The 3<sup>rd</sup> grid is the discriminator that is swept over a range of voltages to determine which ions will be allowed to reach the collector plate. Since only the particle energy is discriminated, the RPA is unable to distinguish between singly or multiply ionized particles. However, the equilibrium population of doubly ionized Argon is expected to be much lower than for Ar II.

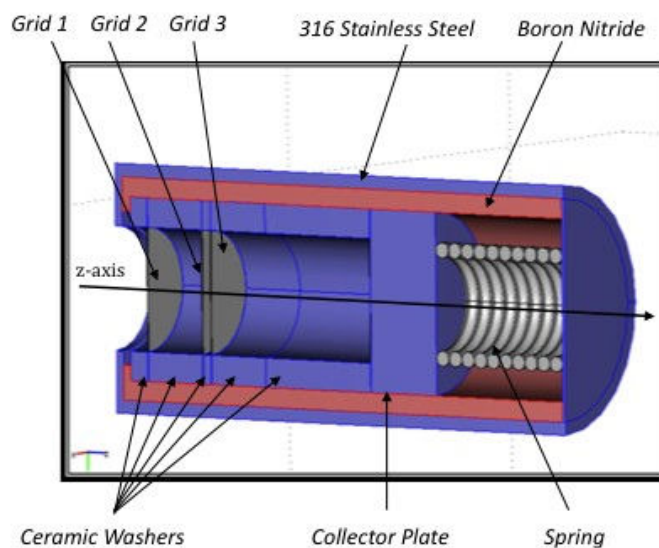


**Figure 3.15** Cross Section of the Retarding Field Potential Analyzer using COMSOL<sup>48</sup>

The design is based on a model by Azziz<sup>49</sup> and previously by Hofer<sup>50</sup>. The RPA designed consisted of 3 chemically etched molybdenum grids, separated by ceramic washers, a stainless steel collector plate and a boron nitride sleeve to act as an insulator. The electric connections consisted of 30 AWG copper wires that were aligned with the boron nitride sleeve. The resulting product had an outer diameter of 12.7mm, an inner diameter of 10.9mm and a length of 38.1mm. The inner sleeve was made of boron nitride and had an inner diameter of 8.8 mm, an outer diameter of 10.6mm and a length of 36.5mm. The collector plate was about 19mm downstream of the aperture.

The RPA was connected to several power supplies as shown schematically in Figure (3.16) below. The discriminator grid was conned to a Keithley 2410 SourceMeter so that it could be swept over the necessary range of potentials. The collector plate was connected to a Keithley 6485 PicoAmmeter to allow for precise measurement of the collected current.

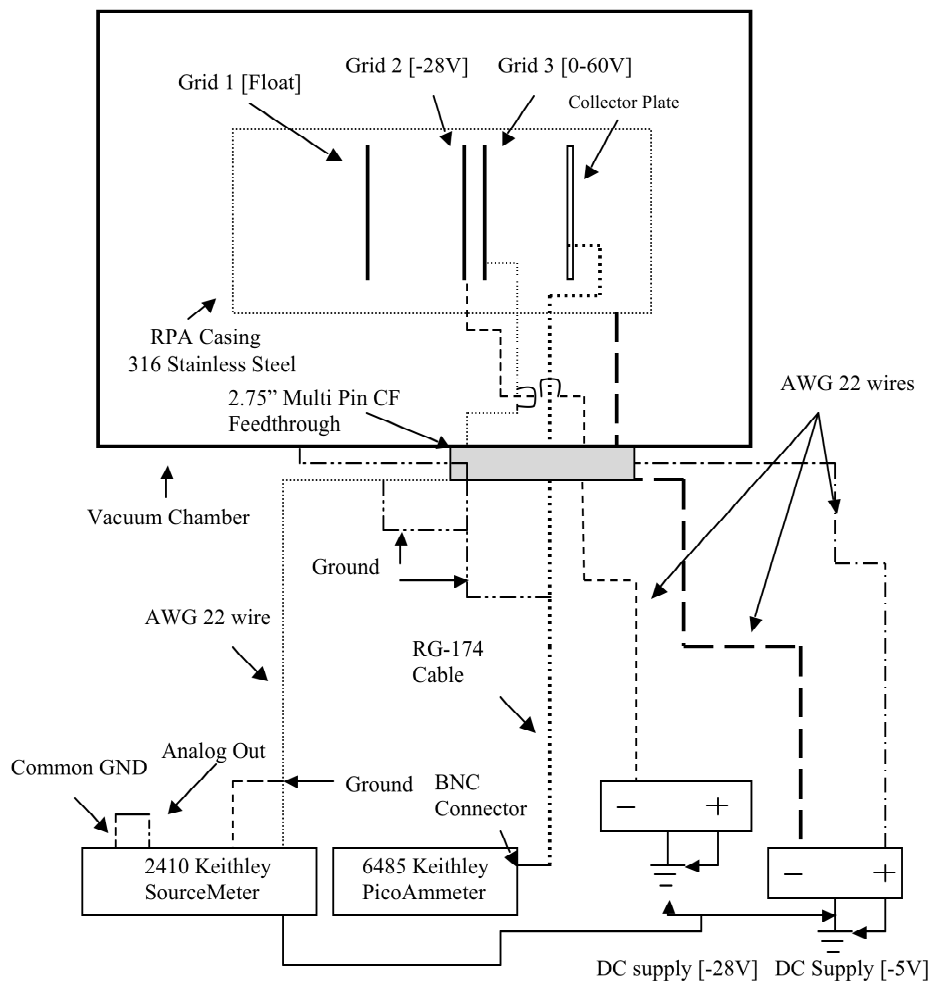


**Figure 3.16** *Detail Schematic of the Retarding Potential Analyzer and its components*

### 3.5.2 LabVIEW Interface

A LabVIEW program was written to sweep the voltage using a 2410 Keithley Source Meter and simultaneously acquire a current measurement, which was digitally displayed on a Keithley 6485 PicoAmmeter. The application program interface called in low level drivers that were provided by Keithley Instruments. A USB-RS232 converter was used to make a connection with

the Keithley 2410 SourceMeter and the Keithley 6485 PicoAmmeter. Both units were then connected using separate COM ports by a RS-232 cable. The drivers were imported from Keithley Instruments and were used to configure, initialize and measure the incoming currents by the PicoAmmeter for a given voltage that were being swept by the SourceMeter. The voltage was typically swept from 0-60V to obtain I-V curves. Two waveforms (not shown) captured the current the RPA collected for a given voltage. These waveforms were meshed to generate an I-V curve. The curve was then imported into Matlab for data analysis.

### ***3.6 Langmuir Probe***

#### **3.6.1 Probe Description**

The Langmuir probe, which was invented by American physicist Irving Langmuir during the early 20<sup>th</sup> century, uses a voltage scanning technique to measure electron temperature and density with an electrostatic probe. The probe shown in Figure (3.17) was made from a 1.6mm diameter tungsten rod and a 6.35mm diameter ceramic tube which acted as an insulator. Tungsten was used since it can sustain high temperatures. The original uncompensated probe was built and tested by Dustin Alinger, a graduate research assistant at the University of Maryland.

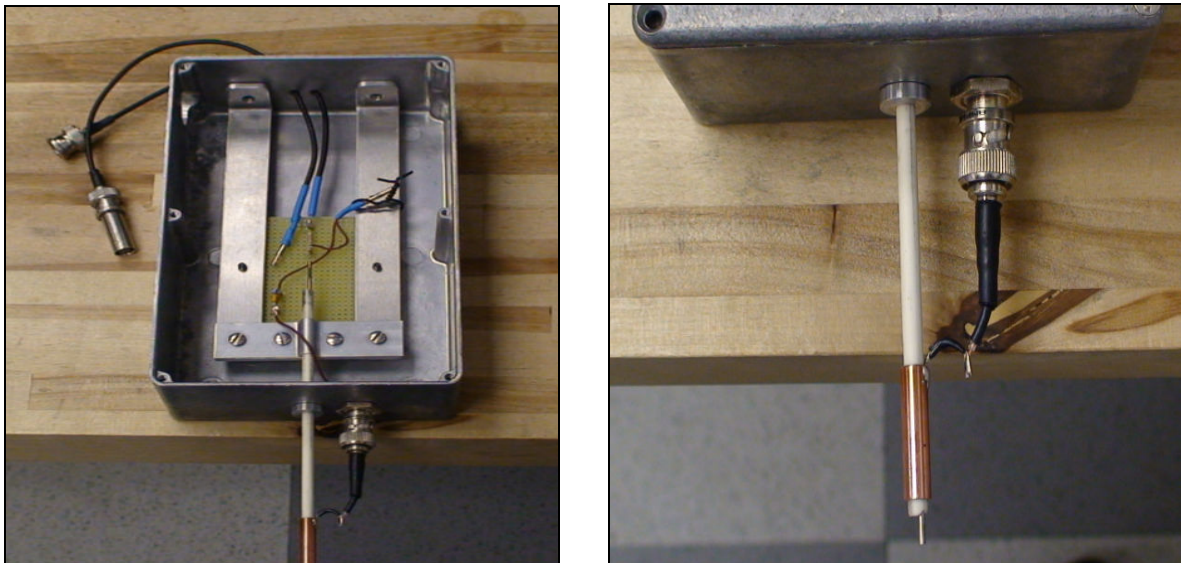


**Figure 3.17** *RF Compensated Langmuir Probe [with auxiliary electrode]*

RF compensation of the probe was implemented using theory by Chen<sup>51</sup>. An uncompensated probe tends to overestimate the electron temperature. In addition, a time-varying plasma potential<sup>52</sup> can distort the electron retarding region near the probe tip causing a shifting in floating potential. The compensated probe design used in this experiment is similar to one adopted by Godyak<sup>53</sup>. The method consisted of using an auxiliary electrode (see Figure (3.18)) which coupled to the Langmuir Probe to sample local fluctuations in the plasma. Placing the auxiliary electrode near the tip of the probe ensured that both electrodes were exposed to the same region of the plasma.

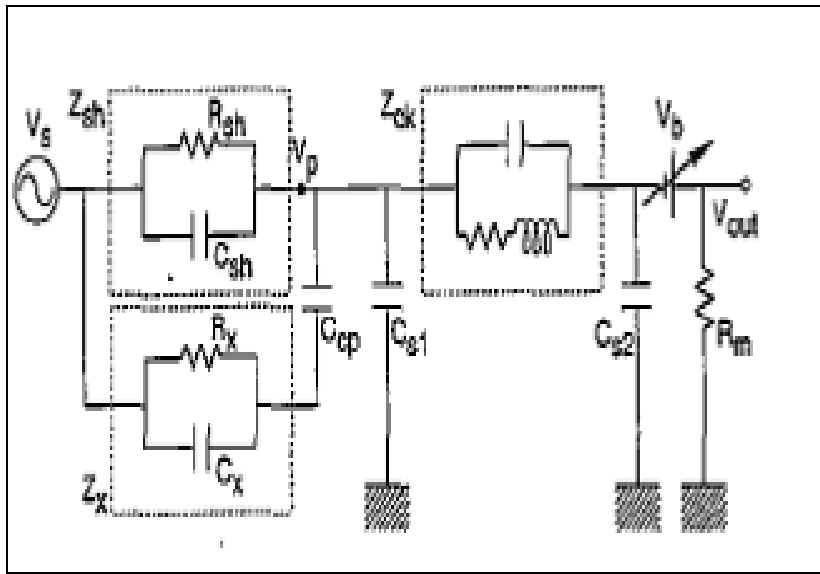


**Figure 3.18** Schematic of the RF Compensated Circuit<sup>51</sup>

Referencing Figure (3.18),  $V_b$  is the probe bias potential,  $V_p$  is potential at the tip and  $V_s$  is the space potential. The choke impedance  $Z_{ch}$  will consist of an inductor that satisfies a condition given by

$$Z_{s1} \approx Z_{ch} \gg Z_{sh} \left( \frac{e|V_{RF}|}{kT_e} - 1 \right) \quad (3.15)$$

where,  $Z_{s1}$  is the stray capacitance, and  $V_{RF}$  is the RF voltage. The RC circuit in series with the choke circuit represents the plasma, and the circuit adjacent to the sheath represents the

impedance of the auxiliary electrode, which is connected by a coupling capacitor. According to Chen<sup>51</sup> the effective sheath resistance is given by

$$\frac{1}{R_{sh}} = \frac{dI}{dV} \approx -\frac{dI_e}{dV} \quad (3.16)$$

Assuming an electron temperature and density, the ion current can be determined. The initial ion current was taken to be on the order of 1 mA. The assumed phase velocity was about 4000 m/s. In addition, the capacitance in the absence of  $V_{RF}$  is given by

$$C_o = \frac{\epsilon_o A_p}{2^{7/4} \lambda_D} \left[ \frac{e(V_{DC} - V_p)}{kT_e} \right]^{-3/4} \quad (3.17)$$

where,  $\epsilon_o$  is the emissivity,  $A_p$  is the probe area,  $\lambda_D$  is the Debye length,  $V_{DC}$  is the DC voltage,  $T_e$  is the electron temperature and  $V_p$  is the plasma potential. The capacitance in the absence of a RF voltage was taken to be on the order of pF at the floating potential. The sheath resistance had a magnitude of  $100\Omega$ . The primary stray capacitance  $C_{s1}$  was taken to be about 1.5pF from the choke to the probe tip. The secondary stray capacitance,  $C_{s2}$  from Figure (3.18) is given by the RF power supply. Assuming a 100W power input the minimum surface area factor for the auxiliary electrode was two, and is given by  $\frac{R_{sh}}{Z_{ch}}$  where  $R_{sh}$  is the sheath resistance and  $Z_{ch}$  is the choke impedance.

The area of the auxiliary electrode should be made larger than the tip area so the probe can be coupled to generate a *short* for RF signals, but small enough not to pass low frequency signals. The RF fluctuations through impedance  $Z_x$  from the electrode should be identical to the sheath impedance, but smaller in magnitude. The surface area of the electrode was chosen to be twenty times larger than the area of the probe tip. The coupling capacitor consisted of two 2200pF ceramics in parallel. The inductor modeled was a 100 $\mu$ H RF conformal inductor and its impedance was determined by ranging the frequency for a given capacitance. Impedance versus

frequency curve is shown in Figure (3.19) for the conformal inductor. The point where the curve crosses the frequency at 13.56MHz is the impedance of the inductor for this setup.

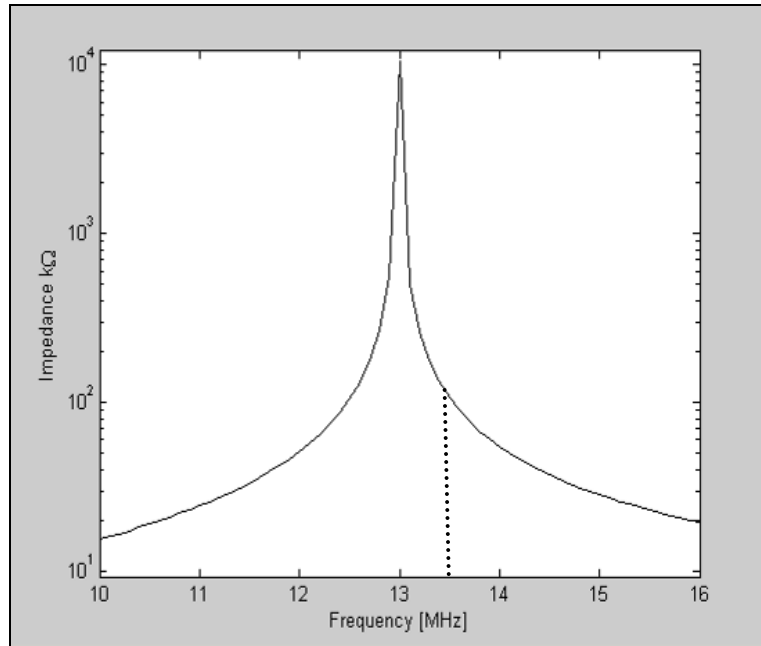


**Figure 3.19** Impedance vs. Frequency Curve for a 100µH RF Conformal Inductor

Using equation (3.18) the impedance of the inductor can be determined

$$Z = \frac{\omega L}{1 - \omega^2 LC} \tag{3.18}$$

The impedance of the 100µH inductor at 13.56MHz (fixed by the RF power supply), was about 100kΩ, which was larger than the impedance of the sheath as desired.

The auxiliary electrode was made of copper. The copper tube’s dimensions were 25.4mm long, 12.7mm in diameter, and had a wall thickness of 4.75mm.

Figure (3.20) shows a schematic of the Langmuir probe setup from inside the vacuum chamber extending to the 2410 Keithley SourceMeter that was used to sweep the voltage across the probe from -50-150V. The cable extended from the shielded box through the CF flange into the SourceMeter to reduce any reactive losses that could arise from RF. The shielded box that held

the circuit in place was set to float, since grounding the box caused instabilities that produced erroneous results.

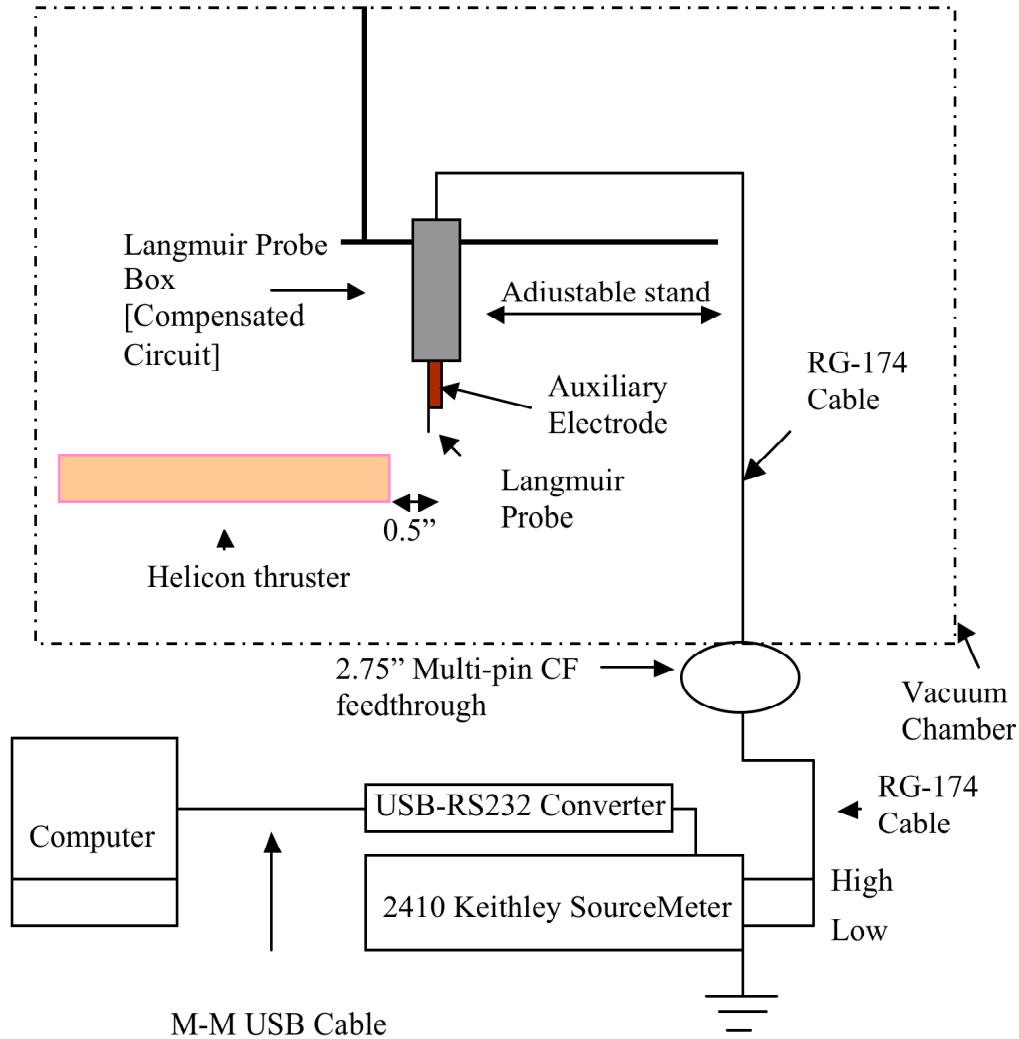


**Figure 3.20** Schematic of the Langmuir Probe Setup

### 3.6.2 LabVIEW Interface

The program for the Langmuir Probe used the same concept to call in low-level drivers. A USB-RS232 converter was used to make a connection with the Keithley 2410 SourceMeter. The unit was then connected using a COM port via a RS-232 cable. The drivers were imported from Keithley Instruments and were used to configure, initialize and measure the incoming currents

by the SourceMeter for a given voltage that was being swept by the SourceMeter. The voltage was typically swept from -50-150V to obtain I-V curves. The waveform (not shown) would capture the current the SourceMeter would collect for a given voltage swept. The waveform was then meshed to generate an I-V curve. The curve was then imported into Matlab for data analysis to measure the electron temperature and density.

### ***3.7 Gas Feed Systems***

Since Argon is a monatomic inert gas it was simpler to investigate for preliminary analysis purposes. Other gases that have been used recently are Xenon<sup>37</sup>, Hydrogen<sup>54</sup>, Helium<sup>55</sup>, and Nitrogen<sup>56</sup> to ignite plasma.



**Figure 3.21** *CONCOA 560 Series 150mm flow regulator*

The flow rate of the Argon gas was set to be at ten standard cubic centimeters per minute, which was found to provide the appropriate range of pressures during pumping. The Argon gas was controlled using a flow regulator as shown in Figure (3.21). A CONCOA needle valve was placed downstream of a CONCOA 560 Series 150mm flow regulator to reduce back pressure and also provide finer control of the operating pressures for plasma ignition.

In addition to Argon gas, water was also used as a propellant to ignite plasma. A small CO<sub>2</sub> tank was filled with water for this portion of the experiment. It was deduced that a large differential pressure head would cause the water to rapidly vaporize as it entered the vacuum chamber. A valve controlled the flow rate to stabilize the pressure in the chamber.

# Chapter 4: Testing

## 4.1 Retarding Potential Analyzer Data

### 4.1.1 Sample Measurements

As discussed in Chapter 3, the discriminator grid was connected to the Keithley Source meter, which swept the voltage between 0-60V. It was not necessary to sweep across a larger range because the I-V curve produced a Maxwellian distribution curve that matched theory quite well for higher pressures. Figures (4.1, 4.2, and 4.3) depict sample I-V curves and one of their derivatives over 3 runs for pressures at 8.5e-mbar, 4e-3mbar and 2e-3mbar respectively, with a forward power of 50W.

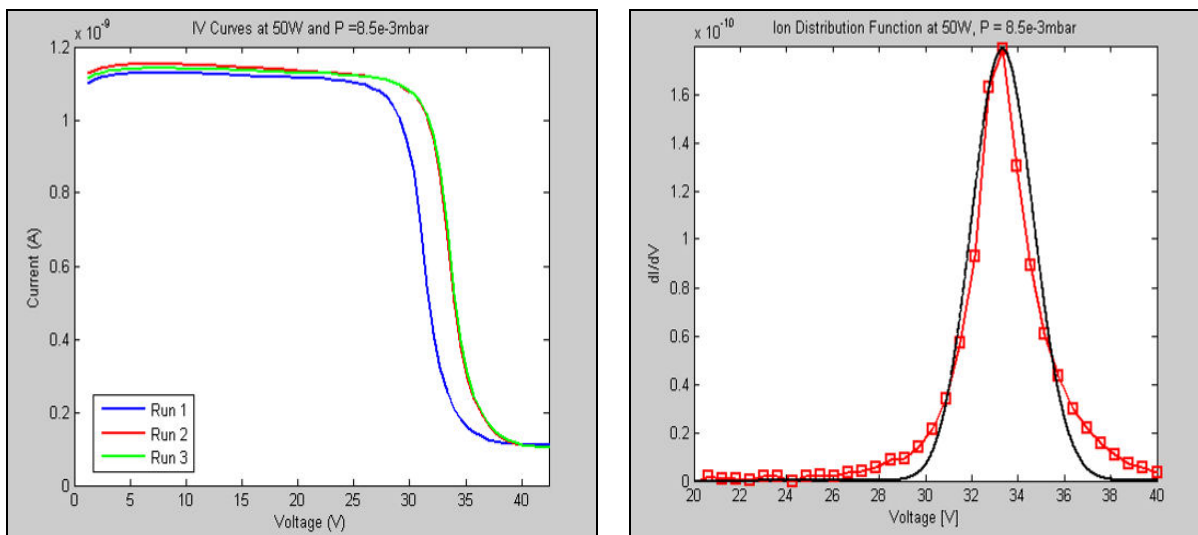


**Figure 4.1** I-V curve (left) and derivative (right) at 50W and 8.5e-3mbar

The derivative of the I-V curve was determined by central differencing, and shows the energy distribution of the ions. The shifted Maxwellian is indicative of an ion beam as is expected. The parameters of the beam will be found in Chapter 5. Full data sets can be found in Appendix A.

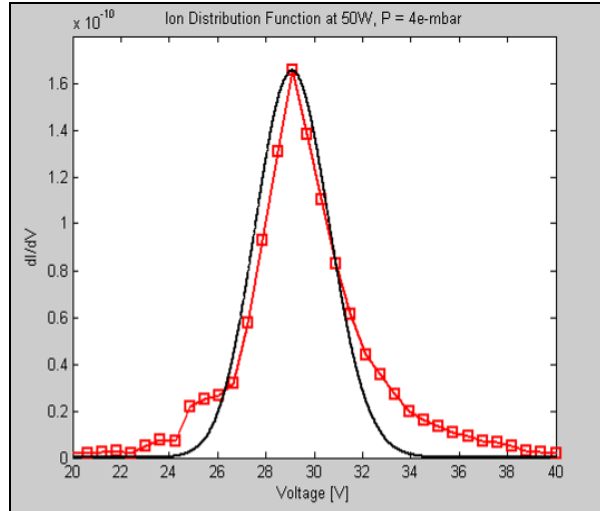
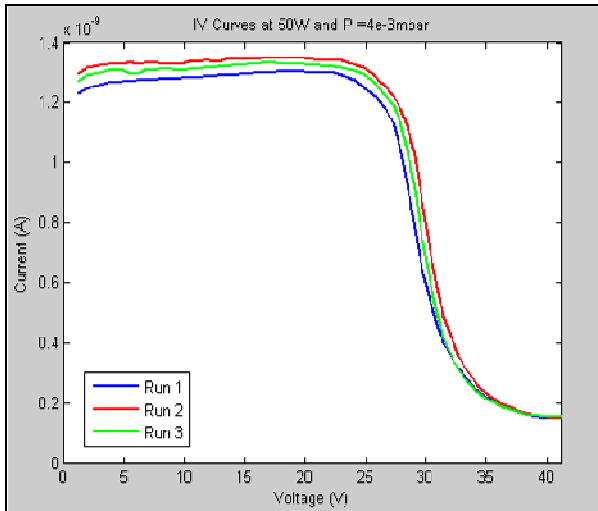


**Figure 4.2** *I-V curve (left) and derivative (right) at 50W and 4e-3mbar*

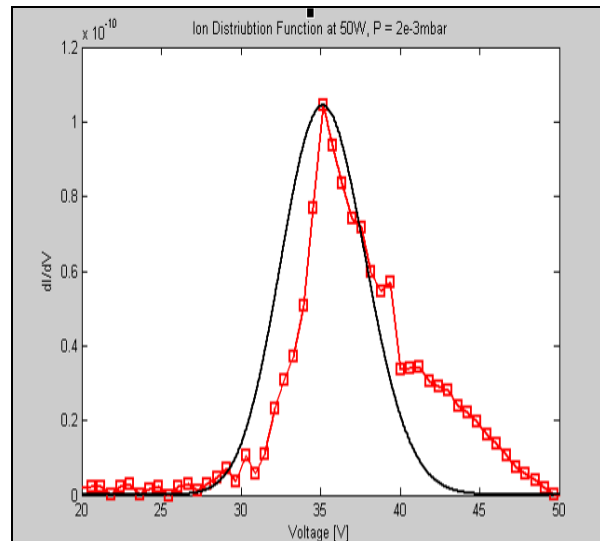
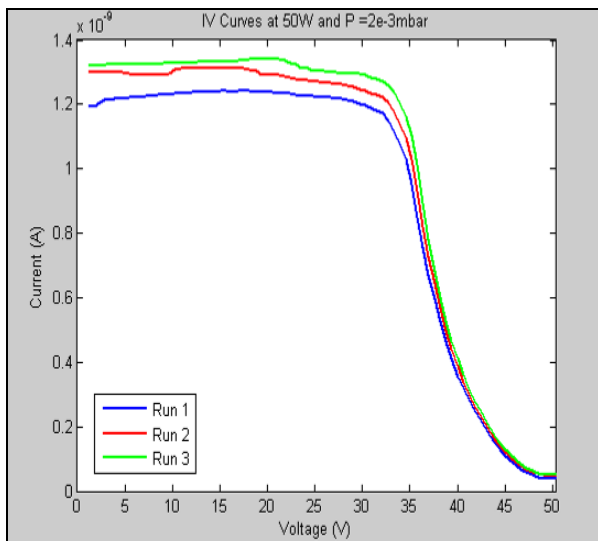


**Figure 4.3** *I-V curve (left) and derivative (right) at 50W and 2e-3mbar*

## 4.2 Langmuir Probe Data

### 4.2.1 Sample Measurements

Figures (4.4-4.7) show I-V curves and their respected Electron Energy Distribution Functions [EEDF] for an RF compensated and uncompensated Langmuir Probe at a forward power of 100W and a pressure of around 2mTorr. The uncompensated case tends to exhibit an indistinct knee, apparent when taking the semilog of the I-V curve. Typically, the uncompensated case overestimates the electron temperature. Sometimes the electron population region is not well defined so it is difficult to determine where to extrapolate the ion current to get the electron temperature.

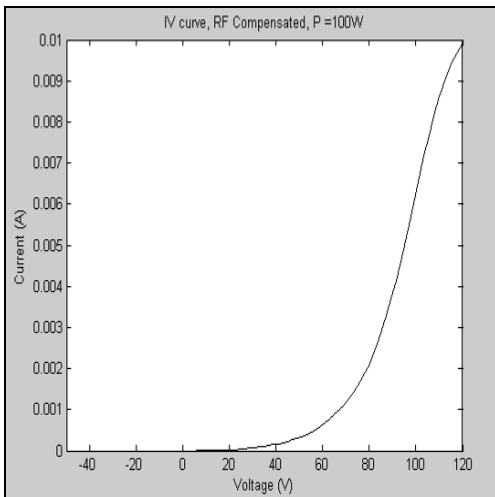


**Figure 4.4** I-V, RF Compensated Case

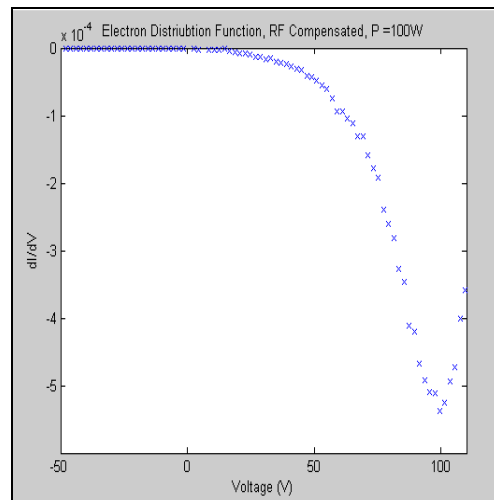


**Figure 4.5** EEDF, RF Compensated Case

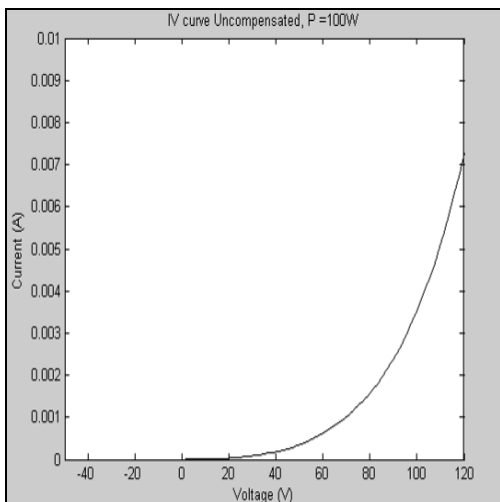


**Figure 4.6** I-V, Uncompensated Case

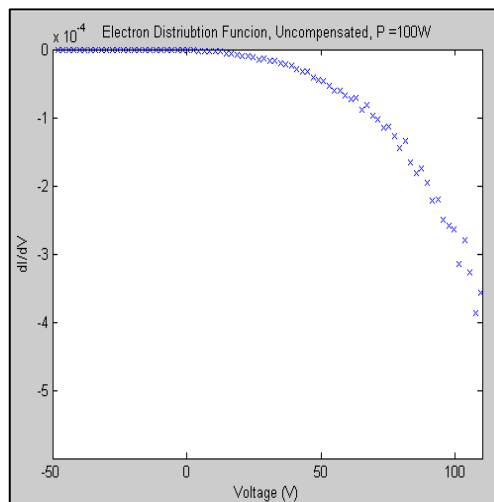


**Figure 4.7** EEDF, Uncompensated Case

### 4.3 Radiated Power

The RF Power was typically maintained below 150W to reduce thermal loading. However, a few runs were conducted at power levels up to 250 Watts. Images of these runs can be seen in Figure (4.8) below. Little variation is seen between 100W and 150W; however an increase in the plume can be seen at 200W. At 250W there is a significant increase in radiation along the entire length of the source tube.

Originally, a copper sleeve was introduced with the intent to directly measure radiated power from the source tube. However, it was discovered that due plasma being generated externally of the tube by the antenna, the heating of the sleeve was driven more by ion and electron impact than by radiation. To properly implement such a diagnostic it would be necessary to isolate the sleeve from the gas using a transparent boundary.

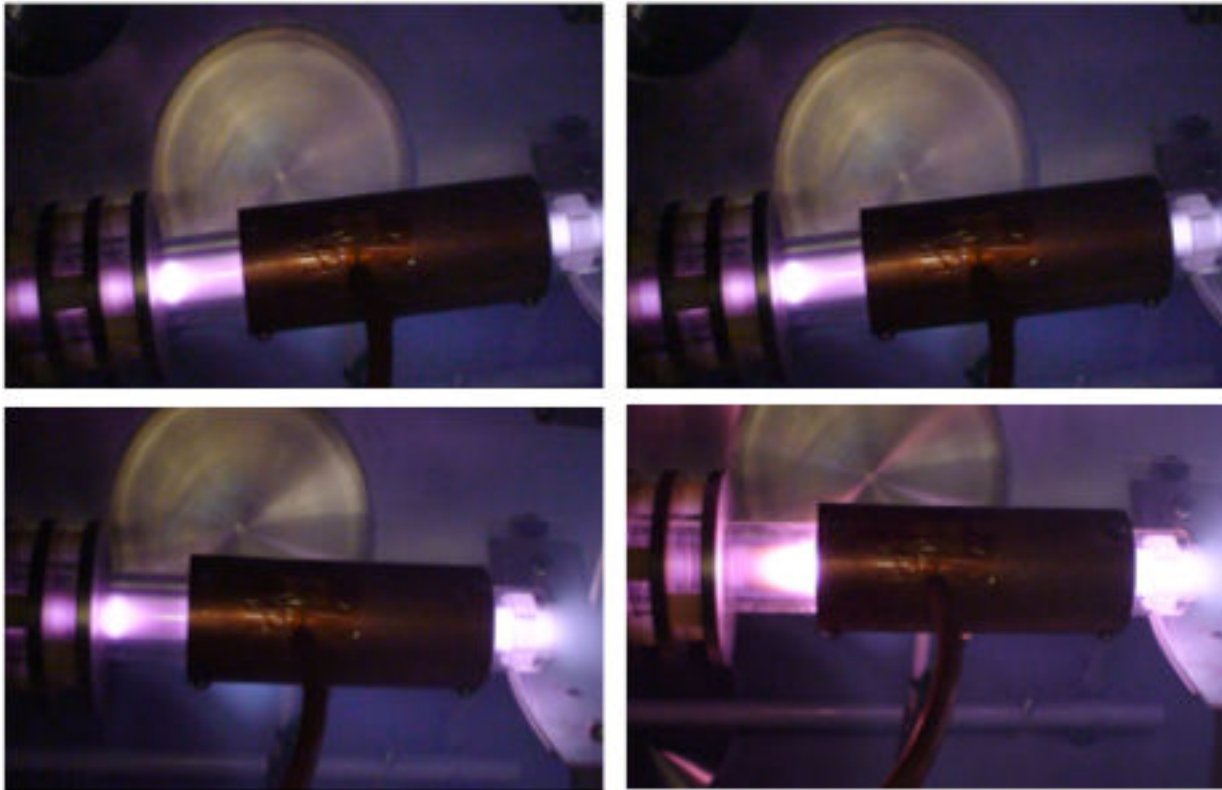


**Figure 4.8** Helicon Operation with Argon at 100W (upper left), 150W (upper right), 200W (lower left) and 250W (lower right).

#### ***4.4 Operation with Water Vapor***

Only two runs were conducted using water vapor to generate the plasma, and in the second run the Retarding Potential Analyzer was used to measure the characteristics plasma. Figure (4.9) shows plasma ignition using water vapor during the first run.



**Figure 4.9** *Plasma ignition using  $H_2O$ ,  $P = 150W$ ,  $p = 2e-3mbar$*

In the second run, the RPA was used to generate I-V curves that were similar to Argon however; there were noticeable peaks that arose through the transition region. Figure (4.10) is the I-V curve and Figure (4.11) is the ion energy distribution curve. The peaks are most likely the dissociation products of O, OH,  $H_2$ ,  $O_2$ , and  $H_2O$ . Without other instrumentation the composition of the plasma cannot be determined. In order to analyze the I-V curves, each peak would need to be fitted with a Maxwellian distribution for each constituent. Future studies will investigate the percent chemical composition breakdown of water using a mass spectrometry, optical spectroscopy or time of flight measurements to distinguish between particles of different species with the same energy.

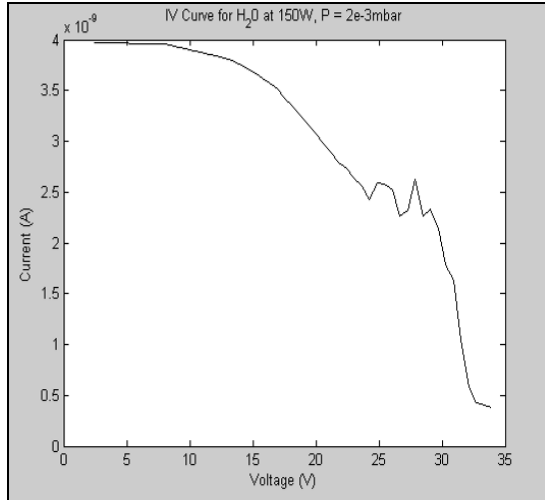


**Figure 4.10** *IV curve for H<sub>2</sub>O at P = 150W*

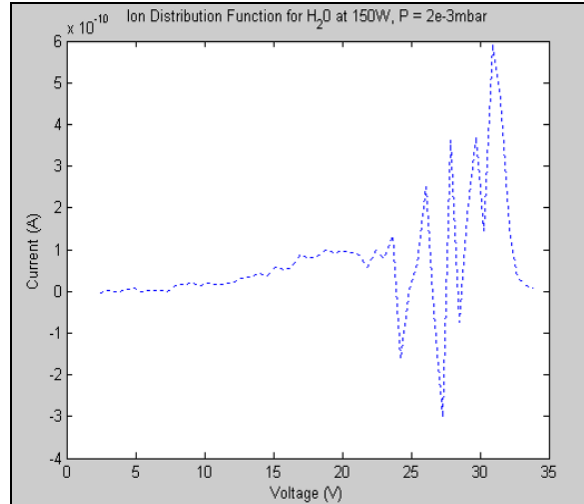


**Figure 4.11** *Ion Distribution Function for H<sub>2</sub>O*

# Chapter 5: Analysis of Results

## 5.1 Langmuir Probe

### 5.1.1 Standard Theory

The theory for analyzing Langmuir probe data is relatively straight-forward, however modifications are necessary in some circumstances, such as when the Debye length is large in comparison to the probe dimensions, or if neutral collisions play a factor in the sheath region around the probe. Barring these extremes, the standard probe theory would typically apply. There are 3 assumptions to this theory that Liebermann et al<sup>30</sup> characterized. First, the probe current does not disturb the plasma equilibrium. Secondly, the probe diameter is less than the electron mean free path. Lastly, the electrons are in thermal equilibrium, therefore, the particles will follow a Boltzmann distribution in the presence of an applied potential.

The application of the theory is best described in the context of a typical I-V curve, such as the one shown in Figure (5.1) below.

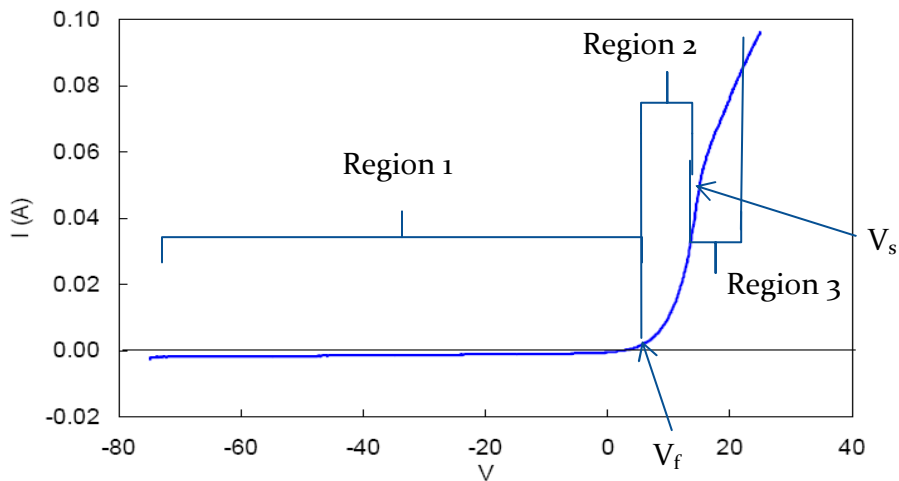


**Figure 5.1** Theoretical I-V curve for Langmuir Probe

The curve is divided into three regions. In region I, the bias voltage of the probe is much less than the plasma potential ( $V_s$ ) and the probe is mostly collecting ions. In region III, the bias

voltage of the probe is greater than the plasma potential and the probe collects mostly electrons. In region II, a near balance of the two currents exists, and the greater mobility of the electrons means that they will tend to dominate the variation of current with voltage. It is therefore expected that the I-V curve in region II will reflect the Boltzmann distribution characterized by the electron temperature. The floating potential is the potential at which the flux of ions and electrons are the same, so this is identified by the point at which the I-V curve crosses zero current. The plasma potential is near the upper knee of the curve and is sometimes found graphically or by looking at the derivative of the characteristic.

Near the floating potential, the sheath structure of the probe is nearly the same as for the sheaths that form at the walls of the vacuum chamber. Provided that the ion temperature is low in comparison to that of the electrons, the ion current collected by the probe is given by the Bohm current

$$I_{Bohm} = 0.6en_i \sqrt{\frac{kT_e}{m_i}} A_{probe} \quad (5.1)$$

In the ion saturation region, once the exponential drop in electron current makes it small in comparison to the ion current, this expression can be used to find the plasma density once the electron temperature has been found.

Above the floating potential, once the ion current can be neglected, the electron current can be found from the Boltzmann relation<sup>30</sup>

$$I_e(V) = I_{es} \exp\left(\frac{-e(V_s - V)}{kT_e}\right), \quad I_{es} = \frac{1}{4} en_e v_{e,th} A_{probe} \quad (5.2)$$

Taking the natural log of the first expression, and then differentiating with respect to  $V$  results in

$$\frac{d}{dV} \ln(I_e) = \frac{1}{T_{ev}} \quad (5.3)$$

where the electron temperature on the right is in electron volts. This allows for the electron temperature to be determined from the slope of the plot without explicit knowledge of the probe dimensions, provided all of the appropriate assumptions hold.

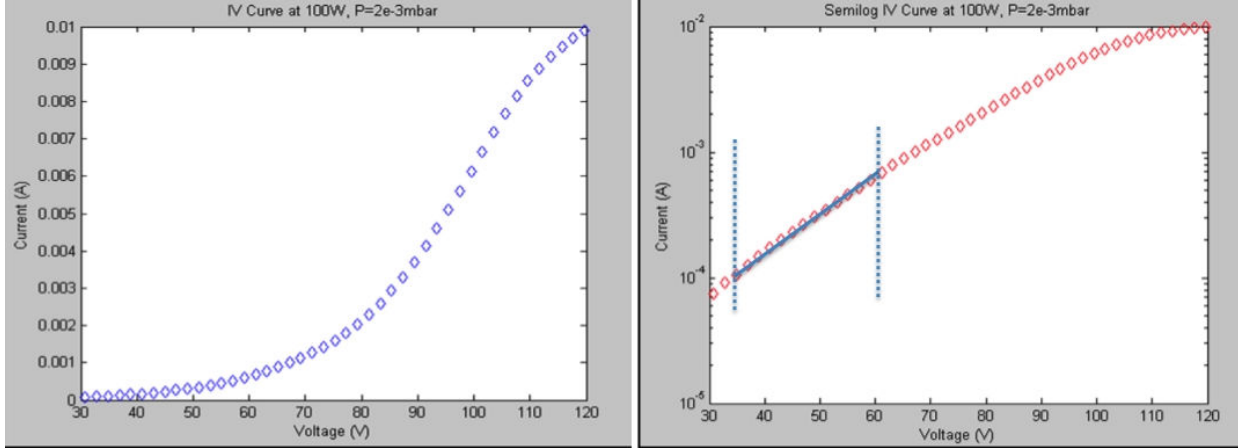


**Figure 5.2** (left) Average  $I$ - $V$  curve for Argon, at 100W, (right) Semi-log plot of  $I$ - $V$  curve

Figure (5.2) shows an example of the probe data taken for 100W forward power at a vacuum pressure of  $2(10^{-3})$  mbar. The slope of the curve is taken in the region show in the semi-log plot (right). The slope gives a value of 17 eV for the electron temperature, which is far above what would be expected inside the discharge tube. However, because the probe is downstream of acceleration region, it is likely that only the most energetic electrons from the discharge chamber would have reached this region.

As a check, the electron temperature can also be found by setting the electron and ion currents equal at the floating potential. This yields

$$\frac{1}{4}en_e v_{e,th} A_{probe} \exp\left(\frac{-e(V_s - V_f)}{kT_e}\right) = 0.6en_i \sqrt{\frac{kT_e}{m_i}} A_{probe} \quad (5.4)$$

and solving for the electron temperature (in electron volts)

$$T_{eV} = 2(V_s - V_f) \left[ 1 + \ln\left(\frac{m_i}{2\pi m_e}\right) \right]^{-1} \quad (5.5)$$

Given the plasma potential, floating potential and ion to electron mass ration, the electron temperature can therefore be found. The plasma potential can be found by taking the derivative of the I-V curve, which will inflect once the plasma potential is reached. This is shown in Figure (5.3), where the minimum at 100V corresponds to the inflection. While a value of 100 V for the plasma potential is itself somewhat troubling, the electron temperature that is obtained by inserting it into equation (5.5) is also 17 eV. For the uncompensated case, the Langmuir probe overestimated the electron temperature by 30%.

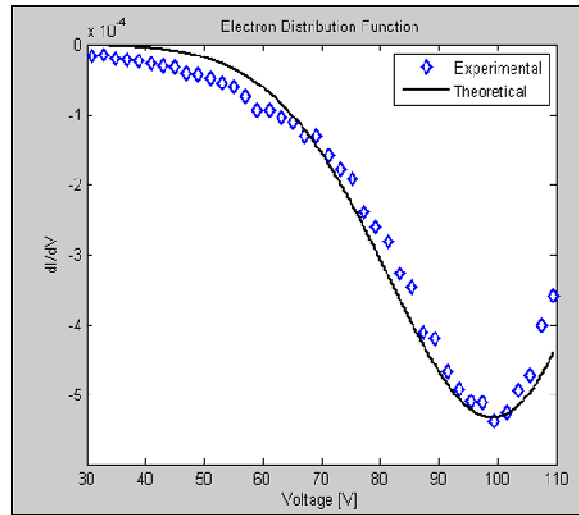


**Figure 5.3** Derivative of I-V plot at  $P = 100\text{W}$ ,  $p = 2e-3\text{mbar}$

### 5.1.1 Alternate Theory

Observation of Figure (5.3) leads one to consider if the electron current is actually the result of a shifted Maxwellian. This would be consistent with a high-energy beam of electrons coming out of the discharge tube. The assumed form of a shifted Maxwellian distribution function is given as<sup>57</sup>

$$f_b(v) = 1/v_b \sqrt{\pi} \exp(-(v-u)^2 / v_b^2) \quad (5.6)$$

where  $v-u$  is the shifted velocity of the distribution relative to the beam energy ( $u$ ), and the thermal velocity of the electrons is given by

$$v_b = (2eT_b / m)^{1/2} \quad (5.7)$$

where  $T_b$  is the temperature of the beam in electron volts, and  $m$  is the mass of electron. The beam current density is given by

$$j_b = \frac{n_b}{v_b \sqrt{\pi}} \int_{v_{\min}}^{\infty} \exp[-(v-u)^2 / v_b^2] v dv \quad (5.8)$$

Integrating and multiplying by the probe area yields the total beam current

$$I_b = A_p n_b \bar{v}_b [\exp(-y_m^2 / v_b^2) + u / v_b \sqrt{\pi} \operatorname{erfc}(y_m / v_b)] \quad (5.9)$$

where,  $\operatorname{erfc}$  is the complimentary error function and  $n_b$  is the beam density. The  $y_m$  term is given by  $y_m = v_m - u$ , and the average beam velocity is given by  $\bar{v}_b = v_b / 2\sqrt{\pi}$ . In terms of dimensionless quantities

$$\frac{u}{v_b} = \frac{V_p - V_s}{T_e} \quad \text{and} \quad \frac{v_m}{v_b} = \frac{V_p - V_f}{T_i} \quad (5.10)$$

Note the non-dimensional terms would be different for an ion distribution curve. Substituting the appropriate dimensionless terms into equation (5.9) yields the shifted Maxwellian shown in Figure (5.3). The distribution function is solved iteratively by matching the density, potential and electron temperature until the peak of the distribution is matched and the area under the curve matches within 1% error. Fitting this curve to the data results in a beam spread of 30eV, which is nearly twice what the electron temperature from the standard analysis predicts. However, the uncertainty in this value based on the error analysis (described in Appendix C) is 52%, which would not rule out the 17eV value arrived at previously. To relate these values back to the electron temperature inside the discharge, which will be more reliably found from the RPA analysis, the following approach was used.

Inside the discharge tube, the electrons are well approximated by a Maxwellian distribution, and only the highest energy electrons will be able to overcome the sheath potential and make it out to where the Langmuir probe is mounted. By finding the average energy of the electrons that make it through the sheath and assuming that they re-thermalize outside of the discharge tube,

an estimate of the electron temperature outside can be made and compared to the measured results.

The average kinetic energy of electrons that escape the discharge tube is given by

$$\overline{KE} = \frac{\int_{v_{\min}}^{\infty} \frac{1}{2}mv^2 f(v) dv}{\int_{v_{\min}}^{\infty} f(v) dv} \quad (5.11)$$

where  $m$  is the electron mass,  $v$  is the velocity,  $v_{\min}$  is the minimum velocity required to overcome the sheath potential and  $f(v)$  is the electron distribution function given by

$$f(v) = \sqrt{\frac{m}{2\pi KT_e}} \exp\left(\left(-\frac{1}{2}mv^2\right)/KT_e\right) \quad (5.12)$$

Equation (5.11) evaluates to

$$\frac{m}{4}c_e^2 \left\{ e^{-\phi/T} \sqrt{\frac{\pi}{4}} \left(\frac{\phi}{T}\right)^{1/2} + \frac{\pi}{4} \operatorname{erfc}\left(\frac{\phi}{T}\right)^{1/2} \right\} \left( \operatorname{erfc}\sqrt{\frac{\phi}{T}} \right)^{-1} \quad (5.13)$$

For Argon,  $\frac{\phi}{T} = 5.2$ , so that the average kinetic energy (KE) is given by  $\overline{KE} \sim 4.42 \frac{1}{2}mc_e^2$ ,

where thermal speed of the electrons is related to the electron temperature by  $\frac{8KT}{c_e} = \frac{8KT}{\pi m}$ .

Outside the discharge chamber, the average kinetic energy of the thermalized electrons is found by integrating over the entire velocity space

$$\overline{KE} = \int_{-\infty}^{\infty} \left(\frac{m}{2\pi KT}\right)^{3/2} e^{-1/2mv^2/KT} \frac{1}{2}mv^2 d^3v \sim \frac{3\pi}{8} \frac{1}{2}mc_e^2 \quad (5.14)$$

Setting the average kinetic energy of the electrons that escape the discharge chamber to the average kinetic energy of the thermalized electrons outside the discharge chamber allows for the temperatures in the two regions to be related. This results in

$$T_e^{out} = 3.75T_e^{in} \quad (5.15)$$

As will be seen in the next section, the electron temperature inside the discharge tube, as predicted by the ion beam energy is about 8eV for the same 100W forward power case that applied to the Langmuir probe data. Applying equation (5.15) predicts an electron temperature outside of about 30eV, which is consistent with the electrons having more of a beam structure.

Due to difficulties in acquiring the Langmuir probe data, the case that was analyzed is the only reliable data set that is available, so no additional data sets are included in the Appendices. As discussed in the future work section, a more completed set of data collection under a variety of operating conditions need to be acquired.

## ***5.2 Retarding Potential Analyzer***

### **5.2.1 Theory**

Analysis of the RPA data allows for the determination of the ion beam energy and its spread, the first of which provides for a direct measurement of the specific impulse. As discussed in Chapter 3, the ions are accelerated through the sheath potential, which is a function of the electron temperature and the ion and electron masses. A mono-energetic distribution of ions should be accelerated uniformly to a constant velocity downstream. However, the ions are not truly monoenergetic, and in fact they should have roughly the same temperature (velocity spread) as the neutral gas. This is due to the slow exchange of energy between the electrons and ions and the fact that the mechanism for energizing the plasma is to couple to the electrons first. It is expected that the energy spectrum of the ions will therefore be a narrow Maxwellian, shifted by some beam energy. This is the same assumption that was used in the modified analysis of the Langmuir probe, so what follows will look very similar.

A sample of the I-V curve and its derivative are shown in Figure (5.4) below. The  $dI/dV$  plot (or the Ion Energy Distribution Plot – IEDF) can be seen to have the shifted Maxwellian shape that was expected. The rest of the IEDF plots with their corresponding curve fits can be found in Appendix A.

The peak of the distribution was just taken as the maximum data point. Some attempts were made to identify the peak as a weighted average across the entire distribution, however as seen in Figure (5.4) the tails of the distribution will often have structures that do not follow the Maxwellian shape. These are real structures that indicate that collisions with the background gas are causing some spread in the distribution before it reaches the RPA. Detailed analysis of these structures was not implemented.

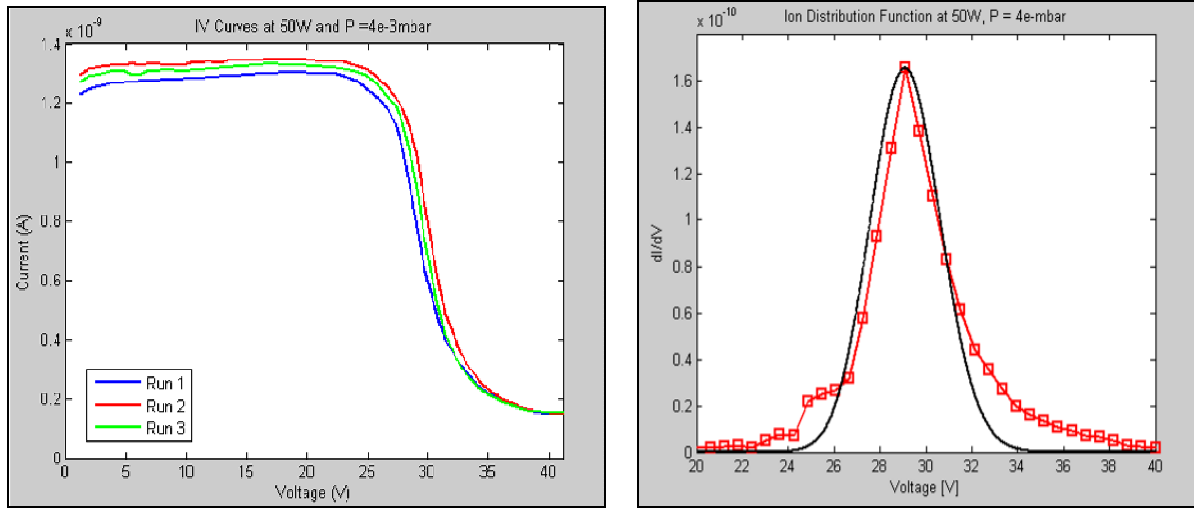


**Figure 5.4** *I-V curve (left) and derivative (right) at 50W and 4e-3mbar*

Once the peak of the distribution is located, the width must be found to establish the temperature of the distribution. The width was determined by two methods and was used to compute the ion temperatures. Method 1 compared the Full Width at Half Maximum, and Method 2 calculated the area under the distribution. It is clear that the area provided a more accurate depiction of the temperature since not all of the curves obeyed a strictly Maxwellian distribution.

The theory was calculated using a shifted Maxwellian distribution function

$$f(v) = A \exp\left(\frac{-m(v-u)^2}{2kT_i}\right) \quad (5.16)$$

However the data is in terms of voltage, so the voltage and velocity are related by

$$u = \sqrt{\frac{2q_i\phi}{m_i}} \quad (5.17)$$

where  $\phi$  is the voltage and  $q_i$  is the charge of an ion. Substituting equation (5.17) into (5.16) one obtains an equation for the  $dI/dV$  in terms of voltage, which is given by

$$-\frac{\partial I}{\partial \phi} = A \exp\left(-\beta\left(\sqrt{\phi} - \sqrt{\phi_b}\right)^2\right) \quad (5.18)$$

where  $T_i = 1/\beta$  (in eV) and  $\phi_b$  is the beam potential.

A Matlab program was written, (which can be found in Appendix B) to determine the ion temperature match this to each data set. Method 1 calculated the Full Width at Half Max by matching the experimental peaks with the theoretical equation and iteratively solving for the width until the condition was satisfied to within 1%. Method 2 calculated the area under both curves by summing their differences and finding the error between both curves until the error was within 1%. The error analysis associate with both of these methods is presented in Appendix C.

### 5.2.1 Results and Discussion

The results of the two analyses are shown in Tables (5.1) and (5.2) below. Because the distribution was found as a result of taking a finite difference, the accuracy of the resulting  $dI/dV$  values was determined by the resolution with which the data was taken, rather than the resolution of the instrument. For the case of RPA runs the uncertainty is 0.6 Volts. The peak of the distribution was defined as the maximum point, so the error in determining this location is the 0.6V data resolution. This also translates directly into the uncertainty in the electron temperature in the source tube, since the voltage has a much greater uncertainty than any of the physical constants.

**Table 5.1** Ion temperature and ion beam energy at 50, 100, 150W and pressures at 8.5e-3, 4e-3, and 2e-3mbar using the Full Width Half Maximum Method

FULL WIDTH HALF MAXIMUM METHOD					
POWER	RUN	PRESSURE [mbar]	T <sub>i</sub> [eV]	T <sub>e</sub> [eV]	Beam Energy [eV]
50W	1	8.50E-03	0.020 +/- 0.013	5.9 +/- 0.6	30.9 +/- 0.6
	2	8.50E-03	0.019 +/- 0.012	6.3 +/- 0.6	32.7 +/- 0.6
	3	8.50E-03	0.018 +/- 0.012	6.4 +/- 0.6	33.3 +/- 0.6
	1	4.00E-03	0.035 +/- 0.018	5.5 +/- 0.6	28.5 +/- 0.6
	2	4.00E-03	0.032 +/- 0.017	5.7 +/- 0.6	29.7 +/- 0.6
	3	4.00E-03	0.033 +/- 0.017	5.6 +/- 0.6	29.1 +/- 0.6
	1	2.00E-03	0.080 +/- 0.024	6.8 +/- 0.6	35.1 +/- 0.6
	2	2.00E-03	0.064 +/- 0.022	6.9 +/- 0.6	35.8 +/- 0.6
	3	2.00E-03	0.049 +/- 0.019	6.9 +/- 0.6	35.8 +/- 0.6
100W	1	8.50E-03	0.052 +/- 0.020	6.3 +/- 0.6	33.9 +/- 0.6
	2	8.50E-03	0.040 +/- 0.017	6.8 +/- 0.6	35.1 +/- 0.6
	3	8.50E-03	0.038 +/- 0.017	6.8 +/- 0.6	35.1 +/- 0.6
	1	4.00E-03	0.040 +/- 0.017	6.9 +/- 0.6	35.8 +/- 0.6
	2	4.00E-03	0.036 +/- 0.016	6.9 +/- 0.6	35.8 +/- 0.6
	3	4.00E-03	0.038 +/- 0.017	6.9 +/- 0.6	35.8 +/- 0.6
	1	2.00E-03	0.026 +/- 0.013	7.5 +/- 0.6	38.8 +/- 0.6
	2	2.00E-03	0.024 +/- 0.013	7.5 +/- 0.6	38.8 +/- 0.6
	3	2.00E-03	0.025 +/- 0.013	7.5 +/- 0.6	38.8 +/- 0.6
150W	1	8.50E-03	0.052 +/- 0.034	10.4 +/- 0.6	53.9 +/- 0.6
	2	8.50E-03	0.057 +/- 0.022	9.9 +/- 0.6	51.5 +/- 0.6
	3	8.50E-03	0.051 +/- 0.016	9.8 +/- 0.6	50.9 +/- 0.6
	1	4.00E-03	0.050 +/- 0.017	9.1 +/- 0.6	47.2 +/- 0.6
	2	4.00E-03	0.049 +/- 0.016	9.1 +/- 0.6	47.2 +/- 0.6
	3	4.00E-03	0.047 +/- 0.016	9.1 +/- 0.6	47.2 +/- 0.6
	1	2.00E-03	0.023 +/- 0.011	9.7 +/- 0.6	50.3 +/- 0.6
	2	2.00E-03	0.022 +/- 0.011	9.7 +/- 0.6	50.3 +/- 0.6
	3	2.00E-03	0.022 +/- 0.011	9.7 +/- 0.6	50.3 +/- 0.6

Referring to Figure (5.5), a clear trend can be seen whereby the beam energy (and hence the corresponding electron temperature) increases with power. However, of more interest is that for the high pressure case in particular, there is only a modest increase from 50W to 100W, but a significant increase from 100W to 150W. A possible explanation for this is that the gas is not fully ionized between 50W and 100W, so that any additional power supplied goes into increasing the level of ionization. Once the gas is fully ionized, further increase in power input goes fully into increasing the electron temperature. One would expect this trend to be more prevalent at the higher pressures since there is a higher density of neutrals to be ionized, whereas at the lower pressures nearly full ionization may be present even at the 50W level. There is a re-ordering of beam powers at different pressures as the input power is increased,

however this is comparable to the 95% confidence level indicated on the data, so no clear trend can be deduced.

**Table 5.2** Ion temperature and ion beam energy at 50, 100, 150W and pressures at 8.5e-3, 4e-3, and 2e-3mbar using the Area Method

AREA METHOD					
POWER	RUN	PRESSURE [mbar]	T <sub>i</sub> [eV]	T <sub>e</sub> [eV]	Beam Energy [eV]
50W	1	8.50E-03	0.028 +/- 0.000	5.9 +/- 0.6	30.9 +/- 0.6
	2	8.50E-03	0.029 +/- 0.000	6.3 +/- 0.6	32.7 +/- 0.6
	3	8.50E-03	0.027 +/- 0.000	6.4 +/- 0.6	33.3 +/- 0.6
	1	4.00E-03	0.049 +/- 0.000	5.5 +/- 0.6	28.5 +/- 0.6
	2	4.00E-03	0.048 +/- 0.000	5.7 +/- 0.6	29.7 +/- 0.6
	3	4.00E-03	0.043 +/- 0.000	5.6 +/- 0.6	29.1 +/- 0.6
	1	2.00E-03	0.105 +/- 0.000	6.8 +/- 0.6	35.1 +/- 0.6
	2	2.00E-03	0.104 +/- 0.002	6.9 +/- 0.6	35.8 +/- 0.6
	3	2.00E-03	0.091 +/- 0.002	6.9 +/- 0.6	35.8 +/- 0.6
100W	1	8.50E-03	0.066 +/- 0.001	6.3 +/- 0.6	33.9 +/- 0.6
	2	8.50E-03	0.051 +/- 0.000	6.8 +/- 0.6	35.1 +/- 0.6
	3	8.50E-03	0.049 +/- 0.000	6.8 +/- 0.6	35.1 +/- 0.6
	1	4.00E-03	0.054 +/- 0.001	6.9 +/- 0.6	35.8 +/- 0.6
	2	4.00E-03	0.050 +/- 0.001	6.9 +/- 0.6	35.8 +/- 0.6
	3	4.00E-03	0.053 +/- 0.001	6.9 +/- 0.6	35.8 +/- 0.6
	1	2.00E-03	0.048 +/- 0.001	7.5 +/- 0.6	38.8 +/- 0.6
	2	2.00E-03	0.045 +/- 0.001	7.5 +/- 0.6	38.8 +/- 0.6
	3	2.00E-03	0.048 +/- 0.001	7.5 +/- 0.6	38.8 +/- 0.6
150W	1	8.50E-03	0.081 +/- 0.014	10.4 +/- 0.6	53.9 +/- 0.6
	2	8.50E-03	0.096 +/- 0.014	9.9 +/- 0.6	51.5 +/- 0.6
	3	8.50E-03	0.073 +/- 0.008	9.8 +/- 0.6	50.9 +/- 0.6
	1	4.00E-03	0.060 +/- 0.003	9.1 +/- 0.6	47.2 +/- 0.6
	2	4.00E-03	0.058 +/- 0.003	9.1 +/- 0.6	47.2 +/- 0.6
	3	4.00E-03	0.056 +/- 0.003	9.1 +/- 0.6	47.2 +/- 0.6
	1	2.00E-03	0.038 +/- 0.002	9.7 +/- 0.6	50.3 +/- 0.6
	2	2.00E-03	0.037 +/- 0.002	9.7 +/- 0.6	50.3 +/- 0.6
	3	2.00E-03	0.038 +/- 0.002	9.7 +/- 0.6	50.3 +/- 0.6

The ion temperature estimated by the area method (Table 5.2) can be seen to have less uncertainty than when estimated by the full-width-half-max method (Table 5.1), so the following discussion will refer to the area method data. For reference, the neutral gas coming into the system would have been at room temperature, or about 0.025 eV. The fact that all of the ion temperatures are very near to this value is an excellent indicator that the instrument, while uncalibrated with regard to total collected current is operating properly.

Trend analyses of the ion temperature can be done in terms of power and pressure dependence. Generally, one might expect that even though the rate of energy transfer between the electrons and the ions is slow, a slight increase in ion temperature should be seen as the power increases.

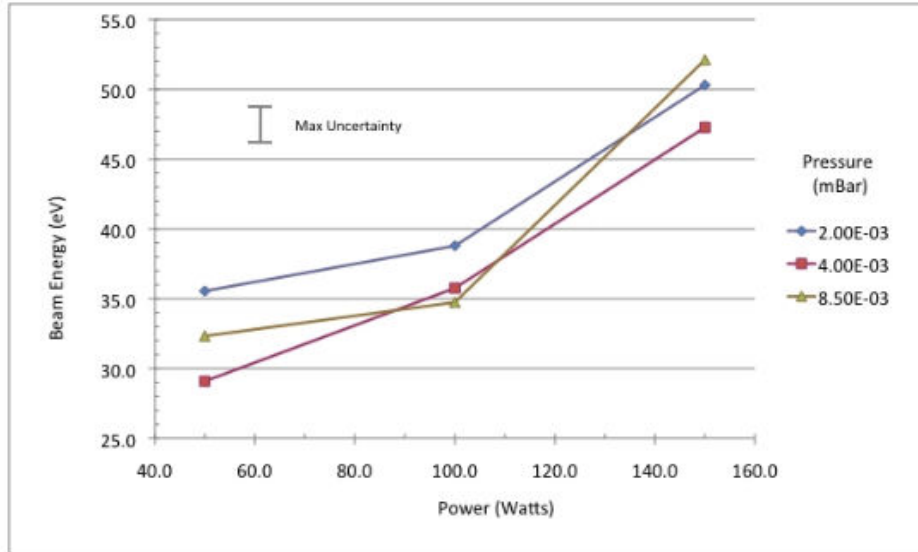


**Figure 5.5** Variation of Beam Energy with Input Power at 2e-3, 4e-3 and 8.5e-3mbar

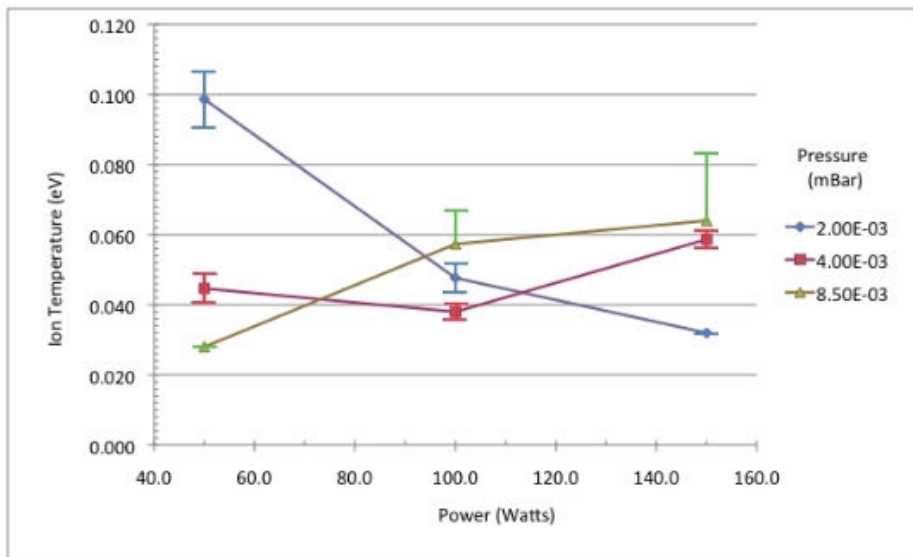


**Figure 5.6** Variation of Ion Temperature with Power at 2e-3, 4e-3 and 8.5e-3mbar

This trend can be seen clearly in Figure (5.6) for the 8.5e-3 mbar pressure case. However, as the pressure decreases the trend levels out and then reverses entirely. Because the temperature is also a measure of the spread of velocities, one might also assume that at higher pressures the spread in ion velocities (i.e. temperature) would also increase as a result of a higher level of

collisionality. This is seen somewhat in Figure (5.7) where the ion temperature is plotted versus pressure at each power level. The trend of increasing ion temperature with pressure is strongly evident in the 150W case, less so in the 100W and then completely reverses trend in the 50W case.

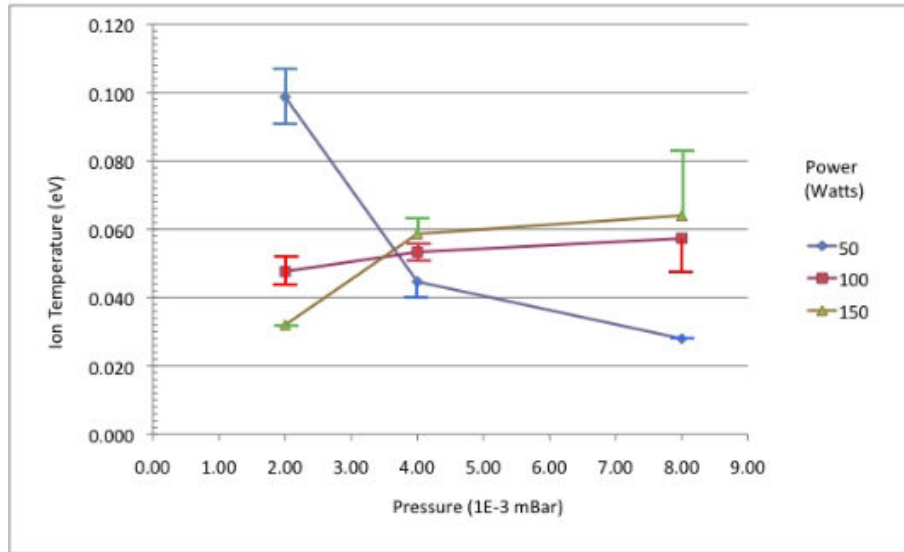


**Figure 5.7** Variation of Beam Energy with Pressure at 50, 100 and 150 Watts Power

At this time, no satisfactory theory of the reversed trends for the low pressure case in Figure (5.6) or the low power case in Figure (5.7) can be presented. It is not obvious that simply taking a more resolute data set would rectify the situation, but it may help to identify the functional dependence of ion temperature on pressure and power level. Resolving these trends is an element of future work.

## Chapter 6: Conclusions, Contributions and Future Work

### 6.1 Conclusions

The main objective of this thesis was to develop a helicon thruster test facility with preliminary diagnostics to provide for the evaluation of advanced thruster design concepts. This was accomplished through a combined program of analytical modeling, numerical simulation, and experimentation that focused on developing two standard diagnostic tools for studying plasmas and constructing a baseline thruster concept that uses permanent magnets instead of electromagnets.

#### 6.1.1 Analytical Modeling

The analytical model of the permanent magnet helicon thruster predicts that specific impulses of 1400 seconds and thrusts on the order of 10mN are achievable with efficiencies as high as 60%, although this does not include the efficiency of the power supply that drives the antenna. The primary losses are ionization and excitation, followed by wall losses.

While some ionization loss is unavoidable, it can be minimized by limiting the rate at which ions are lost to the walls. This is done by supplying a sufficiently high magnetic field and pinching it upstream to create a magnetic mirror. The magnetic confines the magnetized electrons, which in turn confines the ions through an ambipolar electric field. The ionization losses are estimated to be 40% of the beam power although this is actually conservative since it does not explicitly include this ambipolar diffusion effect.

The ambipolar diffusion was taken into account when evaluating the wall losses due to ion and electron energy deposition (heating). This loss rate was found to be proportional to the ratio  $n/T$  (density to electric field), which, from the helicon theory, is a function of the tube radius and ionization energy only. So, for a fixed thruster size and propellant, the heat loss to the wall should asymptotically reach some maximum value as the energy is increases, and then remain constant. This implies that the efficiency of the thruster should increase at higher power levels, but only a 10% gain might be possible.

The excitation (radiation) losses were estimated to be about 50% of the ionization losses for the baseline parameters that were assumed. Increasing the electron energy will tend to favor the ionization over the excitation based on the relative increase of cross-sectional area for each. However, the gains associated with the increase are nominal and must be traded against the overall power that is available to determine a desired operating point. The modeling shows that the permanent magnet helicon is indeed viable and offers performance benefits that are comparable or exceed existing electric propulsion systems.

### **6.1.2 Facility Development**

This research has successfully resulted in establishing a helicon thruster research facility, equipped with two standard plasma diagnostics. The first is a Langmuir probe that has been RF compensated to allow for measurement of the I-V characteristics of the plasma in the presence of an RF source. The lack of RF compensation is known to overpredict the electron temperature when measuring a characteristic, and indeed the results with and without the active compensation identify this trend. While the operation of the probe is straightforward, it would be beneficial to calibrate it against a known probe for future use.

The second instrument is a retarding potential analyzer. This instrument has been successfully used to measure the ion energy distribution function of the plasma downstream of the acceleration region. The data from the RPA is repeatable and is consistent with expected values. The main calibration issue with the RPA is the measurement of the total collected current, since it is difficult to know how much of the current that is intercepted by the probe makes it to the collector plate. Even without calibration, its ability to measure energy distribution is quite impressive, able to resolve the ion temperature to a high degree of precision.

### **6.1.3 Helicon Source Development and Testing**

The helicon thruster has been demonstrated to work using permanent magnets upstream of a single turn helical antenna. Direct measurements were made of the specific impulse, which was found to be near 1400 seconds using Argon. The extrapolated thrust based on the measurement of total current is much smaller than predicted, however because the RPA is uncalibrated there is a large degree of uncertainty here.

The ion beam energy was shown to increase with power, which would be expected. At higher pressures, there is a significant increase in beam energy from 100W to 150W as compared to from 50W to 100W. This is consistent with the assumption that from 50-100W the density of neutrals at high pressure is high enough that the ionization in the discharge tube is incomplete. An increase in power then results in an increase in ionization but not an increase in the electron temperature as a whole. Once complete ionization is achieved, additional energy input will result in an increase in electron temperature until wall losses, excitation and beam energy requirements provide the necessary power balance.

Ion energy distribution is not really an important parameter with regard to helicon engine operation, however because it is resolved by the RPA it is interesting to analyze its trends with changing input power and pressure. The expectation is that ion temperature should increase both with power input as well as with pressure, since the increased collisionality will tend to broaden the distribution function. Interestingly, there is a reversal in trends in the variation of ion temperature with both power and pressure. No satisfactory description of this phenomenon can be offered at this time, but it provides an interesting puzzle to be considered in future work.

## ***6.2 Contributions***

The contributions in this thesis are summarized below:

- 1) A 0-Dimensional analytical model of a helicon thruster was developed assuming the magnetic field strengths that would be available using permanent magnets. This model was used to predict the performance of such a thruster as it compared to other electric propulsion technologies. The model predicts specific impulse of 1400 seconds, thrust on the order of 10 mN and efficiency of 60%.
- 2) A helicon thruster research facility was designed and constructed, allowing for helicons of up to 1200W to be tested using an RF power supply with a matching network. To support testing, an RF compensated Langmuir probe and a retarding potential analyzer were constructed and interfaced with a desktop computer for data collection.
- 3) A prototype permanent magnet helicon thruster was constructed and tested using Argon as a propellant. Measurements with the RPA have produced some results that are

intuitive and consistent with expected operation of the thruster over a range of powers and pressures. For example, an increase in beam power with energy input that increases more rapidly once full ionization occurs. They have also produced some clear reverse trending in the ion temperatures that cannot be explained at this time. This presents an interesting area of research as a follow-on.

- 4) Preliminary operation was conducted using water vapor as a propellant; however additional diagnostics are required to assess its applicability.

### ***6.3 Future Work***

Future work on this project can be divided into three areas: Facility upgrades, Thruster upgrades and Experimental procedures.

#### **6.3.1 Facility Upgrades**

Continued experimentation with the existing diagnostics would benefit greatly from having them calibrated against other instruments or plasma sources, in particular with regard to the RF compensation of the Langmuir probe and the total current collected by the RPA. In addition, instrumentation that would allow for analyzing molecular gases as propellants would be useful. Examples include mass spectrometers, optical spectrometers or time of flight detectors. The failed attempt at directly measuring radiation could be re-attempted by modifying the copper sleeve with a transparent housing that would isolate it from plasma generated by the antenna outside of the discharge tube. The ability to place the Langmuir probe inside the discharge tube would also be very helpful in providing independent corroboration of the electron temperature and plasma density inside the source.

#### **6.3.2 Thruster Upgrades**

The thruster has already gone through a series of upgrades and redesigns over the course of its implementation. Future upgrades will focus on generating a more uniform and higher strength magnetic field with permanent magnets. Implementation of the magnetic bottle upstream of the plasma would also be of interest to reduce the plasma losses to the front wall. Placing baffles near the gas inlet can also increase the residence time of the neutrals in the discharge tube since their mean free path through the system is very long. The baffles can effectively make the

particles bounce back and forth on the walls as they diffuse through the length of the tube. Some consideration has been given to using very high permeability ( $\mu$ -metal) or very low permeability (superconducting) materials to better shape the magnetic fields. Ultimately, if the system is to be used as a space propulsion system, a suitably compact and efficient power supply must be developed. Initial efforts in this direction were attempted, but then the adoption of a commercially available supply was chosen in the interest of expediency.

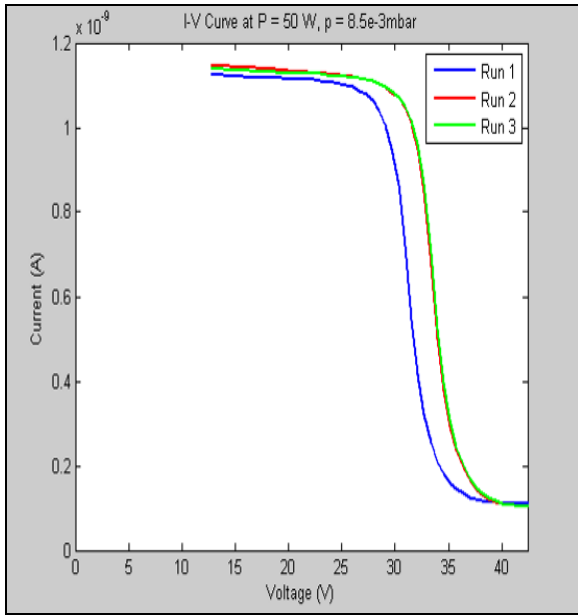
### **6.3.3 Experimental Procedures**

Even using only instrumentation and the thruster hardware that has been developed over the course of this research a number of additional experiments can be conducted.

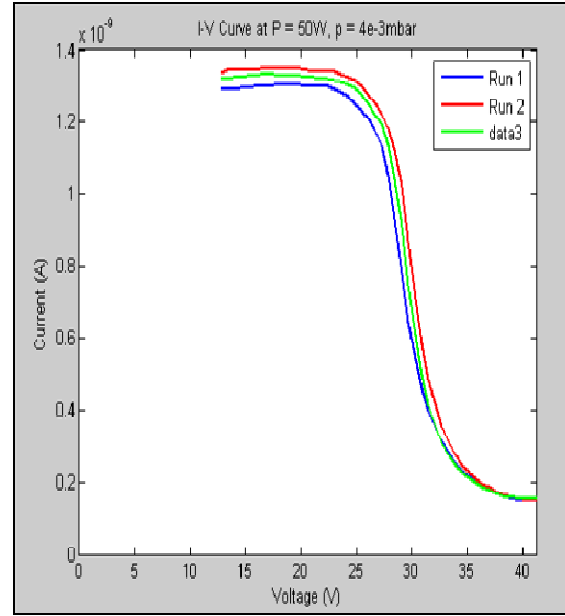
- 1) As mentioned above, the Langmuir probe can be moved inside of the discharge chamber to make direct measurements of the electron temperature and plasma density to compare against other measurements.
- 2) The RPA can be oriented at various angles off the centerline of the thruster to measure the beam divergence.
- 3) A higher density of data points can be taken over sweeps of energy and pressure to better resolve the trends discussed in Chapter 5 and hopefully lead to a theory as to why these trends are occurring.
- 4) The radiation diagnostic (copper sleeve) can be modified to see if direct measurements of the radiated power can be achieved.
- 5) The Langmuir probe can be moved off-axis to help determine whether the electron population is beamlike with a thermal spread or truly thermalized.

# Appendices

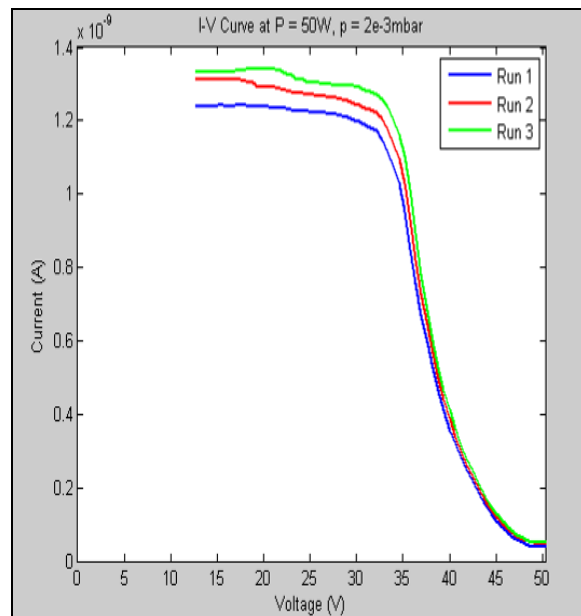
## APPENDIX A: RPA I-V Curves for Argon



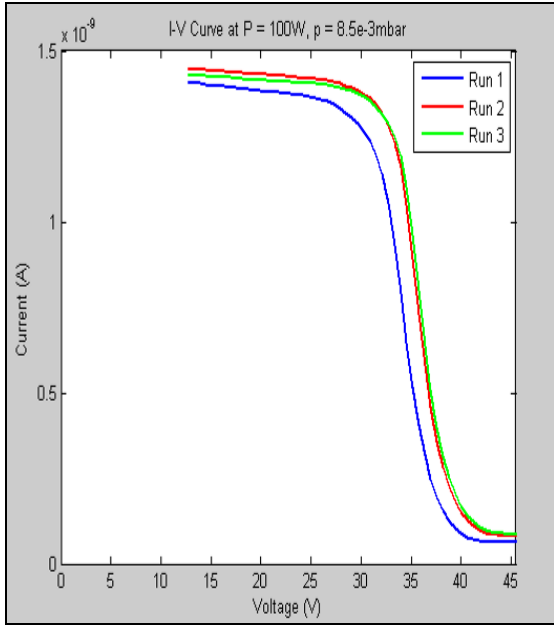
I-V Curve P = 50W, p = 8.5e-3mbar



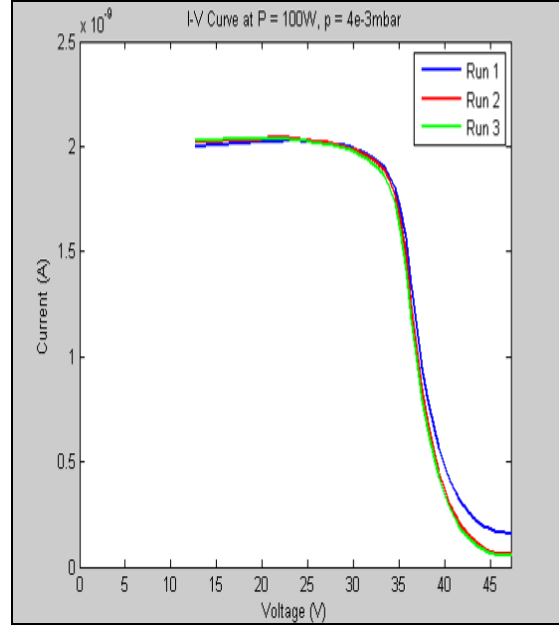
I-V Curve P = 50W, p = 4e-3mbar



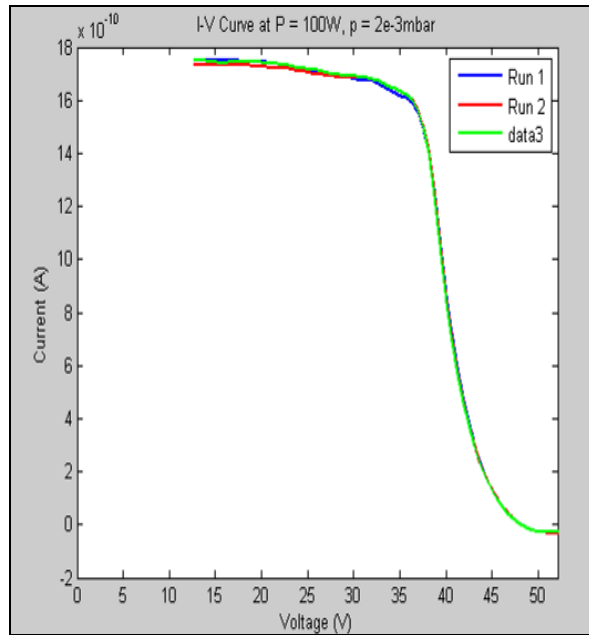
I-V Curve P = 50W, p = 2e-3mbar



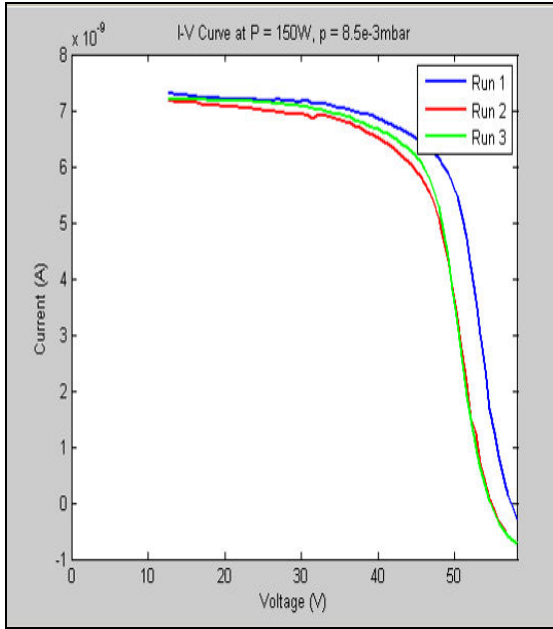
I-V Curve P = 100W, p = 8.5e-3mbar



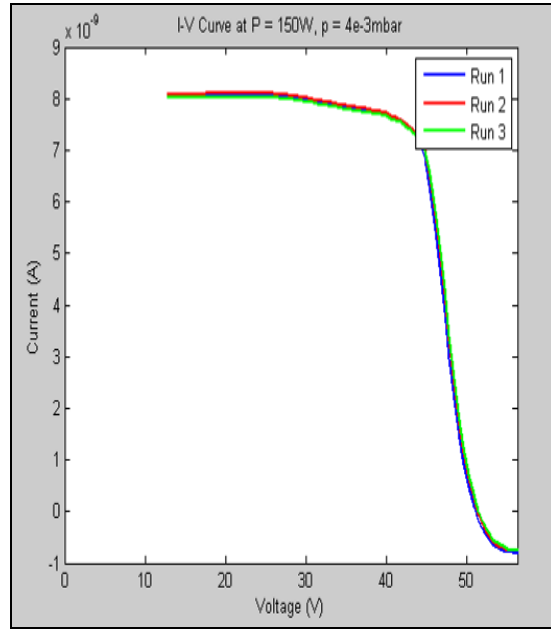
I-V Curve P = 100W, p = 4e-3mbar



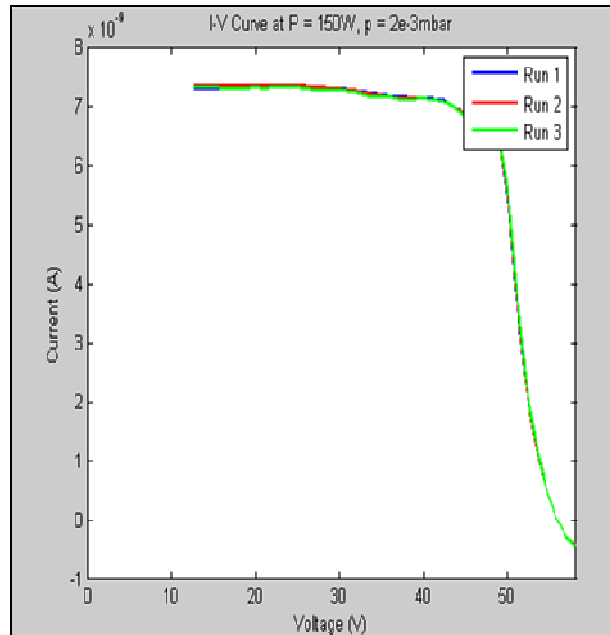
I-V Curve P = 100W, p = 2e-3mbar



I-V Curve P =150W, p =8.5e-3mbar

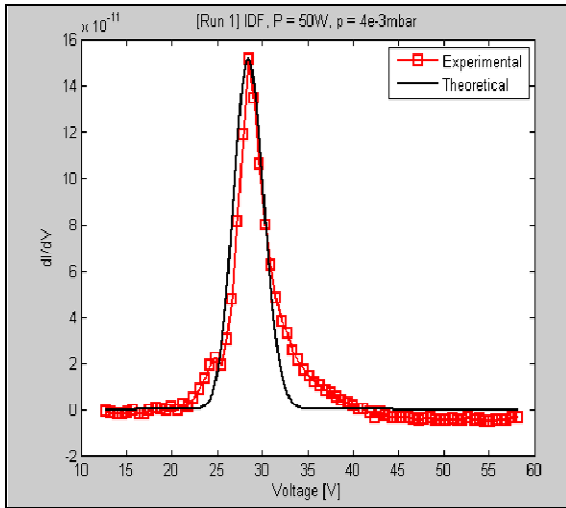


I-V Curve P =150W, p =4e-3mbar

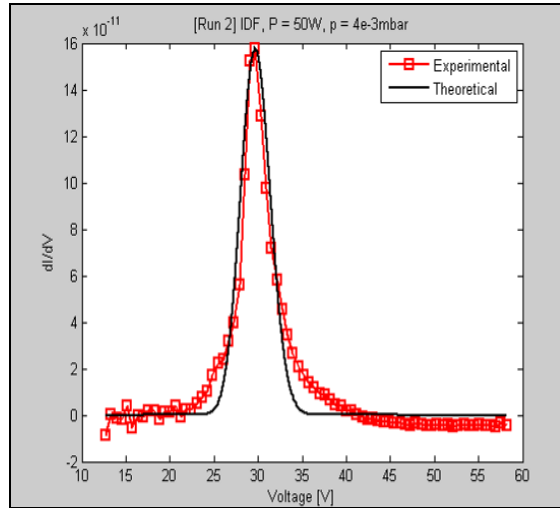


I-V Curve P =150W, p =2e-3mbar

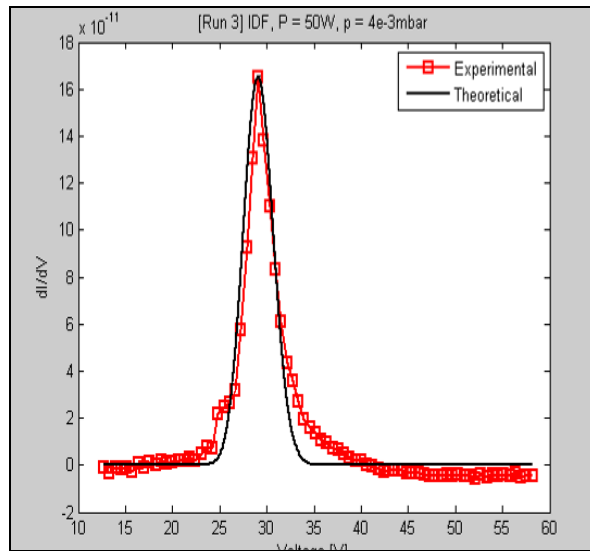
## APPENDIX B: RPA Ion Distribution Functions for Argon



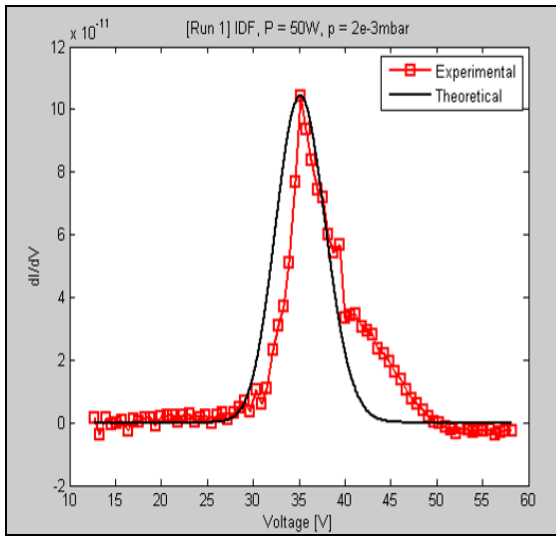
Ion Distribution Function—  
P = 50W, p = 4e-3mbar [Run 1]  
[Solid line] theoretical  
[Red squares] experimental



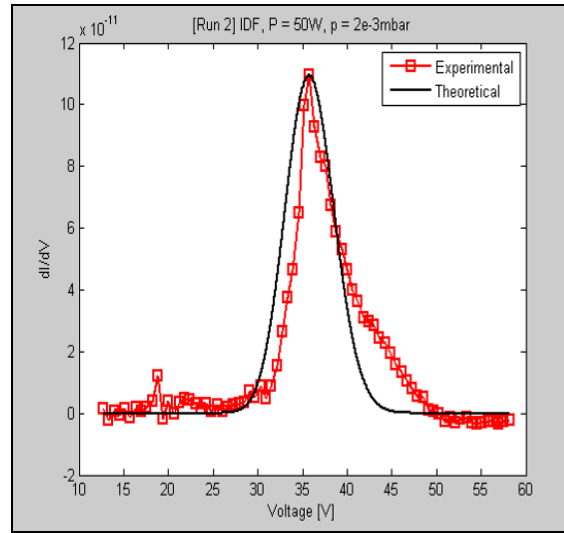
Ion Distribution Function—  
P = 50W, p = 4e-3mbar [Run 2]  
[Solid line] theoretical  
[Red squares] experimental



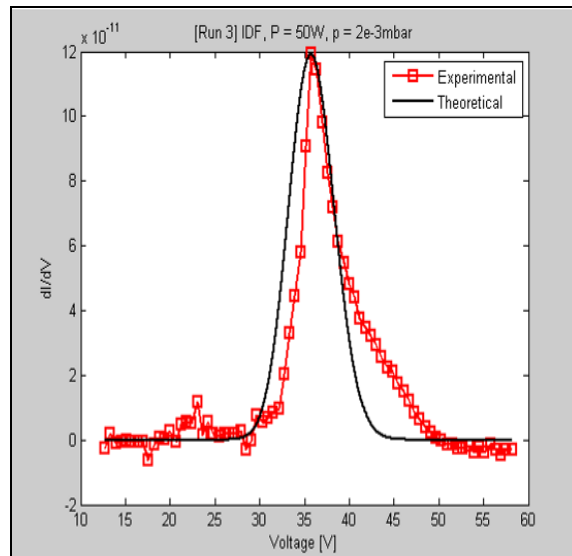
Ion Distribution Function—  
P = 50W, p = 4e-3mbar [Run 3]  
[Solid line] theoretical  
[Red squares] experimental



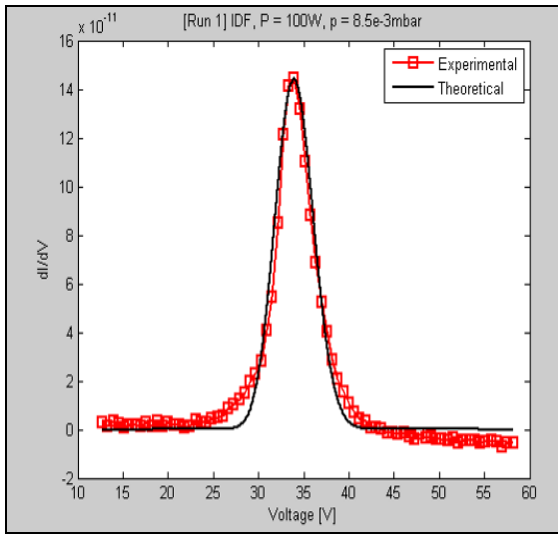
Ion Distribution Function—  
 $P = 50W$ ,  $p = 2e-3mbar$  [Run 1]  
 [Solid line] theoretical  
 [Red squares] experimental



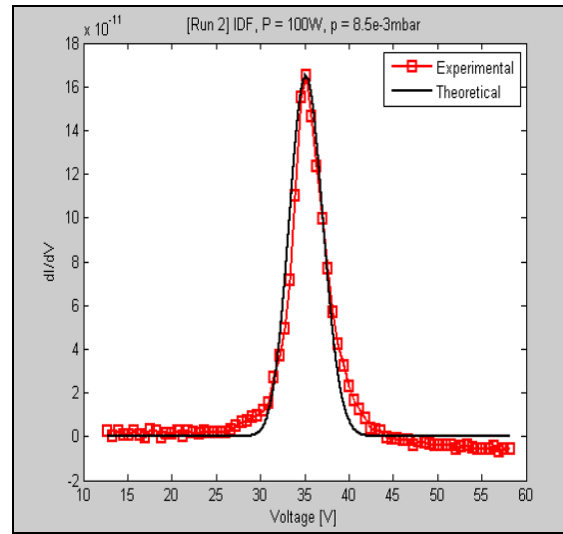
Ion Distribution Function—  
 $P = 50W$ ,  $p = 2e-3mbar$  [Run 2]  
 [Solid line] theoretical  
 [Red squares] experimental



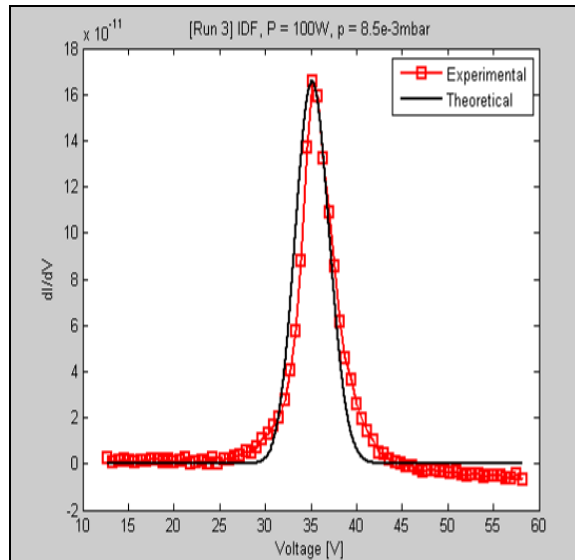
Ion Distribution Function—  
 $P = 50W$ ,  $p = 2e-3mbar$  [Run 3]  
 [Solid Line] theoretical  
 [Red squares] experimental



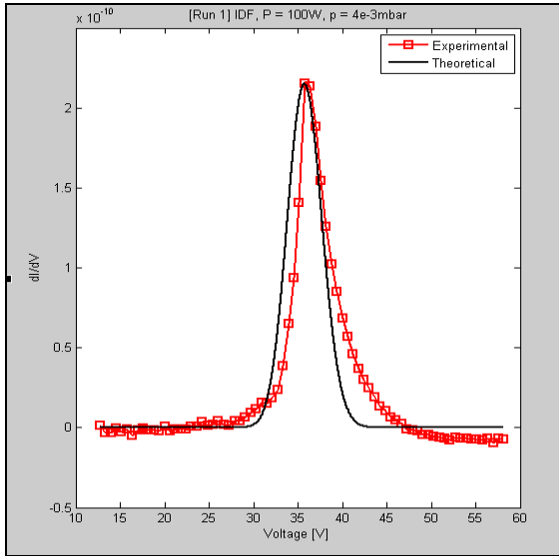
Ion Distribution Function—  
 $P = 100\text{W}$ ,  $p = 8.5\text{e-}3\text{mbar}$  [Run 1]  
 [Solid line] theoretical  
 [Red squares] experimental



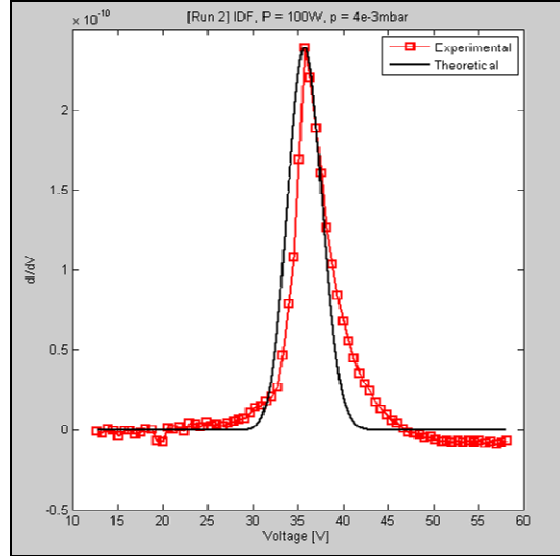
Ion Distribution Function—  
 $P = 100\text{W}$ ,  $p = 8.5\text{e-}3\text{mbar}$  [Run 2]  
 [Solid line] theoretical  
 [Red squares] experimental



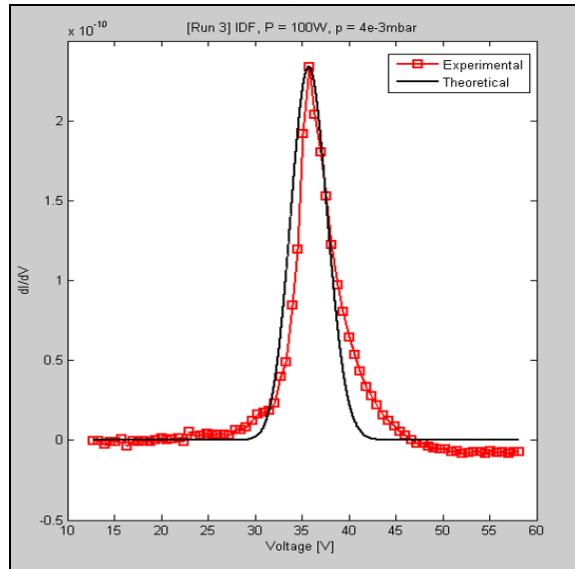
Ion Distribution Function—  
 $P = 100\text{W}$ ,  $p = 8.5\text{e-}3\text{mbar}$  [Run 3]  
 [Solid line] theoretical  
 [Red squares] experimental



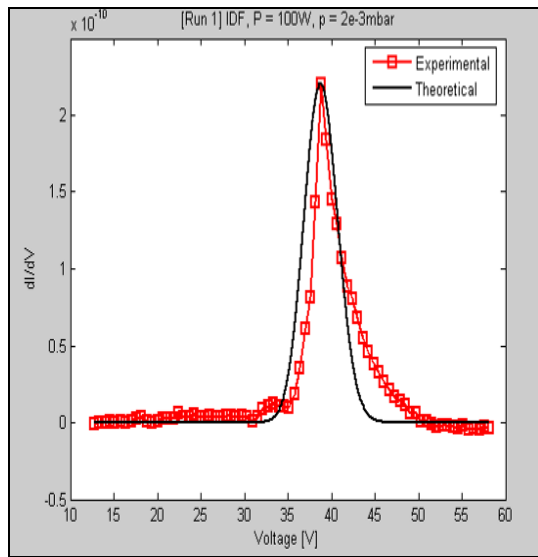
Ion Distribution Function—  
 P = 100W, p = 4e-3mbar [Run 1]  
 [Solid line] theoretical  
 [Red squares] experimental



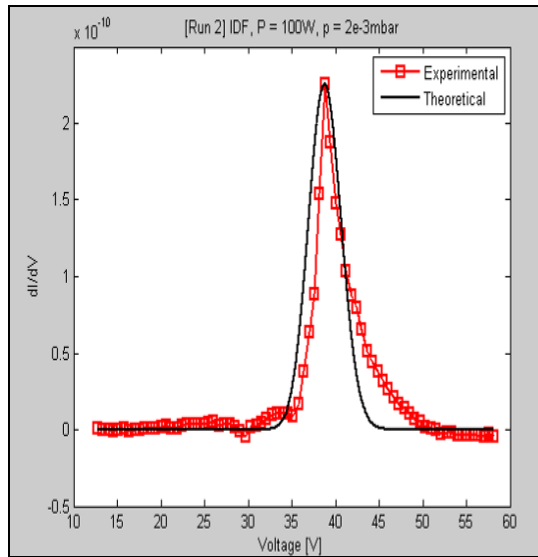
Ion Distribution Function—  
 P = 100W, p = 4e-3mbar [Run 2]  
 [Solid line] theoretical  
 [Red squares] experimental



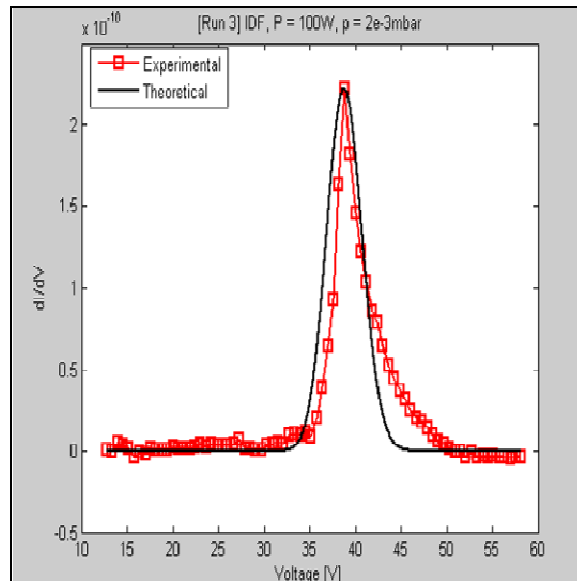
Ion Distribution Function—  
 P = 100W, p = 4e-3mbar [Run 3]  
 [Solid line] theoretical  
 [Red squares] experimental



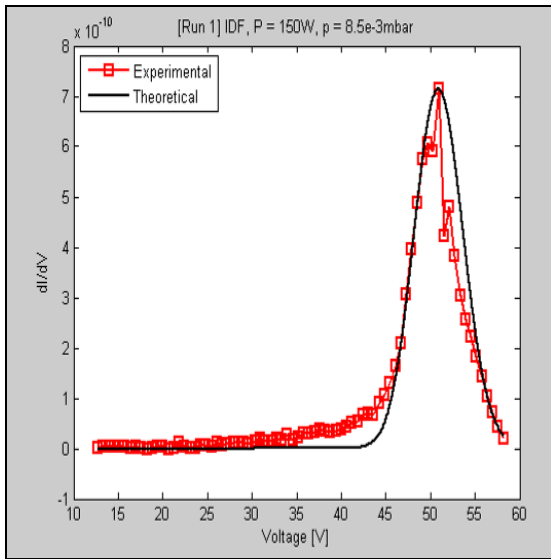
Ion Distribution Function—  
 $P = 100\text{W}$ ,  $p = 2\text{e-}3\text{mbar}$  [Run 1]  
 [Solid line] theoretical  
 [Red squares] experimental



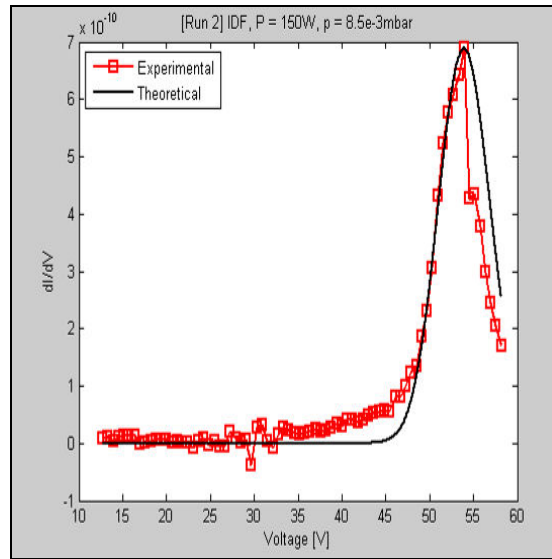
Ion Distribution Function—  
 $P = 100\text{W}$ ,  $p = 2\text{e-}3\text{mbar}$  [Run 2]  
 Solid line [theoretical]  
 [Red squares] experimental



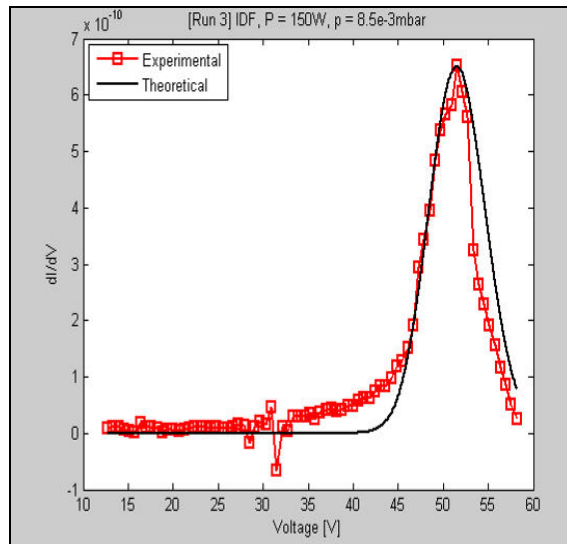
Ion Distribution Function—  
 $P = 100\text{W}$ ,  $p = 2\text{e-}3\text{mbar}$  [Run 3]  
 [Solid line] theoretical  
 [Red squares] experimental



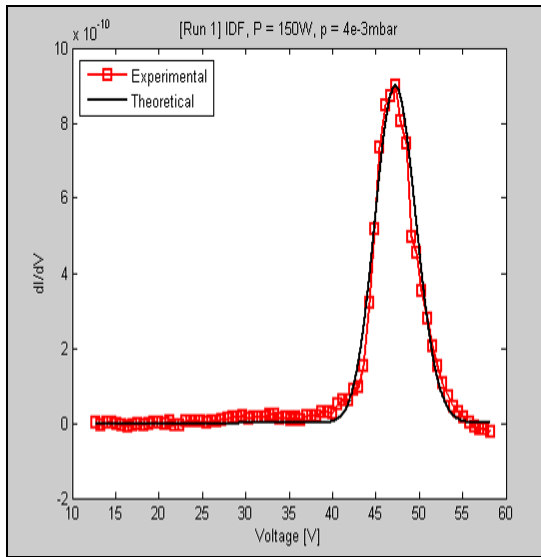
Ion Distribution Function—  
 P = 150W, p = 8.5e-3mbar [Run 1]  
 [Solid line] theoretical  
 [Red squares] experimental



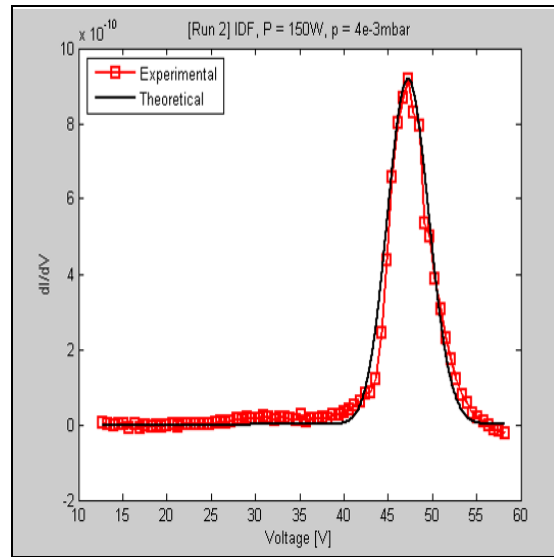
Ion Distribution Function—  
 P = 150W, p = 8.5e-3mbar [Run 2]  
 [Solid line] theoretical  
 [Red squares] experimental



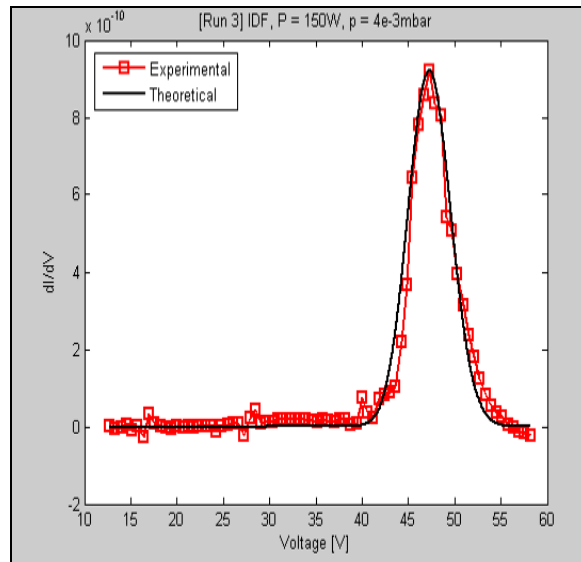
Ion Distribution Function—  
 P = 150W, p = 8.5e-3mbar [Run 3]  
 [Solid line] theoretical  
 [Red squares] experimental



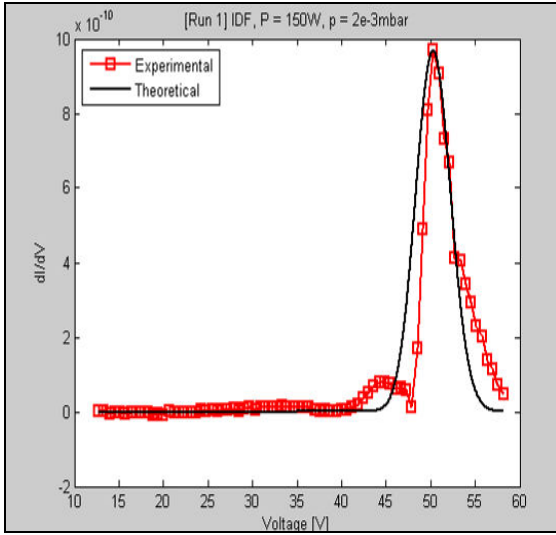
Ion Distribution Function—  
 $P = 150\text{W}$ ,  $p = 4\text{e-}3\text{mbar}$  [Run 1]  
 [Solid line] theoretical  
 [Red squares] experimental



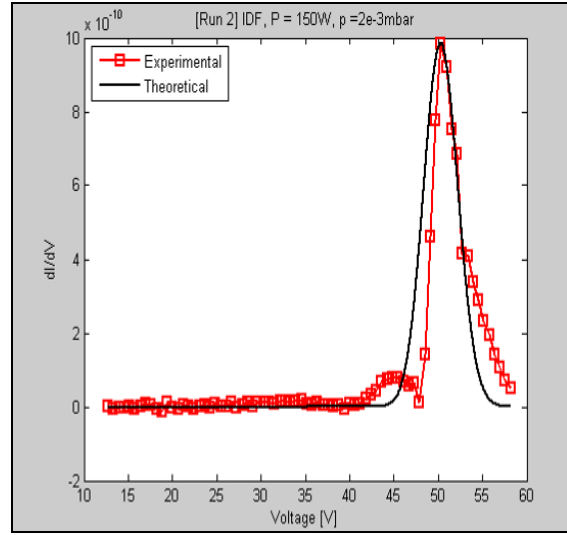
Ion Distribution Function—  
 $P = 150\text{W}$ ,  $p = 4\text{e-}3\text{mbar}$  [Run 2]  
 [Solid line] theoretical  
 [Red squares] experimental



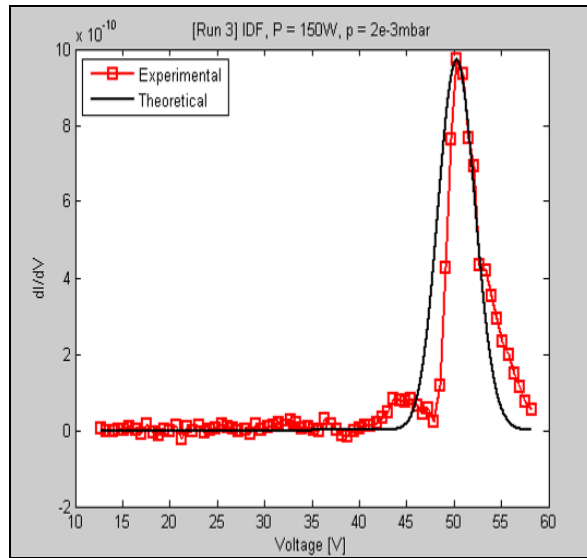
Ion Distribution Function—  
 $P = 150\text{W}$ ,  $p = 4\text{e-}3\text{mbar}$  [Run 3]  
 [Solid line] theoretical  
 [Red squares] experimental



Ion Distribution Function—  
 P =150W, p = 2e-3mbar [Run 1]  
 [Solid line] theoretical  
 [Red squares] experimental



Ion Distribution Function—  
 P =150W, p = 2e-3mbar [Run 2]  
 [Solid line] theoretical  
 [Red squares] experimental



Ion Distribution Function—  
 P =150W, p = 2e-3mbar [Run 3]  
 [Solid line] theoretical  
 [Red squares] experimental

## APPENDIX C: Error Analyses

### C.1 Langmuir Probe and RPA Error Analysis: Area under a Shifted Maxwellian

In the modified Langmuir probe analysis, the plasma parameters were found by matching the peak location of the  $dI/dV$  (EEDF) curve equal to that of a shifted Maxwellian and adjusting the parameters until the areas under the curve matched to within 1%. A similar approach was taken with the RPA to match to the ion energy distribution function (IEDF). A second approach for the RPA, which matched the Full Width at Half Max of the distribution, is discussed in the next section. The analysis will be discussed in terms of the EEDF, but applies equally well to the IEDF, except where noted.

The area under the curve is just the total collected current, which is given as an integral over the EEDF as

$$I_{\max} = \int_{\phi_{\min}}^{\phi_{\max}} A e^{-\beta f(\phi)} d\phi \quad (\text{C.1})$$

Taking the differential of this with respect to independent quantities yields

$$\Delta I_{\max} = a_1 \Delta \phi_{\min} + a_2 \Delta \phi_{\max} + a_3 \Delta \phi + a_4 \Delta A + a_5 \Delta \beta \quad (\text{C.2})$$

where  $a_1 = (A e^{-\beta f(\phi_{\max})})$ ,  $a_2 = (-A e^{-\beta f(\phi_{\min})})$ ,  $a_3 = \left( \int_{\phi_{\min}}^{\phi_{\max}} e^{-\beta f(\phi)} d\phi \right)$ ,  $a_4 = \left( \int_{\phi_{\min}}^{\phi_{\max}} A e^{-\beta f(\phi)} d\phi \right)$  and

$a_5 = \left( \int_{\phi_{\min}}^{\phi_{\max}} A f(\phi) e^{-\beta f(\phi)} d\phi \right)$ , with  $f(\phi) = (\sqrt{\phi} - \sqrt{\phi_b})^2$ . Because the derivative of the data set is

found using a finite difference, the uncertainty in a given value of the  $dI/dV$  curve is proportional to the second derivative, as shown in equation (C.3).

$$\frac{f(\phi_0 + \Delta\phi) - f(\phi_0)}{\Delta\phi} = f'(\phi_0) + \frac{f''(\phi_0)}{2!} \Delta\phi \quad (\text{C.3})$$

Linearizing the second derivative from the analytical form of  $dI/dV$ , the uncertainty in the peak amplitude is found to be

$$\frac{\Delta A_{amp}}{A_{amp}} = \frac{1}{v_b^2 4\phi_b} \Delta\phi^2 \quad (A \rightarrow A_{amp}) \quad (C.4)$$

where a notational change has been made to avoid confusion with the probe tip area. The uncertainty of the area under the curve is just  $\Delta I_{max}$ , which is a function of the resolution of the PicoAmmeter. This is given as  $0.4\% \pm 400$  fA. Alternatively, the uncertainty in the potential is actually given by the step size that was used to collect the data during the voltage sweep. For the Langmuir probe it was a step size of  $\Delta\phi = 2V$ .

Solving for  $\Delta\beta$  yields

$$\Delta\beta = \frac{1}{|a_5|} \left[ (a_1^2 + a_2^2 + a_3^2) (\Delta\phi)^2 + a_4^2 \Delta A^2 + \Delta I_{max}^2 \right]^{1/2} \quad (C.5)$$

And since  $\beta = \frac{1}{T}$ , the uncertainty in the temperature is just  $\frac{\Delta T}{T} = \frac{\Delta\beta}{\beta}$ . The peak of the EEDF is also related to the probe area, the electron temperature and the plasma density. Specifically for the case of the Langmuir probe, solving for the uncertainty in the plasma density results in

$$\frac{\Delta n}{n} = \left[ \left( \frac{\Delta A_{area}}{A} \right)^2 + \left( \frac{\Delta T}{T} \right)^2 + \left( \frac{\Delta A_{amp}}{A_{amp}} \right)^2 \right]^{1/2} \quad (C.6)$$

where the probe area uncertainty is related to the height and radius of the probe tip (which is

cylindrical) by  $\left( \frac{\Delta A_{area}}{A} \right)^2 = \left( \frac{\Delta h}{h} \right)^2 + \left( \frac{\Delta r}{r} \right)^2$ .

## C.2 RPA Error Analysis for Ion Temperature: Matching FWHM of IEDF curve

In the Full Width at Half Max (FWHM) method of determining the ion temperature, the points at which the distribution is matched are the peak and the half-max points. The half max points are found by setting the Maxwellian that is approximating the distribution equal to half the peak value as seen in equation (C.7)

$$\frac{-\partial I}{\partial \phi} = A \exp[-\beta f(\phi)] = \frac{A}{2} \quad (\text{C.7})$$

As in the analysis for the Langmuir probe, the function  $f(\phi) = \sqrt{\phi} - \sqrt{\phi_b}$  can be solved explicitly from equation (C.7). Applying this function at each half-max location results in two solutions for the potential

$$\phi = \left[ \left( \frac{\ln(2)}{\beta} \right)^{1/2} \pm \sqrt{\phi_b} \right]^2 \quad (\text{C.8})$$

So the full width is just found by subtracting these two values, and results in  $\phi_2 - \phi_1 = 4\sqrt{\phi_b} \sqrt{\alpha}$

where,  $\alpha = \sqrt{\frac{\ln(2)}{\beta}}$ . Solving for  $\beta$  and taking the natural log yields

$$\ln \beta = \ln(16 \ln(2)) + \ln(\phi_b) - 2 \ln(\phi_2 - \phi_1) \quad (\text{C.9})$$

and taking the differential

$$\frac{\Delta \beta}{\beta} = \frac{\Delta \phi_b}{\phi_b} + \frac{2\Delta(\phi_2 - \phi_1)}{\phi_2 - \phi_1} \quad \Rightarrow \quad \frac{\Delta T}{T} = \left( \left| \frac{\Delta \phi_b}{\phi_b} \right|^2 + 2 \left| \frac{(2\Delta\phi)}{\phi_2 - \phi_1} \right|^2 \right)^{1/2} \quad (\text{C.10})$$

where  $\frac{\Delta \phi}{\phi_2 - \phi_1} = \frac{\Delta \phi}{4(\phi_b \ln(2) T_{ev})^{1/2}}$ .

## ***APPENDIX D: MATLAB Code for Retarding Potential Analyzer Analysis***

### **Master Run Script**

```
color = ['b-'; 'r-'; 'g-'];
cidx = 1;
for file = 1:27,
    disp(['Now running file number ', num2str(file), ' ...']);
    [Tev_area(file), Tev_width(file), max_voltage(file)] =
OptimizeTev(file, color(cidx, :));
    if mod(file,3) == 0
        figure(2)
        saveas(gcf, ['Figures/Current_Voltage_', num2str(file), '.fig'], 'fig');
        hold off
        cidx = 0;
    end
    cidx = cidx + 1;
end

function [Tev_area, Tev_width, max_voltage] = OptimizeTev(filename, color)
```

The master run script calls assigned file numbers from excel in the c: / drive, and iteratively calculates the Area and Width of the function relative to the experimental distribution function provided by the Retarding Potential Analyzer. The maximum voltage [constraint] is determined by the shifted Maxwellian Distribution. The information is then output and plotted accordingly.

---

### **Optimize $T_{ev}$ [electron temperature]**

```
% function width = fwhm(x,y)

clear all
close all
format short g
voltage=xlsread(['Run',num2str(filenum)],'A20:A95');
current=xlsread(['Run',num2str(filenum)],'B20:B95');
dIdV= xlsread(['Run',num2str(filenum)],'C20:C95');
% voltage1=voltage;
%x=x1;
%

v_theory=voltage(1):0.01:voltage(end); % sweep theory voltage

startTev = 0.01;
error = 0.001;
start_error = 10;

[Tev_area,max_voltage] =
TevFromAreaRatio(voltage,v_theory,dIdV,startTev,error,start_error);
figure(1)
saveas(gcf,['Figures/dIdV_Voltage_',num2str(filenum),'.fig'],'fig');

[Tev_width] = TevFromWidth(voltage,v_theory,dIdV,startTev,error,start_error);

figure(2)
plot(voltage,current,color,'LineWidth',2);
hold on
xlabel('Voltage (V)');
ylabel('Current (A)');
[min_current,minidx] = min(current);
xlim([0 voltage(minidx)]);

Tev_area'
Tev_width'
max_voltage'
```

---

### **Calculate Width of Function**

```
function [Tev_width] =  
TevFromWidth(voltage, v_theory, dIdV, startTev, error, start_error)  
  
Tev = startTev;  
Tag = 1;  
e = start_error;  
while e>error && tag==1  
  
    % calculate width of the experimental curve  
    width_exp = CalculateWidth(voltage, dIdV);  
  
    % calculate the width of the theory curve  
    [max_dIdV, dIdV_idx]=max(dIdV); % determines the index of the maximum  
current  
    max_voltage = voltage(dIdV_idx); % finds the maximum voltage  
    f=-(sqrt(v_theory)-sqrt(max_voltage)).^2; % maxwellian distribution  
    g=exp(f/Tev).*max_dIdV;  
    width_theory = CalculateWidth(v_theory, g);  
  
    Tev=Tev+0.001;  
    e_new=abs((width_exp-width_theory)/width_theory);  
    if e_new>e  
        tag = 0;  
        Tev=Tev-0.001;  
    else  
        e=e_new;  
    end  
end  
  
Tev_width = Tev;
```

---

### **$T_{ev}$ from Area Ratio**

```
function [Tev_area,max_voltage] =
TevFromAreaRatio(voltage,v_theory,dIdV,startTev,error,start_error)
[max_dIdV,dIdV_idx]=max(dIdV); % determines the index of the maximum current
max_voltage = voltage(dIdV_idx); % finds the maximum voltage
ddIdV=diff(dIdV);
dtt=diff(v_theory); %takes the difference of the voltage
Tev=startTev; % assumed ion temperature
tag=1;
e=start_error;
while e>error && tag==1
    f=-(sqrt(v_theory)-sqrt(max_voltage)).^2; % maxwellian distribution
    g=exp(f/Tev).*max_dIdV;
    dg=diff(g); %takes difference between each point of the Maxwellian
    Area_theory = sum((g(1:end-1)+(dg/2)).*dtt);
    Area_exp = sum((dIdV(1:end-1)+(ddIdV/2)).*diff(voltage));
    Tev=Tev+0.001;
    e_new=abs((Area_exp-Area_theory)/Area_theory);
    if e_new>e
        tag = 0;
        Tev=Tev-0.001;
        g=exp(f/Tev).*max_dIdV;
    else
        e=e_new;
    end
end

end
Tev_area = Tev;

figure(1)
plot(voltage,dIdV,'-rs','LineWidth',2);
hold on
plot(v_theory,g,'-k','LineWidth',2);
%axis([20 40 0 18e-11]);
xlabel('Voltage [V]');
ylabel('dI/dV');
hold off
```

---

## **Full Width Half Maximum**<sup>58</sup>

```
function [width] = CalculateWidth(voltage,dIdV)

% calculate width of the experimental curve
dIdV = dIdV / max(dIdV);
N = length(dIdV);
lev50 = 0.5;
if dIdV(1) < lev50 % find index of center (max or min)
of pulse
    [garbage,centerindex]=max(dIdV);
    Pol = +1;
    disp('Pulse Polarity = Positive')
else
    [garbage,centerindex]=min(dIdV);
    Pol = -1;
    disp('Pulse Polarity = Negative')
end
i = 2;
while sign(dIdV(i)-lev50) == sign(dIdV(i-1)-lev50)
    i = i+1;
end %first crossing is between v(i-1) &
v(i)
interp = (lev50-dIdV(i-1)) / (dIdV(i)-dIdV(i-1));
tlead = voltage(i-1) + interp*(voltage(i)-voltage(i-1));
i = centerindex+1; %start search for next crossing at
center
while ((sign(dIdV(i)-lev50) == sign(dIdV(i-1)-lev50)) && (i <= N-1))
    i = i+1;
end
if i ~= N
    Ptype = 1;
    disp('Pulse is Impulse or Rectangular with 2 edges')
    interp = (lev50-dIdV(i-1)) / (dIdV(i)-dIdV(i-1));
    ttrail = voltage(i-1) + interp*(voltage(i)-voltage(i-1));
    width = ttrail - tlead;
else
    Ptype = 2;
    disp('Step-Like Pulse, no second edge')
    ttrail = NaN;
    width = NaN;
end
```

## ***APPENDIX E: MATLAB Code for Langmuir Probe Analysis***

---

### **Master Run Script—Langmuir**

```
% Master Run Langmuir Probe
voltage=xlsread('Lang.xls','A1:A40');
dIdV=xlsread('Lang.xls','B1:B40');
voltage_IV=xlsread('LangIV.xls','A1:A40');
current_IV=xlsread('LangIV.xls','B1:B40');
v_theory = (voltage(1):.01:voltage(end));
v_theory_IV=(voltage_IV(1):0.01:voltage_IV(end));
startTev = 22;
start_density = 1e15;
start_plpot = 220;
error = 0.01;
start_error = 100;
start_err=100;
Area = 0.000008;

[Tev,density,plasma_potential] = LangmuirProbOpt(voltage,v_theory,dIdV,...

startTev,start_density,start_plpot,error,start_error,Area,start_err,voltage_I
V,current_IV,v_theory_IV);
```

The program iteratively solves for the electron temperature, density and the plasma potential by matching the peak and width of the experimental electron distribution function. The program begins by solving for the electron temperature by looking at the area under the EEDF. Once the width is determined, the height of the curve is found by matching the density of the function. Lastly, the shift of the curve is determined by the plasma potential. The program runs until the error between curves are within 1%.

---

## **Langmuir Probe Optimization**

```
function [Tev,density,plasma_potential] =  
LangmuirProbOpt (voltage,v_theory,dIdV,startTev,start_density,start_plpot,erro  
r,start_error,Area,start_err,voltage_IV,current_IV,v_theory_IV)  
%[max_dIdV,dIdV_idx]=max(dIdV); % determines the index of the maximum current  
ddIdV=diff(dIdV); % takes the differetial of the experimental current  
dvt=diff(v_theory); %takes the difference of the voltage  
density = start_density; % assume a density  
Tev=startTev; % assumed ion temperature [eV]  
plasma_potential = start_plpot; % assume a potential
```

---

### ***Solve for the electron temperature***

```
tag=1;  
e=start_error;  
disp('Solving for Tev...');  
  
while e>error && tag==1  
    V = (((plasma_potential-v_theory)/Tev)-5.2);  
    if V<0  
        err = 1+erf(-V);  
    else  
        err = 1-erf(V);  
    end  
    current_theory = (exp(-(V.^2))+sqrt(pi)*5.2.*err).*sqrt((2*1.6E-  
19*Tev)/9.1E-31)*density*1.6E-19*Area;  
    dIdV_theory=diff(-current_theory);%takes difference between each point of  
the Maxwellian  
    ddIdV_theory=diff(-dIdV_theory);  
    Area_theory = sum((dIdV_theory(1:end-1)+(ddIdV_theory/2)).*dvt(1:end-1);  
    Area_exp = sum((dIdV(1:end-1)+(ddIdV/2)).*diff(voltage));  
  
    Tev=Tev+1;  
    e_new=abs((Area_exp-Area_theory)/Area_theory);  
    if e_new>e  
        tag = 0;  
        Tev=Tev-1;  
        V = (((plasma_potential-v_theory)/Tev)-5.2);  
        if V<0  
            err = 1+erf(-V);  
        else  
            err = 1-erf(V);  
        end  
        current_theory = exp(-(V.^2))+sqrt(pi)*5.2.*err).*sqrt((2*1.6E-  
19*Tev)/9.1E-31)*density*1.6E-19*Area;  
        dIdV_theory=diff(-current_theory); %takes difference between each  
point of the Maxwellian  
    else  
        e=e_new;  
    end  
end
```

```

end
figure(1)
plot(voltage,dIdV,'d','LineWidth',2);
hold on
plot(v_theory(1:end-1),dIdV_theory,'-k','LineWidth',2);
%axis([20 40 0 18e-11]);
xlabel('Voltage [V]');
ylabel('dI/dV');
hold off

```

---

***Solve for the density of the plasma***

```

tag=1;
e=start_error;
disp('Solving for density...');

while e>error && tag==1
    V = (((plasma_potential-v_theory)/TeV)-5.2);

    if V<0
        err = 1+erf(-V);
    else
        err = 1-erf(V);
    end
    current_theory = exp(-(V.^2))+sqrt(pi)*5.2.*err.*sqrt((2*1.6E-
19*TeV)/9.1E-31)*density*1.6E-19*Area;
    dIdV_theory=diff(-current_theory); %takes difference between each point
of the Maxwellian
    peak_theory = min(dIdV_theory);
    peak_exp = min(dIdV);
    density=density+1e13;
    e_new=abs((peak_exp-peak_theory)/peak_theory);
    if e_new>e
        tag = 0;
        density=density-1e13;
        V = (((plasma_potential-v_theory)/TeV)-5.2);
        if V<0
            err = 1+erf(-V);
        else
            err = 1-erf(V);
        end
        current_theory = exp(-(V.^2))+sqrt(pi)*5.2.*err.*sqrt((2*1.6E-
19*TeV)/9.1E-31)*density*1.6E-19*Area;
        dIdV_theory=diff(-current_theory); %takes difference between each
point of the Maxwellian
    else
        e=e_new;
    end

end

end
figure(2)
plot(voltage,dIdV,'d','LineWidth',2);
hold on
plot(v_theory(1:end-1),dIdV_theory,'-k','LineWidth',2);
%axis([20 40 0 18e-11]);
xlabel('Voltage [V]');

```

```
ylabel('dI/dV');
hold off
```

---

### ***Solve for the plasma potential***

```
tag=1;
e=start_error;
p=start_err;
disp('Solving for plasma potential...');

while e>error && tag==1
    V = ((plasma_potential-v_theory)/Tev)-5.2);
    if V<0
        err = 1+erf(-V);
    else
        err = 1-erf(V);
    end
    current_theory = exp(-(V.^2))+sqrt(pi)*5.2.*err.*sqrt((2*1.6E-
19*Tev)/9.1E-31)*density*1.6E-19*Area;
    dIdV_theory=diff(-current_theory); %takes difference between each point
of the Maxwellian
    ddIdV_theory=diff(-dIdV_theory);
    [peak_theory,peakthidx] = min(dIdV_theory);
    [peak_exp,peakexpidx] = min(dIdV);
    plasma_potential=plasma_potential+2;
    e_new=abs((voltage(peakexpidx)-v_theory(peakthidx))/v_theory(peakthidx));
    Area_theory = sum((dIdV_theory(1:end-1)+(ddIdV_theory/2)).*dvt(1:end-1));
    Area_exp = sum((dIdV(1:end-1)+(ddIdV/2)).*diff(voltage));
    e_new_area=abs((Area_exp-Area_theory)/Area_theory);
    if e_new>e
        if e_new_area>p
            tag = 0;
            plasma_potential=plasma_potential-2;
            %Tev=Tev-1;
            V = ((plasma_potential-v_theory)/Tev)-5.2);
            if V<0
                err = 1+erf(-V);
            else
                err = 1-erf(V);
            end
            current_theory = exp(-(V.^2))+sqrt(pi)*5.2.*err.*sqrt((2*1.6E-
19*Tev)/9.1E-31)*density*1.6E-19*Area;
            dIdV_theory=diff(-current_theory); %takes difference between each
point of the Maxwellian
        else
            p=e_new_area;
        end
    else
        e=e_new;
    end
end
end
% current_theory
figure(3)
plot(voltage,dIdV,'d','LineWidth',2);
hold on
```

```

plot(v_theory(1:end-1),dIdV_theory,'-k','LineWidth',2);
axis([30 110 -6e-4 0]);
xlabel('Voltage [V]');
ylabel('dI/dV');
h = title('Electron Distribution Function');
set(h,'FontName','Times','FontSize',10,...
    'FontWeight','bold');

legend('Experimental','Theoretical')
hold off

% figure(4)
% plot(voltage_IV,current_IV,'d')
% xlabel('Voltage (V)')
% ylabel('Current (A)')
% axis([30 110 0 0.1]);
% hold on
%
% plot(v_theory_IV,current_theory)%*(abs((start_density-
density)/density)), 'k')
% %axis([30 110 0 0.01]);
% xlabel('Voltage (V)')
% ylabel('Current (A)')
% %
% %
% T=(plasma_potential-99.5-5.5)/30

```

# Bibliography

- 
- <sup>1</sup> W.E. Morren, M.V. Whalen and J.S. Sovey, “Performance and Endurance Tests of a Laboratory Model Multipropellant Resistojet”, *AIAA J. of propulsion and Power*, Vol. 6, No. 1, pgs. 18-27, 1990.
  - <sup>2</sup> G. Soulas, H. Kamhawi, M. Patterson, M. Britton, M. Frandina, “NEXT Ion Engine 2000 Hour Wear Test Results”, AIAA-2004-3791, 40th AIAA/ASME/SAE/ASEE Joint Propulsion Conference and Exhibit, Fort Lauderdale, Florida, July 11-14, 2004.
  - <sup>3</sup> D. Jacobson, D. Manzella, R. Hofer, P. Peterson, “NASA's 2004 Hall Thruster Program”, AIAA-2004-3600, 40th AIAA/ASME/SAE/ASEE Joint Propulsion Conference and Exhibit, Fort Lauderdale, Florida, July 11-14, 2004.
  - <sup>4</sup> J.S. Sovey and M.A. Manteniaks, “Performance and lifetime assessment of magnetoplasma-dynamic arc thruster technology”, *AIAA J. of Propulsion and Power*, Vol.7, No.1, 1991.
  - <sup>5</sup> E. Bering, et al., “VASIMR VX-200: High Power Electric Propulsion for Space Transportation Beyond LEO”, AIAA-2009-6481, *AIAA SPACE 2009 Conference and Exposition*, Pasadena, California, Sep. 14-17, 2009.
  - <sup>6</sup> R.W. Boswell and Francis F. Chen, “Helicons—The Early Years”, *IEEE Trans. On Plasma Science*, Vol. 25, No. 6, December 1997.
  - <sup>7</sup> H. Barkhausen, “Whistling tones from the earth,” *Proc. I.R.E.*, Vol. 18, pg. 143, 1930.
  - <sup>8</sup> D.R. Hartree, “The propagation of electromagnetic waves in a refracting medium in a magnetic field”, *Proc. Cambridge Phil. Soc.*, Vol. 27, pg. 143, 1931.
  - <sup>9</sup> E.V. Appleton, “Wireless studies of the ionosphere”, *J. Inst. Elec. Engrs.*, Vol. 71, pg. 624, 1932.
  - <sup>10</sup> L.R.O. Storey. “An investigation of whistling atmospherics”, *Phil. Trans. Roy. Soc. London*, 246:113, 1953.
  - <sup>11</sup> P. Aigrain, “Les ‘helicons’ dans les semiconductors”, in *Proc. Int. Conf. Semiconductor Physics*, Prague, Czechoslovakia, 1960, pg. 224.
  - <sup>12</sup> R.M. Gallet, J.M. Richardson, B. Weider, and G.D. Ward, “Microwave whistler mode propagation in a dense laboratory plasma”, *Phys. Rev. Lett.*, Vol. 4, pg. 347, 1960.
  - <sup>13</sup> H.A. Belvin and P.C. Thonemann, Culham Laboratory, Rep, CLM-R12, 1961.

- 
- <sup>14</sup> T.J.M. Boyd and J.J. Sanderson, The Physics of Plasmas. Cambridge, UK, 2003.
- <sup>15</sup> G. Sato et al, “Experimental characterization of a density peak at low magnetic fields in a helicon plasma source”, *Plasma Sources Sci. Technol.* **16**, pgs. 734-741, 2007.
- <sup>16</sup> A.W. Degeling, C.O. Jung, R.W. Boswell and A.R. Ellingboe *Physics Plasmas*, **3** 2788, 1996.
- <sup>17</sup> C. Charles and R.W. Boswell, “Laboratory evidence of a supersonic ion beam generated by a current-free “helicon” double layer”, *Physics of Plasmas*, Vol. 11, No. 4, April, 2004.
- <sup>18</sup> C. Charles, “Spatially Resolved Energy Analyzer Measurements of an Ion Beam on the Low Potential Side of a Current-Free Double Layer”, *IEEE Transactions on Plasma Science*, Vol. 33, No. 2, Apr. 2005, pp. 336–337.
- <sup>19</sup> Fernando N. Gesto, B. D. Blackwell, Christine Charles, and R.W. Boswell, “Ion detachment in the helicon double layer thruster exhaust beam”, *Journal of Propulsion and Power*, Vol. 22, No. 1 January-February 2006.
- <sup>20</sup> N. Plihon, P. Chabert and C.S. Corr, “Experimental investigation of double layers in expanding plasmas”, *Physics of Plasmas*, **14**, 013506, 2007.
- <sup>21</sup> M. West, D. Michaels, C. Charles, and R.W. Boswell,” Testing a Helicon Double Layer Thruster Immersed in a Space-Simulation Chamber”, *Journal of Propulsion and Power*, Vol. 24, No. 1, January 2008.
- <sup>22</sup> F.F. Chen, “Permanent Magnet Helicon Source for Ion Propulsion”, *IEEE Transactions on plasma science*, Vol. 36, No. 5, 2008.
- <sup>23</sup> F.F. Chen, “Plasma ionization by helicon waves”, *Plasma Phy. and Cont. Fusion*, Vol. 33, No. 4, pgs. 339-364, 1991.
- <sup>24</sup> R.A. Ellingboe and R.W. Boswell, *Phys. Plasmas* **3** 2797, 1996.
- <sup>25</sup> R.W. Boswell, “Plasma production using a standing helicon wave”, *Phys. Lett. A*, Vol. 33, pg. 457, 1907.
- <sup>26</sup> Kim et al, “M = +1 mode helicon wave excitation using solenoid antenna”, *Phys. Lett. A*. 1996, reprint.
- <sup>27</sup> J.H. Kim, S. M. Yun and H. Y. Chang, “ $m = \pm 1$  and  $m = \pm 2$  mode helicon wave excitation”, *IEEE Trans. Plasma. Sci.*, Vol. 24, pgs. 1364, 1996.
- <sup>28</sup> D.D. Blackwell and F.F. Chen, “2D imaging of a helicon discharge”, PPG-1571 revised. September, 1997.

- 
- <sup>29</sup> K. Suzuki, K. Nakamura and H. Sugai, *Japan J Appl. Phys.* **35** 4044 1996.
- <sup>30</sup> A.M. Lieberman and J. A. Lichtenberg, “Principles of Plasma Discharges and Materials Processing”, New York: Wiley, 1994.
- <sup>31</sup> R.L. Kinder et al, “H- to W- mode transitions and properties of a multimode helicon plasma reactor”, *Plasma Sources Sci. Technol.* **12**, 561-575, 2003.
- <sup>32</sup> R.W. Boswell, “Very efficient plasma generation by whistler waves near the lower hybrid frequency”, *Plasma Phys. Control Fusion*, Vol. 26, pgs. 1147, 1984.
- <sup>33</sup> S.M. Lea, “Vlasov theory of Landau damping”, January 2007.
- <sup>34</sup> F.F. Chen and D.D. Blackwell, “Upper limit to Landau Damping in Helicon Discharges”, *Phys. Rev. Letters*. Vol. 82, No. 13, March 29, 1999.
- <sup>35</sup> K. P. Shamrai and V. B. Taranov, *Plasma Sources Sci.Technol.* **5**, 474 (1996).
- <sup>36</sup> K.P Shamrai and VB Taranov, 1994 *Plasma Phys. Control. Fusion* **36** 1719.
- <sup>37</sup> C. Charles, et al., “Xenon ion beam characterization in a helicon double layer thruster”, *Applied Physics Letters* 89, 261503 (2006)
- <sup>38</sup> Lieberman, M. A., Charles, C., and Boswell, R. W., “A Theory for Formation of a Low Pressure, Current-Free Double Layer”, *Journal of Physics D: Applied Physics*, Vol. **39**, No. 15, 2006, pp. 3294–3304.
- <sup>39</sup> F.F. Chen, “Physical mechanism of current-free double layers”, *Physics of Plasmas* **13**, 034502, February 2006.
- <sup>40</sup> F. F. Chen and D. Arnush, *Phys. Plasmas* **8**, 5051 (2001)
- <sup>41</sup> M.A Lennon et al., “Recommended Data on the Electron Impact Ionization of Atoms and Ions: fluorine to Nickel”, *J. Chem. Phys.*, Vol 73, pgs. 3763-3778, 1980
- <sup>42</sup> T.D. Märk and G.H. Dunn (eds): *Electron Impact Ionization*, Wien, New York: Springer, 1985
- <sup>43</sup> R.S. Brusa, G.P. Karwsz and A. Zecca, “Analytical Partitioning of Total Cross Sections for Electron Scattering on Noble Gases”, *Z. Phys. D*, Vol 38, pgs. 279-287, 1996.
- <sup>44</sup> Schneider, Darryn D., “Helicon Waves in High Density Plasmas”, Plasma Research Laboratory, Australian National University, Canberra, Australia, November, 1998.

- 
- <sup>45</sup> P. Horowitz and W. Hill, “The Art of Electronics”, Cambridge University Press. pgs. 32–33, 1989.
- <sup>46</sup> “Skin Depth”, *Wikipedia, The Free Encyclopedia*, 17 December 2008, 5:47 UTC. Wikimedia Foundation, Inc. 19 Jan. 2009 <[http://en.wikipedia.org/wiki/Skin\\_depth](http://en.wikipedia.org/wiki/Skin_depth)>
- <sup>47</sup> RF Safety Solutions, “IEEE Standards”  
[http://www.rfsafetysolutions.com/RF%20Radiation%20Pages/IEEE\\_Standards.html](http://www.rfsafetysolutions.com/RF%20Radiation%20Pages/IEEE_Standards.html)
- <sup>48</sup> COMSOL Multiphysics AC/DC Module, Software Package, Ver. 3.5, COMSOL Group, College Park, MD, 2009.
- <sup>49</sup> Y. Azziz and M. Martinez-Sanchez, “Experimental and Theoretical Characterization of a Hall Thruster Plume”, Cambridge, Massachusetts, PhD Thesis, June 2007.
- <sup>50</sup> R. Hofer, J. Haas, A. Gallimore, “Ion Voltage Diagnostics in the Far-Field Plume of a High-Specific Impulse Hall Thruster”, AIAA-2003-4556, 39th Joint Propulsion Conference, Huntsville, AL, July 20-23, 2003.
- <sup>51</sup> I.D. Sudit and F.F. Chen, “RF Compensated probes for high density discharges”, *Plasma Sources Sci. Technol.* **3** (1994) pp.162-168.
- <sup>52</sup> A. Boschi and F. Magistrelli, 1963 *Nuovo Cimrnto* **29** 487.
- <sup>53</sup> V.A. Godyak and R.B. Piejak, *Plasma Sources Sci. Technol.* **1** **36**, 1992.
- <sup>54</sup> C. Charles, “Hydrogen ion beam generated by a current-free double layer in a helicon plasma”, *Applied Physics Letters*, Vol 84, No. 3, November 2003.
- <sup>55</sup> O. Batishchev, “Experimental Study of the Mini-Helicon Thruster”, *Air Force Research Laboratory*, Edwards AFB, CA, February 2008.
- <sup>56</sup> J.M. Pucci, N. Sinenian, et al, “Preliminary Characterization of a Helicon Plasma Source for Space Propulsion”, 42<sup>nd</sup> AIAA/ASME/SAE/ASEE Joint Propulsion Conference and Exhibit, Sacramento, CA, July 2006.
- <sup>57</sup> F.F. Chen, “DC Probe Diagnostics of Phased EEDF’s in RF discharges”, *Plasma Phys. Control Fusion* **39** (1997) 1553-1550.
- <sup>58</sup> Egan, Patrick, “Full Width Half Maximum”, Matlab Central, March 2006.  
<<http://www.mathworks.com/matlabcentral>>